Use of spacecraft onboard sensors for autonomous collision avoidance

Politecnico di Bari

Department of Mechanics, Mathematics and Management
MECHANICAL AND MANAGEMENT ENGINEERING
Ph.D. Program
SSD: IIND-01/E – AEROSPACE EQUIPMENTS AND SYSTEMS
IINF-01/A – ELECTRONICS

Final Dissertation

Use of spacecraft onboard sensors for autonomous collision avoidance

---

by

GIULIO CAMPITI

Supervisors:

Prof. Caterina CIMINELLI

Prof. Eugenio DI SCIASCIO

Coordinator of Ph.D. Program:
Prof. Marco Donato DE TULLIO

Course n°37, 01/11/2021 – 31/10/2024

Politecnico di Bari

Department of Mechanics, Mathematics and Management
MECHANICAL AND MANAGEMENT ENGINEERING
Ph.D. Program
SSD: IIND-01/E – AEROSPACE EQUIPMENTS AND SYSTEMS
IINF-01/A – ELECTRONICS

Final Dissertation

Use of spacecraft onboard sensors for autonomous collision avoidance

by

GIULIO CAMPITI

Referees:

Prof. Dario MODENINI

Prof. Michele MAESTRINI

Supervisors:

Prof. Caterina CIMINELLI

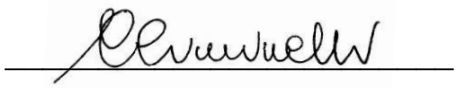

Prof. Eugenio DI SCIASCIO

Coordinator of Ph.D. Program:

Prof. Marco D. DE TULLIO

Course n°37, 01/11/2021 – 31/10/2024

Abstract

The space population is rapidly growing and so is the likelihood of in-orbit collisions, making space operations always more complicated and costly. The current process behind spacecraft collision avoidance mainly relies on surveillance data provided by ground-based sensors. These data contain uncertainties that largely affect collision avoidance decisions, leading to execute maneuvers in a conservative way, i.e., much more frequently than necessary. Whenever a maneuver is performed, some propellant is lost to move the satellite and on-board science instruments are typically switched off, causing a temporary interruption of the nominal operations. Therefore, especially in view of the future levels of space traffic, improving the quality of orbital information is essential to reduce the rate of unnecessary maneuvers and improve the cost-effectiveness of space operations.

To reduce positional uncertainties, this thesis investigates the use of onboard sensors to enable satellites, whenever at risk of collision, to autonomously observe the hazardous objects during the orbits before the Time of Closest Approach (TCA). The acquired data would be processed directly onboard to refine the positional knowledge of the secondary object, starting from initial orbital estimates uplinked from the ground, ultimately leading to an autonomous maneuver decision. Space-based observations can improve the positional accuracy for two main reasons: 1) they are not affected by atmospheric issues such as diffraction, aberration or turbulences, and 2) compared to ground-based observations, they can be made much closer to the TCA (e.g. 0.5-1.5 orbits before the event), which significantly improves the final prediction accuracy.

This thesis provides a feasibility study and performance assessment for the proposed avoidance system by addressing multiple technical aspects. Firstly, an in-depth study of the orbital dynamics of conjuncting objects in Low Earth Orbit (LEO) is performed to characterize potential observation windows arising during the time leading up to TCA. The analysis focuses on key features that will help determining the most suitable sensing technology, including the average number of observation opportunities, their duration, relative distances between objects, and others. This is done by reconstructing and analyzing the trajectory evolution for thousands of historical conjunction events, starting from Two-Line Element sets and using a Simplified General Perturbations 4 model for the propagation.

Following an initial investigation of potential onboard sensor technologies, the results of the previous study narrow the focus to the most feasible option, which turns out to be electro-optical sensors. A more detailed study is then conducted on

these sensors through a parametric analysis, mapping their in-orbit detection performance across a range of possible parameters. Particularly, the detection concept is simulated in a Matlab–System Tool Kit environment across hundreds of space-to-space observational scenarios, modeling various imaging systems of different quality. Unlike works from other authors based on analytic models of the apparent magnitude and Signal-to-Noise Ratio (SNR), realistic synthetic images of the simulated scenes are generated through commercial software, which are then post-processed to derive the SNR of the detected targets and to calculate the detection probability for each considered sensor.

Finally, for the limited set of feasible sensor options identified, astrometry and orbit determination analyses are conducted to assess whether and to what extent successful in-orbit observations can improve prediction accuracy, thereby reducing maneuver rates. A few conjunction case studies are first set up using the environment developed in the previous step. For each synthetic image, plate-solving tools are employed to map pixel coordinates to sky coordinates using mathematical transformations, enabling the extraction of orbital information for detected targets, including associated uncertainties. The resulting measurements are then used to simulate the process of updating the trajectory estimation for the secondary object in orbit. Orbit determination methods, specifically sequential filters, are applied due to their suitability for real-time updates.

Contents

List of figures

List of tables

Chapter 1

Introduction

1.1 Background

The ever-decreasing launch costs and the emergence of private actors in the space sector have led to a strong intensification of space activities during the last decade. The annual number of launched payloads has almost quintupled in the 2019-2022 period [1, 2], and with the various ongoing plans for mega-constellations, this trend is set to continue. Besides active payloads, space debris – encompassing defunct satellites, spent rocket stages, and fragments resulting from collisions or disintegration – is also proliferating, contributing to the increasing congestion of near-Earth space. Space agencies regularly monitor and report on space environment statistics, with publicly available resources such as ESA's "Annual Space Environment Report" and NASA's "Orbital Debris Quarterly News". According to the latest statistics, there are about 11,500 intact satellites in orbit, of which 9,000 are still functioning. As for space debris, it is estimated that there are approximately 36,500 pieces larger than 10 cm and 1 million sized in between 1-10 cm [3].

Given that orbital velocities are in the order of 8 km/s in Low-Earth Orbit (LEO) and 3 km/s in Geostationary Earth Orbit (GEO) – which are several times faster than a bullet – the energy released upon impact by such particles can be devastating, potentially terminating a mission. Even particles in the millimeter range are concerning, as they can penetrate satellite structures and cause significant damage or even destruction of internal components. An example of this can be seen in Fig. 1.1, showing the radiator section of the WFPC2 camera mounted onboard the Hubble Space Telescope. After over 15 years of exposure to space, this section was returned to Earth and revealed numerous holes caused by space debris. Remarkably, the largest holes measured about 30 mm in diameter, despite the debris particles themselves being less than a millimeter in size.

Each collision generates more debris, which in turn increases the likelihood of further collisions in a cascading effect, commonly referred to as the Kessler Syndrome [4]. Some major collision events in recent history, such as that between Iridium and Cosmos satellite in 2009, significantly contributed to debris creation, as highlighted in Fig. 1.2. These events include deliberate collisions due to Anti-Satellite Tests (ASAT), which are military tests involving missiles or

other weapons to target and destroy a satellite, conducted to demonstrate a nation's ability to disable or eliminate space infrastructures.

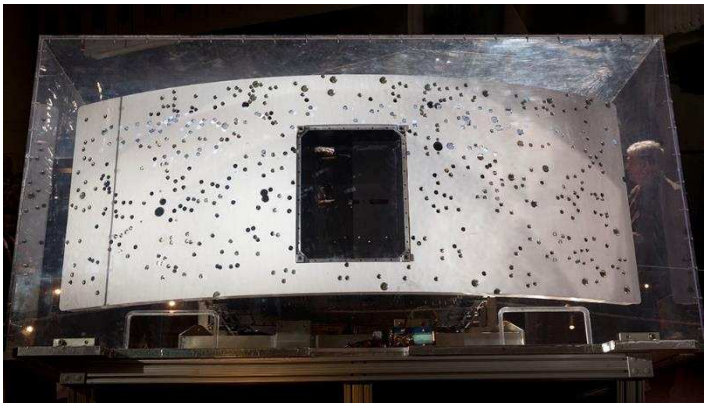

Fig. 1.1 Impact damage on the radiator section of the WFPC2 instrument. Image Credit: Eric Long, National Air and Space Museum, Smithsonian Institution [5]

As result of the increased orbital congestion, the impact on satellite operations is rapidly worsening, as underscored by recent highlights. ESA's satellites executed three to four collision avoidance maneuvers (CAMs) in 2023 [6], compared to an average of two in 2022. SpaceX's "Starlink" satellites maneuvered a total of nearly 50,000 times over the one-year period leading up to November 30, 2023 [7, 8], although using a maneuver threshold ten times more sensitive than the industry standard. The International Space Station had to alter its trajectory twice within a single week during August 2023 to avoid potential strikes, as reported in [9].

Whenever a maneuver is performed, some propellant is lost to move the satellite and the onboard science instruments are typically switched off, causing a temporary interruption of nominal operations [6]. On May 16, 2022, five scheduled data downlinks of ESA's Copernicus Sentinel 1–A satellite had to be canceled to avoid a potential collision [10].

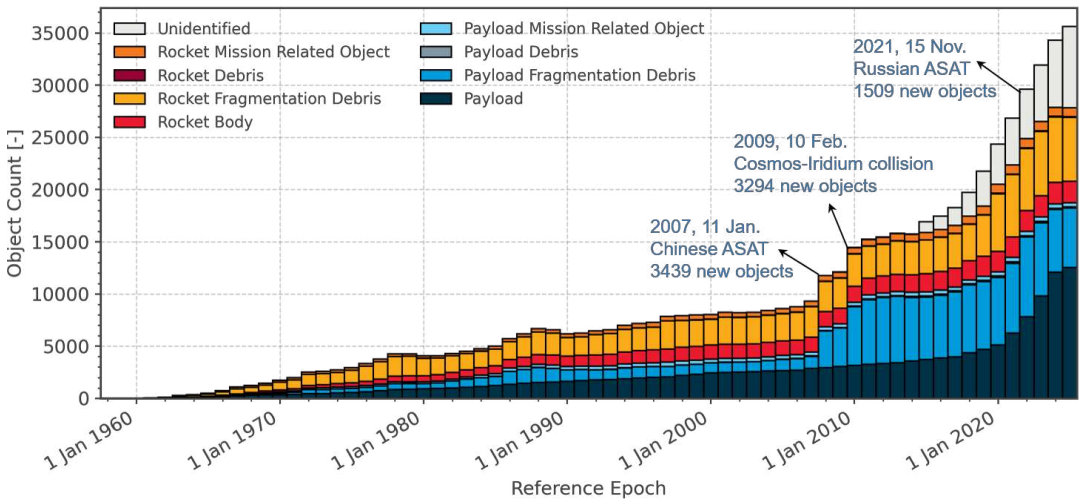

Fig. 1.2 Temporal evolution of trackable space objects, with major debris generation events highlighted. Adapted from [11]

1.2 Research motivations

Despite the large number of CAMs, the actual chances of a satellite being struck by debris large enough to cause appreciable damage are very low, and will remain so for at least the foreseeable future. ESA's MASTER-8 model [12] for the space debris environment predicts that the impact rate of objects larger than 1 cm on a cross-section of 30 m^2 orbiting at 800 km of altitude (i.e., the most crowded region) is once every 101 years on average [13]. The reason why satellites are in practice maneuvered much more frequently is that multiple uncertainties and error sources enter the decision-making process behind CAMs, forcing operators to take conservative actions. The inherent noises of surveillance sensors are one of the limits imposed on the accuracy to which the orbits of uncooperative objects can be determined. The impact of data accuracy on maneuver frequency is illustrated in the example of Fig. 1.3, where ESA's DRAMA software has been used to estimate the total number of CAMs required for a satellite over a 7-year lifetime, given varying accuracies for the orbital data available on the other objects. The spacecraft is modeled as a 2-meter sphere orbiting in a Sun-synchronous orbit at an altitude of 785 km, and maneuvers are decided using an Accepted Collison Probability Level (ACPL) defined based on achieving a risk reduction of >90%[1].

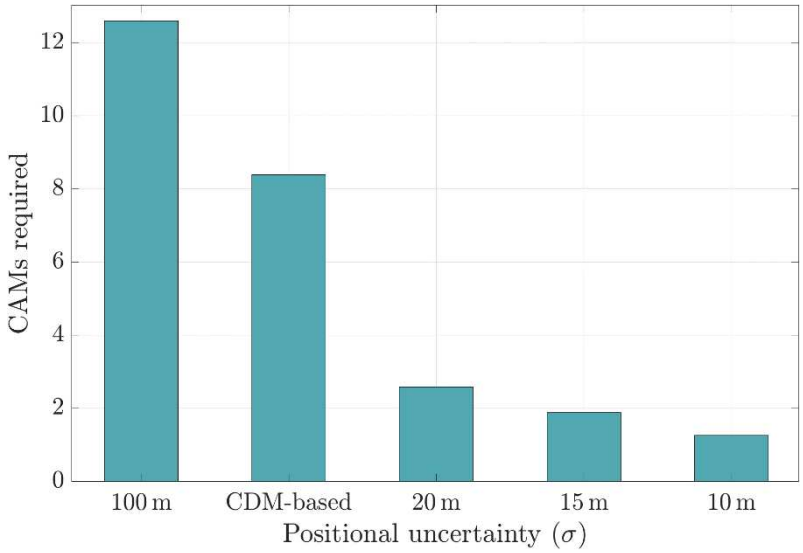

Fig. 1.3 Estimated number of CAMs required by a satellite over 7 years for varying levels of data accuracy on secondary objects. The accuracy is represented in terms root-mean-square (RMS) positional uncertainty (1-σ), which is assumed equal in each direction. "CDM-based" reflects the typical uncertainties present in Conjunction Data Messages (CDMs) [15], which are currently the standard for making maneuver decisions and thus can be seen as the current accuracy level.

Some experiments have shown that combining Space Situational Awareness

[1]The ACPL is a threshold on collision probability used for maneuver decisions. A >90% risk reduction strategy leads to ACPL values in between 10^{-4} and 10^{-5}. More information can be found in Section 3.2 of [14].

(SSA) data from different providers, including public and private ones as well as space operators, can substantially enhance the knowledge of objects' position and thus the accuracy of conjunction predictions [16, 17]. However, the establishment of a reliable, large-scale data-sharing framework is a complicated matter, since several behavioral and psychological barriers can intervene when it comes to sharing authoritative data between different countries. Political rivalries between governments, cross-cultural differences and the competitive and economic advantages of possessing unique SSA information are some of the factors hindering the process [18]. Another possibility, raised by several authors in the last decade, is to use ground-based laser ranging stations to make high-precision measurements of uncooperative RSOs and refine their positional accuracy [19, 20-22]. Although early studies have demonstrated the potential of this technique, different constraints reduce the possibilities of making valuable observations, such as weather conditions, targets illumination and stations availability [22, 23]. In parallel, solutions involving space-based sensors have recently gained interest as they overcome some limitations of their ground-based counterparts, such as the dependence on circadian rhythms and the presence of atmosphere-related problems (e.g., attenuation, absorption, turbulences) [24]. Most related research focuses on generally improving the current SSA capability by exploiting the unique observation possibilities available from space, for example by using in-situ sensors for the detection of uncatalogued millimeter-sized particles [25–27].

All these solutions aim to improve the accuracy of orbital solutions *at epoch*, which is the specific time at which an object's position and velocity is determined. However, even when small positional uncertainties are initially available for two objects, assessing their collision risk requires to propagate their states up to the predicted TCA. This involves using nonlinear dynamics models that account for orbital perturbations (i.e., solar radiation pressure, third-body perturbations, etc.), causing initial uncertainties to grow accordingly with the length of the propagation interval. For objects in LEO, errors associated with the atmospheric drag model constitute the largest source of propagation uncertainty [28]. This concept is illustrated in Fig. 1.4, which shows the size of the positional uncertainty of an object being propagated for different time spans. In the three-dimensional space, uncertainties are generally represented as ellipsoids [29].

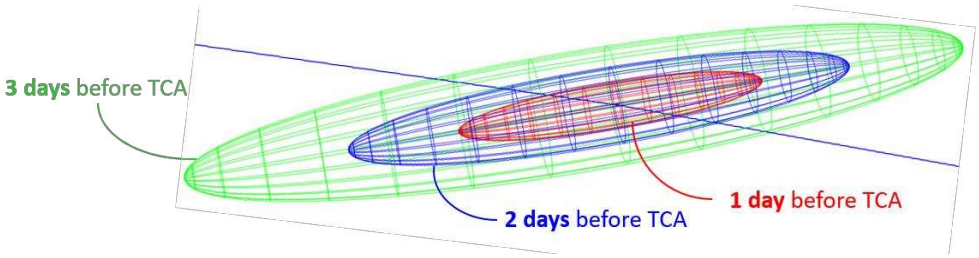

Fig. 1.4 Positional uncertainty of an object being propagated to the TCA starting from one, two, and three days prior. Generated through the STK software

Due to propagation uncertainties, assessing the collision risk well ahead of the TCA leads to lower confidence predictions. Depending on the case, this can result in either a high probability of false alarms or an artificially low probability

of collision (related to the "dilution region" effect [29]), which may create an equally dangerous false sense of safety. This often leads on-ground operators to wait as long as possible before making the final decision, aiming to obtain the most updated information on the objects' position. At ESA, roughly around one third of the times in which a CAM is already commanded to a satellite, new tracking data becomes available before TCA revealing that the collision risk has fallen below the maneuvering threshold. Considering that satellites in LEO generally have only a few daily ground-station accesses, and due to the practical time margins required to plan and uplink a command, not always canceling a decision is feasible, leading to unnecessary interruptions of satellite operations and fuel waste. This problem has also been reported to occur for SpaceX's Starlink satellites [7], for which crucial conjunction information sometimes becomes available when it is too late for timely update.

This problem has motivated space agencies and operators to explore various solutions that minimize the time gap between maneuver decision and TCA. As part of ESA's Collision Risk Estimation and Automated Mitigation (CREAM) initiative, an activity begun in 2024 aims at enabling alternative pathways for late commanding of CAMs by utilizing the Galileo system [30]. The solution, developed jointly by Astroscale UK and GMV, plans to leverage the Galileo Signal-in-Space and its Return Link Service to establish continuous communication channels with satellites that are equipped with Galileo-compatible GNSS receivers, allowing for late relay of CAM decisions [30]. Other strategies under investigation at ESA involve expanding the network of ground stations to increase satellite connectivity, or devolving part of the conjunction analyses – currently carried out on ground – directly to the satellites that are at risk of collision [31]. The latter approach allows late updates on hazardous objects to be directly sent to the at-risk satellites, bypassing the need for prior ground processing, which slows down the response time. This also reduces the need for human intervention, which is particularly advantageous when managing large fleets of spacecraft. Starlink satellites, for instance, were among the first to incorporate intelligent avoidance capabilities, which allows them to efficiently handle the frequent conjunction warnings they face [32].

In the previous solutions, at-risk satellites do not actively participate in collecting data on secondary objects. However, if equipped with suitable onboard sensors, satellites could autonomously gather and process additional data during the orbits before TCA. In this way, starting from initial positional estimates uplinked from ground, the onboard solution could be refined up until shortly before TCA – potentially half an orbit before – when predictions can be made with a higher confidence level.

Autonomous avoidance systems exploiting onboard sensors have already been proposed in the past [33], but they were tied to the idea of detecting the hazardous objects in the last minutes before TCA, which is a rather impractical and risky approach. In 2018, a joint on-orbit experiment by the Canadian Space

Agency and Defence R&D Canada revived interest in this concept by demonstrating that opportunities for such in-situ measurements may arise also well before the closest approach, allowing for much safer strategy [34]. The experiment was performed by NEOSSat, a 74-kg spacecraft equipped with a 15-cm aperture telescope, which was able to image several objects predicted for a close approach with it during the days before the conjunctions. As reported in [34], observation opportunities became available since most objects encountered NEOSSat multiple times and at relatively close distances prior to TCA. Despite the encouraging results, numerous challenges remain and significant R&D efforts are required this autonomous avoidance concept can be implemented on generic satellites, which not always embark on a suitable onboard payload.

1.3 Research objectives

Figure 1.5 conceptualizes the main steps required to take the considered avoidance system from a conceptual idea to a fully functioning system in orbit. In a fashion similar to "TRL0 to TRL9," the outlied pathway begins with the initial idea and moves through development stages like feasibility studies, design refinement, on-ground testing, and ultimately, real-world validation in space.

The preliminary design phase must bring out the many technical challenges involved in making this system concept viable. This includes feasibility studies to assess whether the system can realistically be built within current technological limits and a performance assessment to see if it genuinely offers any meaningful benefits over existing systems.

Once these aspects are reasonably confirmed, the focus shifts to optimizing the design of each system's functional block and harmonizing them into a fully structured system. On-ground testing must follow up to simulate space-like conditions more accurately, allowing for a better evaluation of the system's performance. This step is here particularly important for testing functional blocks where significant modeling uncertainties are present during the simulation work, such as the in-orbit detection process. As explained later, these two activities—design optimization and on-ground testing—are planned to be approached together, to allow design refinements to be informed by on ground test outcomes, and vice versa.

The final stage involves in-orbit testing, where the fully integrated system is deployed and its performance validated under real operational conditions. This step ensures the system functions reliably within the actual space environment and meets design expectations.

Referring to Fig. 1.5, the purpose of this thesis is to address the 'Preliminary design phase,' as well as laying the grounds for the other two. Feasibility and performance assessments can be broken down into the three main steps shown in the yellow box in Fig. 1.5, which address different technical aspects that are sequential and build upon one another.

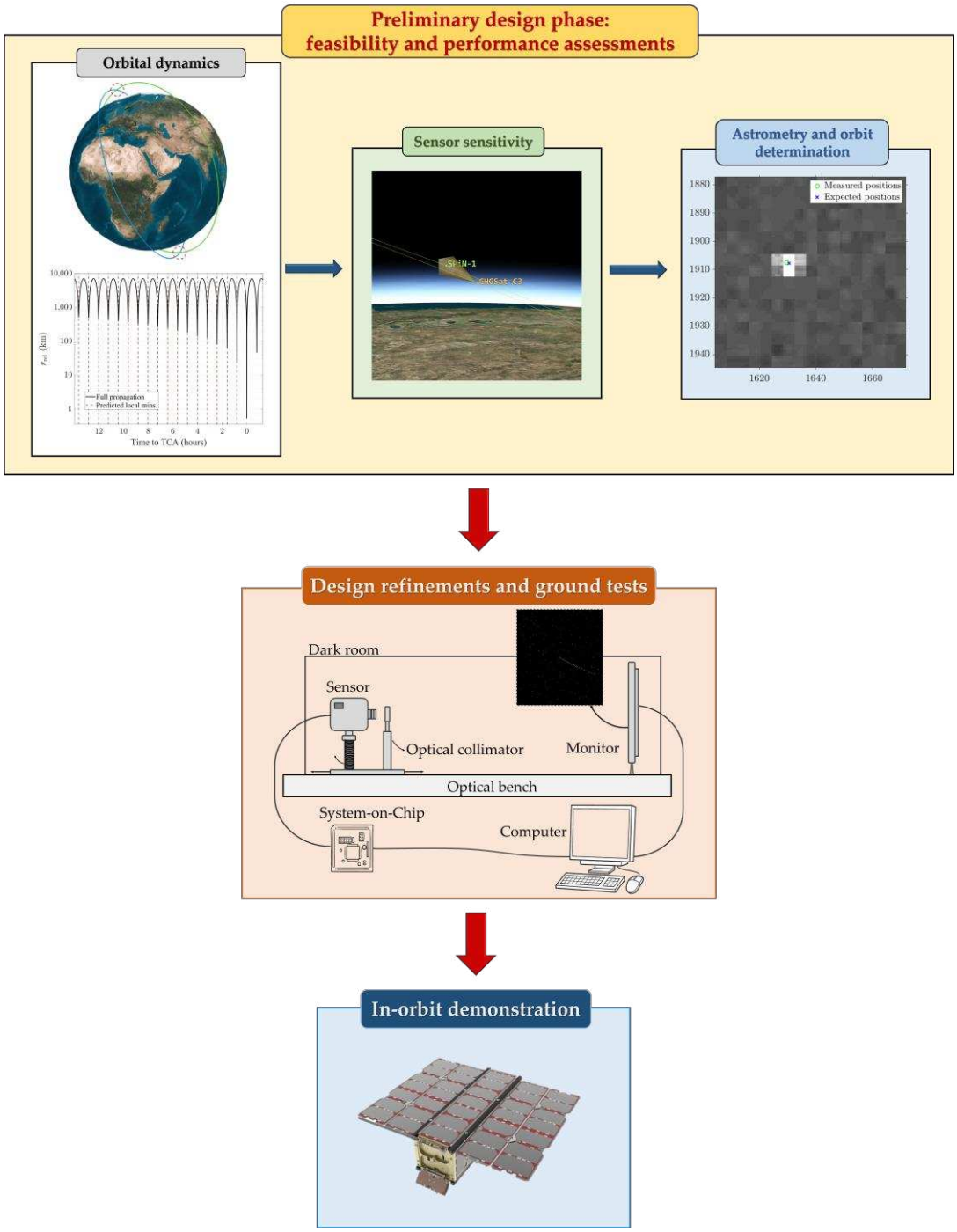

Fig. 1.5 Development pathway from idea to deployment, outlining the key stages from initial feasibility and performance assessment to on-ground testing, culminating in on-orbit mission deployment

In the first step, the concept is approached from an orbital dynamics perspective to assess how generalizable NEOSSat's results on space-based detection are and set the basis for an observation strategy. Specifically, the goal is to understand how frequently repeated encounters occur before TCA and to statistically characterize key features such as the relative distances and velocities involved. These features are essential for understanding the operational context in which the onboard sensor must function and for deriving its performance requirements. To this end, an analysis of the trajectory evolution of past

conjunction events during the two days leading to TCA is performed. Orbital data is extracted for about 22,000 conjuncting objects in the form of Two-Line Element (TLE) sets [35], and each trajectory is reconstructed using the Simplified General Perturbations 4 (SGP4) model [36], the analytical propagator designed for use with TLEs. The time evolution of the relative distance, relative velocity and angular rate is computed for each event, enabling to characterize several aspects of the encounters, such as their duration and the angular rates involved.

In the second step, the focus is shifted towards the definition of the sensor technology for the on-board payload. A state-of-the-art review on sensor technologies currently used for debris detection and tracking (e.g., radar, LiDAR, optical cameras) is carried out. Building on insights from the orbital dynamics study, requirements and performance standards for the sensor are defined to ensure successful debris detection. These include, for example, minimum detection thresholds and SWaP (Size, Weight, and Power) constraints. In this direction, the design strongly prioritizes leveraging existing sensors already onboard satellites. While adding a secondary payload is an option, it would introduce significant SWaP challenges, something operators would likely view unfavorably—especially those in the New Space sector who operate under tight SWaP budgets and cannot easily accommodate additional hardware. Potential sensing technologies are then screened based on their ability to meet the established requirements. For the best candidate, which occurs to be electro-optical sensors in this case, a more focused parametric study is performed to determine optimal sensor parameters. This is accomplished by simulating the sensor's operations in realistic scenarios. A Matlab–System Tool Kit (STK) modeling environment is established, where hundreds of real-world conjunctions between satellites and other objects are reconstructed. For each event, an onboard electro-optical sensor is modeled for the satellite and used to simulate observations of the secondary object in the pre-TCA time. Leveraging STK's Electro-Optical and InfraRed (EOIR) tool, synthetic images of the virtual scenes are generated and post-processed, to evaluate the Signal-to-Noise-Ratio (SNR) of the detection system. The probability of detection and observation quality is assessed for different possible low-to-medium performance sensors, to determine how well an already embarked sensor could be repurposed for the proposed avoidance concept.

Finally, the third step entails conducting Orbit Determination (OD) analyses for evaluating whether – and to what extent – successful in-orbit observations can lead to improvements in positional accuracy. A few conjunction case studies will be establisehd using the modeling environment of the previous step. For each simulated observation, orbital information about detected targets will be extracted, along with associated observation uncertainties. The tools and measurements used in this stage will depend on the chosen sensor technology. For example, with optical cameras, plate-solving tools must be employed to translate pixel coordinates into sky coordinates, ultimately providing measurements in terms of Right Ascension and Declination. These measurements will then be used to simulate the process of updating the trajectory estimation of the secondary object in orbit. OD methods, such as Least

Squares or Sequential Filters (e.g., Kalman filters), will be applied in this step. The ultimate goal is to assess the extent to which the designed system can enhance the current collision avoidance process.

1.4 Thesis outline

Chapter 2 offers a more in-depth description of the operational concept behind the proposed system. It begins by framing the system within the context of current collision avoidance practices, providing an overview that helps clarify the added value of the proposal and its compatibility with the existing framework. By breaking down the the collision avoidance process into three main elements—sensor data collection, data processing, and mitigation—the chapter provides a review of existing and planned sensor technologies for SSA, including space-based ones.

Chapter 3 initiates the system design using a requirements-driven approach, where system requirements are derived from high-level objectives and then refined through quantitative analysis that considers technical feasibility. Guiding this process, Section 3.1 emphasizes the strong need for an extensive analysis of the orbital dynamics of conjuncting objects in LEO, which is functional to quantify key system requirements. This analysis is presented in Section 3.2, with all steps fully described, including orbital data collection and propagation methods. Observation opportunities are examined in terms of relative distances, velocities, angular rates, time-to-first opportunity, average number and duration of observing windows, as well as azimuth and elevation angles. Section 3.2.5 provides a supplementary analysis of the reliability of these outcomes. Section 3.3 draws insights from these findings, leading to the decision that active technologies for the onboard sensor are unfeasible.

Chapter 4 shifts the focus to the sensing element and analyzes the detection performance of electro-optical sensors for varying hardware characteristics. Section 4.1 introduces the simulation framework of the analysis, detailing the models used, while Section 4.2 outlines the simulation parameters, their selection rationale, and the post-processing analyses. Section 4.3 presents the outcomes, and Section 4.4 summarizes key findings and meaningful insights.

Chapter 5 focuses on OD, aiming to evaluate potential trajectory improvements using data from onboard sensors. The chapter guides the reader through a series of tasks required for determining such improvements starting from raw images, including tasks such as astrometric reduction. A set of case studies demonstrates how real-time observations from electro-optical sensors can reduce positional uncertainty. Various sources of measurement uncertainty are analyzed and incorporated into the OD process using an Extended Kalman Filter.

Chapter 6 offers concluding discussions and remarks.

1.5 List of publications

Journal articles

[1] G. Campiti, G. Brunetti, V. Braun, E. Di Sciascio, C. Ciminelli, "Orbital kinematics of conjuncting objects in low-earth orbit and opportunities for autonomous observations," *Acta Astronautica*, vol. 208, 2023, pp. 355-366, doi: https://doi.org/10.1016/j.actaastro.2023.04.032

[2] G. Brunetti, G. Campiti, M. Tagliente and C. Ciminelli, "COTS devices for space missions in LEO," *IEEE Access*, vol. 12, 2024, pp. 76478-76514, doi: https://doi.org/10.1109/ACCESS.2024.3405373

[3] G. Campiti, G. Brunetti, C. Ciminelli, "Detectability of potentially colliding space objects through onboard cameras and star trackers," submitted to *IEEE Transaction on Aerospace and Electronic Systems*

Book chapters

[1] G. Campiti, M. Tagliente, G. Brunetti, M. N. Armenise, C. Ciminelli, "Debris detection and tracking through on-board LiDAR", in *Berta, R., De Gloria, A. (eds) Applications in Electronics Pervading Industry, Environment and Society. ApplePies 2022.* Lecture Notes in Electrical Engineering, vol 1036. Springer, Cham., 2023, https://doi.org/10.1007/978-3-031-30333-3_31

[2] G. Brunetti, N. Sasanelli, N. Saha, G. Campiti, F. Hassan, A. di Toma, M. N. Armenise, C. Ciminelli, "Integrated photonics for NewSpace," in *Berta, R., De Gloria, A. (eds) Applications in Electronics Pervading Industry, Environment and Society. ApplePies 2022*. Lecture Notes in Electrical Engineering, vol 1036. Springer, Cham., 2023, https://doi.org/10.1007/978-3-031-30333-3_39

Conference proceedings

[1] G. Campiti, G. Brunetti, F. Santoro, M. Reali, R. Vittori, M. N. Armenise, C. Ciminelli, "Feasibility assessment of an autonomous collision avoidance system for satellites," in *Proceedings of the 74th International Astronautical Congress (IAC)*, Baku, Azerbaijan, Oct. 2–6, 2023

[2] G. Campiti, G. Brunetti, C. Ciminelli, "A 3U Cubesat mission to image potentially colliding objects," in *Proceedings of the Small Satellite Systems and Services (4S) Symposium*, Palma de Mallorca, Spain, May 27-31, 2024

Workshop presentations

[1] G. Campiti, G. Brunetti, C. Ciminelli, "Observing opportunities of space conjuncting objects in the orbits prior to the closest approach", in *Space Debris Risk Assessment and Mitigation Analysis Workshop*, European Space Operation Center (ESOC), Darmstadt, Germany, Jun. 23-24, 2022

[2] G. Campiti, G. Brunetti, C. Ciminelli, "Sistema di anti-collisione autonomo per satelliti in LEO," in *L'Impegno Italiano nel Settore dei CubeSat: Tecnologie e Missioni Future – 2° Edizione*, Italian Space Agency (ASI), Rome, Italy, Jul. 2-4, 2024

Posters

[1] M. Tagliente, G. Campiti, G. Brunetti, M. N. Armenise, C. Ciminelli, "Spaceborne LiDAR for debris detection and tracking," poster for the *SIE 2022 – 53rd Annual Meeting of the Associazione Società Italiana di Elettronica*, Pizzo, Italy, Sep. 7-9, 2022

[2] G. Campiti, G. Brunetti, C. Ciminelli, "A 3U Cubesat mission to image potentially colliding objects," poster for the *Small Satellite Systems and Services (4S) Symposium*, Palma de Mallorca, Spain, May 27-31, 2024

References

[1] Our World in Data, "Annual number of objects launched into space", Accessed Jun 19, 2024. [Online]. Available: https://ourworldindata.org/space-exploration-satellites

[2] United Nations Office for Outer Space Affairs (UNOOSA), "Online index of objects launched into outer space," Accessed: Jun 19, 2024. [Online]. Available: https://www.unoosa.org/oosa/osoindex/search-ng.jspx

[3] ESA.int, "Space debris by the numbers," Accessed: Jun 19, 2024. [Online]. Available: https://www.esa.int/Space_Safety/Space_Debris/Space_debris_by_the_numbers

[4] D.J. Kessler, B.G. Cour-Palais, "Collision frequency of artificial satellites: The creation of a debris belt," *Journal of Geophysical Research: Space Physics*, vol. 83, no. 6, 1978, pp. 2637-2646, doi: https://doi.org/10.1029/JA083iA06p02637

[5] National Air and Space Museum, Smithsonian Institution, "Radiator End of Wide Field Planetary Camera II (WFPC2)," Accessed: Jun 19, 2024. [Online]. Available: https://airandspace.si.edu/multimedia-gallery/6572hjpg#:~:text=This%20image%20shows%20the%20radiator,the%20result%20of%20space%20debris

[6] European Space Agency, "ESA & UNOOSA space debris infographics and podcast," 2024, Accessed Jan 25, 2024. [Online]. Available: https://www.esa.int/Space_Safety/Space_Debris/ESA_UNOOSA_space_debris_infographics_and_podcast

[7] SpaceX, "SpaceX constellation status report, december 1, 2022 – May 31, 2023," SpaceX, Washington, DC, USA, Tech. Rep., 2023

[8] Space.com, "SpaceX's Starlink satellites are dodging debris and each other in orbit as growth stalls," Accessed Apr 17, 2024. [Online]. Available: https://www.space.com/spacex-starlink-collision-avoidance-maneuver-growth-stalls

[9] NASA Orbital Debris Program Office, "Orbital debris quarterly news – Volume 27, Issue 4, Oct 2023," Accessed Oct 16, 2024. [Online]. Available: https://orbitaldebris.jsc.nasa.gov/quarterly-news/pdfs/ODQNv27i4.pdf

[10] European Space Agency, "Sentinel Online – News," Accessed Oct 16, 2024. [Online]. Available: https://sentinels.copernicus.eu/web/sentinel/-/copernicus-sentinel-1a-collision-avoidance-manoeuvres-on-16-may-2022/1.1

[11] ESA Space Debris Office, "ESA's annual space environment report," European Space Operation Center (ESOC), Darmstadt, Germany, Tech. Rep. GEN-DB-LOG-00288-OPS-SD, v.7, 2023

[12] V. Braun, A. Horstmann, S. Lemmens, C. Wiedemann, L. Böttcher, "Recent developments in space debris environment modelling, verification and validation with MASTER," in *8th European Conference on Space Debris*, Darmstadt, Germany, 2021

[13] J. Siminski, "Online Space Debris Training Course 2022, Lecture one: introduction," Lecture, ESA Space Debris Office, Darmstadt, Germany, 2022

[14] ESA Space Debris Office, "Collision avoidance requirements verification and guidelines based on DRAMA/ARES," European Space Operation Center (ESOC), Darmstadt, Germany, Tech. Rep. MIT-COL-MAN-00279-OPS-SD, v.1.1, 2020

[15] Consultative Committee for Space Data Systems (CCSDS), "Conjunction Data Message (Blue Book)," Standard CCSDS 508.0-B-1, Washington, D.C., USA, 2013

[16] L. Mariani, G. Zarcone, F. Santoni, G. Bianchi, M. Acernese, M.F. Montaruli, P. Di Lizia, F. Piergentili, F. Curianò, S.H. Hossein, "Enhancing the knowledge on space debris attitude and position combining radar and optical observations," in *8th European Conference on Space Debris*, Darmstadt, Germany, 2021

[17] D.L. Oltrogge, P. Wauthier, D.A. Vallado, S. Alfano, T.S. Kelso, "Results of comprehensive STCM data fusion experiment," in *8th European Conference on Space Debris*, Darmstadt, Germany, 2021

[18] K.M. Keller, D. Yeung, D. Baiocchi, W. Welser IV, "Facilitating information sharing across the international space community: lessons from behavioral science," RAND Corporation, Santa Monica, CA, USA, Tech. Rep., 2013. [Online]. Available: https://www.rand.org/pubs/technical_reports/TR1255.html

[19] S.J. Setty, T. Flohrer, H. Krag, "SLR for space debris monitoring: an analysis on requirements and achievable orbit improvement," in *1st NEO and Debris Detection Conference*, Darmstadt, Germany, 2019

[20] D. Vallado, J. Woodburn, F. Deleflie, "Sequential orbit determination using satellite laser ranging," *Advances in the Astronautical Sciences Series*, vol. 152, 2014, pp. 1273–1290

[21] N. Bartels, P. Allenspacher, D. Hampf, B. Heidenreich, D. Keil, E.

Schafer, W. Riede, “Space object identification via polarimetric satellite laser ranging,” *Communication Engineering*, vol. 1, no. 5, 2022, doi: https://doi.org/10.1038/s44172-022-00003-w

[22] C. Bamann, U. Hugentobler, “Accurate orbit determination of space debris with laser tracking,” in *the 7th European Conference on Space Debris*, Darmstadt, Germany, 2017

[23] E. Cordelli, A. Vananti, T. Schildknecht, "Analysis of laser ranges and angular measurements data fusion for space debris orbit determination", *Advances in Space Research*, vol. 65, no. 1, 2020, pp. 419-434, doi: https://doi.org/10.1016/j.asr.2019.11.009

[24] D. Spiller, E. Magionami, V. Schiattarella, F. Curti, C. Facchinetti, L. Ansalone, A. Tuozzi, “On-orbit recognition of resident space objects by using star trackers,” *Acta Astronautica*, vol. 177, 2020, pp. 478–496, doi: https://doi.org/10.1016/j.actaastro.2020.08.009

[25] R. Ahmed, N. Majurec, J.W. De Bleser, “A Cubesat-based radar for characterization of millimetric orbital debris,” in *The First International Orbital Debris Conference (IOC)*, Sugar Land, TX, USA, Dec. 9–12, 2019

[26] D. Cerutti-Maori, J. Rosebrock, L. Leushacke, H. Krag, “Preliminary concept of a space-based radar for detecting mm-size space debris,” in *7th European Conference on Space Debris*, Darmstadt, Germany, 2017

[27] C.R. Englert, J. Timothy Bays, K.D. Marr, C.M. Brown, A.C. Nicholas, T.T. Finne, “Optical orbital debris spotter,” *Acta Astronautica*, vol. 104, no. 1, 2014, pp. 99–105, doi: https://doi.org/10.1016/j.actaastro.2014.07.031

[28] J. R. Shell, “Optimizing orbital debris monitoring with optical telescopes,” in *Advanced Maui Optical and Space Surveillance Technologies Conference (AMOS)*, Maui, HI, USA, 2010

[29] A. B. Poore, J. M. Aristoff, J. T. Horwood, R. Armellin, W. T. Cerven, Y. Cheng, C. M. Cox, R. S. Erwin, J. H. Frisbee, M. D. Hejduk, B. A. Jones, P. Di Lizia, D. J. Scheeres, D. A. Vallado, R. Weisman, “Covariance and uncertainty realism in space surveillance and tracking,” Numerica Corporation, Fort Collins, CO, USA, Tech. Rep., 2016

[30] GMV News, No. 88, “Galileo PRS service as an essential element of resilient PNT,” p.31. Accessed Oct 13, 2024. [Online]. Available: https://www.gmv.com/sites/default/files/content/file/2024/01/25/114/gmv_news_88_0.pdf

[31] K. Mertz, “Online Space Debris Training Course 2022, Lecture 11: colllision avoidance,” Lecture, ESA Space Debris Office, Darmstadt, Germany, 2022

[32] SpaceX, “Starlink orbital space safety,” Aug 2021, Accessed: Oct 15, 2024. [Online]. Available: https://forum.nasaspaceflight.com/index.php?PHPSESSID=tu14od0adpt8lrslne9nr33tug&action=dlattach;topic=48297.0;attach=2054365;sess=0

[33] R. Briskman, “Autonomous satellite orbital debris avoidance system and

method," U.S. Patent no. 8,833,702 B2, U.S. Patent and Trademark Office, 2012

[34] R. L. Scott, S. Thorsteinson, V. Abbasi, "On-orbit observations of conjuncting space objects prior to the time of closest approach," *Journal of Astronautical Sciences*, vol. 67, no. 4, 2020, pp. 1735–1754, doi: https://doi.org/10.1007/s40295-020-00236-x

[35] D. Vallado, P. Cefola, "Two-line element sets — practice and use," in *63rd International Astronautical Congress (IAC)*, Naples, Italy, 2012, pp. 5812–5825

[36] D. Vallado, P. Crawford, R. Hujsak, T.S. Kelso, "Revisiting spacetrack report #3," in *AIAA/AAS Astrodynamics Specialist Conference and Exhibit*, Keystone, CO, USA, 2006

Chapter 2

Spacecraft collision avoidance: current pipeline and proposed approach

Adopting a new strategy to avoid collisions in the multi-faceted context of Space Traffic Management (STM) requires careful consideration of various factors beyond just technical feasibility. These include – but are not limited to – compatibility with the current STM landscape and evolving trends in the industry, as well as potential conflicts with existing policies and emerging regulatory frameworks. The need to consider the broader picture comes from acknowledging that one satellite's action has implications for the other space assets, so a new system cannot be developed independently from the operational framework it exists within. Before delving into the details, it is helpful to break down the components of collision avoidance processes.

2.1 The collision avoidance pipeline

Avoiding a collision in space is a complex process that involves a series of interconnected steps and multiple actors and infrastructures. While the specifics may vary depending on the satellite (e.g., the maneuver decision may be made on the ground or autonomously onboard), a few core elements remain consistent throughout the entire process: sensor data collection, data processing, and mitigation.

2.1.1 Sensor data collection

The first ingredient of collision avoidance is the collection of observational data on orbiting objects, which is essential to gain knowledge of the space traffic and predict its future behavior. Two commonly used terms in this context are Space Situational Awareness (SSA) and Space Surveillance and Tracking (SST). Although global harmonization lacks in STM terminology [1], which often leads to ambiguity, SST is generally defined as "the detection, tracking, monitoring, cataloging and prediction of the movement of space objects, and the identification and alerting of derived risks" [1]. Thus, SST not only involves the collection of sensor data but also the processing of this data to provide actionable insights and services for collision avoidance, such as conjunction risk assessments. Building on SST, the SSA definition encompasses a broader understanding of the entire space environment by

integrating additional factors such as space weather conditions, including the radiation environment and solar activity, as well as situational awareness about Near-Earth Objects (NEO).

The current sensor infrastructure for SSA is predominantly ground-based, with the United States (U.S.) historically leading in these capabilities through extensive sensor networks like the Space Surveillance Network (SSN), operated by the U.S. Space Force (USSF). The SSN's origins trace back to the late 1950s, following the launch of the first satellites, when the need to track these new objects led to the practical repurposing of existing ground-based sensors that were originally designed for purposes such as missile tracking and astronomical observations [2]. The European counterpart of the SSN is the EU SST (European Union Space Surveillance and Tracking) network, involving the collaboration of 15 member states that collectively contribute with 36 ground-based sensors, including 9 radars (3 for surveillance and 6 for tracking) and 27 optical telescopes (16 for surveillance and 11 for tracking) [3]. So far, ground-based sensors have been favored due to their technological maturity, ease of maintenance, and cost-effectiveness, making them more widespread compared to space-based systems, which remain a newer and developing concept.

Existing sensors are based on the following technologies: electro-optical, radar, passive RF, and laser ranging, although the latter is still in the developmental stages.

2.1.1.1 Electro-optical sensors

Electro-optical sensors operate by capturing visual data from space using telescopes and cameras that are sensitive to visible, infrared, or ultraviolet light. They are generally the most cost-effective and versatile among SSA sensors, which is why they have played a dominant role in this field since their early adoption. The application of electro-optical sensor to the SSA field was pioneered at MIT's Lincoln Laboratory in the late 1970s, leading to the deployment of the Ground-Based Electro-Optical Deep Space Surveillance (GEODSS) system by the U.S. Air Force [4].

In terms of performance, Commercial-Off-The-Shelf (COTS)-based optical systems, deployed globally, can detect objects fainter than ~16 visual magnitudes (m_v). The visual magnitude refers to a widely adopted scale used to measure the brightness of objects in the sky, where lower magnitudes indicate brighter objects. For reference, a sunlit golf ball at an altitude of 1,000 km would have a magnitude of approximately 14. By comparison, government-owned telescopes like the Space Surveillance Telescope (SST) from the SSN, shown on the left in Fig. 2.1, can detect objects as faint as 20.5 m_v [5]. It is impossible to list all operating telescopes globally, but a notable example is the Mini-MegaTORTORA (MMT-9). Despite its limited accuracy, it provides invaluable, publicly available data, including light curves, measurements, and orbital determination.

Despite their good performance, electro-optical sensors operations are hindered by atmospheric conditions and the need for illumination, limiting their effectiveness during cloudy weather or for objects in Earth's shadow. To effectively track objects in LEO, electro-optical sensors must operate during twilight hours—just after sunset or before dawn—when the Sun is below the horizon but still illuminating the objects.

This restricts the operational window to about three hours per day, which can be further shortened by unfavorable weather. Daylight tracking of objects in LEO is an active area of research, but it has not been been widely employed yet due to several challenges, such as overcoming the interference from the bright sky background. An interesting line of research in this direction is the use of neuromorphic cameras, currently being explored at the University of Sydney.

Additionally, many of the most debris-filled orbits are Sun-synchronous, meaning the debris remains in orbits where twilight conditions are often only present at high latitudes near the poles. As a result, effective optical tracking would require a large number of observation sites spread globally, including at extreme northern and southern latitudes, where conditions are often unsuitable for such observations. Due to these limitations, consistent optical monitoring of space debris in LEO from the ground has proven unfeasible so far.

For these reasons, this technology remains the primary method for tracking objects in Geosynchronous Earth Orbit (GEO). Exceptions exist: some SSN optical sites are occasionally capable of tracking objects in LEO, Medium Earth Orbit (MEO), and Highly Elliptical Orbit (HEO), depending on factors like angular motion and solar illumination [5]. Additionally, companies such as Numerica Corp. have repurposed some previously GEO-focused telescopes to support LEO observations and deployed some purposed ones [6]. Those telescopes have been subsequently bought by Slingshot Aerospace, which expanded its optical network by deploying other purpose-built sensors, such as the one shown on the right of Fig. 2.1, achieving more than 150 globally [7].

In terms of geographical distribution, ground-based electro-optical sensors for SSA have traditionally been concentrated in countries with advanced space programs, such as the United States and European nations. However, there is a growing trend to strategically deploy these sensors worldwide, driven by nations aiming to contribute to global SSA frameworks and reduce reliance on a single source of data. Increasingly, countries outside traditional space powers are investing in SSA sensors, particularly in the Southern Hemisphere, to support this goal [8].

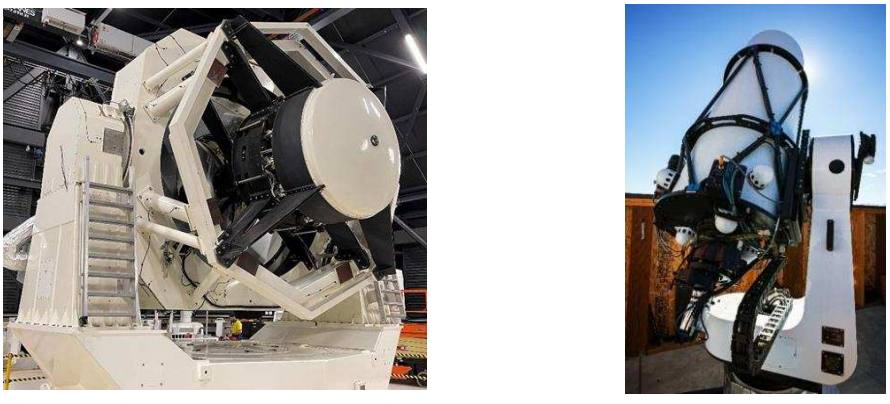

Fig. 2.1 *Left*: The Space Surveillance Telescope (SST), equipped with a 3.5-meter primary mirror, capable of detecting softball-sized objects in GEO [credits: USSF]. *Right*: "Aquila," a narrow field-of-view telescope from Slingshot Aerospace, capable of day and night operations, monitoring objects from LEO to GEO [credits: Slingshot Aerospace]

2.1.1.2 Radar systems

Radar systems utilize radio waves to detect and track objects in space, functioning independently of lighting conditions, making them particularly valuable for tracking objects in LEO and beyond. These systems are not reliant on illumination like electro-optical sensors and can operate in all weather conditions. Ground-based radar systems have been a backbone of SSA due to their ability to detect both cooperative (e.g., active satellites) and non-cooperative (e.g., debris) targets, including small objects that might otherwise be missed by optical systems.

The SSN, for instance, incorporates extensive radar systems that have been crucial for cataloging objects in orbit. However, as the number of objects in space increases, radar systems are being pushed to their limits. Emerging trends in radar technology are include moving toward bistatic and multistatic radar systems, which involve multiple antennas working together to track objects over a larger area and with greater precision. One example of this is BIRALES (Bistatic Radar for LEO Survey) [9], a recently developed bistatic radar system by the Italian National Institute for Astrophysics (INAF) and the University of Bologna. BIRALES, whose receiving antennas are shown in Fig. 2.2, was developed as part of the EU SST framework.

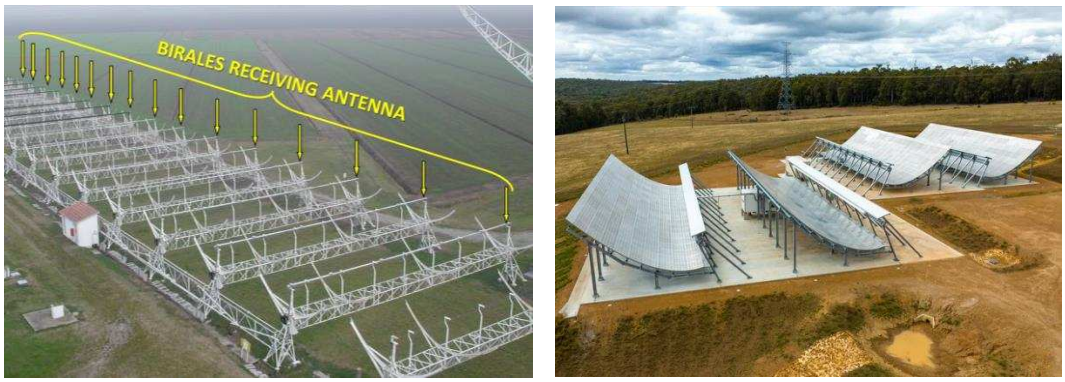

Fig. 2.2 *Left*: BIRALES receiving antennas, located in Medicina, Italy (near Bologna) [credits: [9]]. *Right*: LeoLabs' "West Australian Space Radar", shaped like a halfpipe [credits: LeoLabs].

Another emerging trend in SSA radar technology includes the development of smaller, more cost-effective radars that can be deployed in remote regions. This will enable better global coverage, particularly in the southern hemisphere, which has been historically underrepresented in SSA efforts.

Currently, the world's most advanced SSA radar system is the U.S. Space Fence, located in the Marshall Islands and operational since March 2020. Utilizing a highly sensitive S-band radar, it can track objects smaller than 10 cm [10], surpassing the capabilities of previous systems. The Space Fence is able to track approximately 200,000 objects and generates around 1.5 million observations per day.

Due to the significant distance of the GEO orbital regime from the Earth's surface, radar tracking of GEO objects requires prohibitively high transmitting power. This limitation has largely confined radar systems to LEO applications, though a few specialized radars can reach and track GEO objects, but these are generally limited to special collections [5].

Additionally, their high cost and complex infrastructure have limited their widespread adoption, with most systems primarily concentrated in few countries with significant military and space capabilities, such as the U.S. Europe has multiple radar systems distributed across member states, including France's GRAVES and Germany's TIRA. Russia operates an extensive radar network with roots in its Cold War-era missile warning and defense systems. In Asia, countries like Japan and India are expanding their radar capabilities, with systems like JAXA's debris monitoring radars and India's Multi-Object Tracking Radar (MOTR).

The high costs associated with radar deployment are the primary reason commercial radar networks remain less prevalent compared to their optical counterparts. A key exception is LeoLabs, which has established a global network of phased-array radars – one of which is shown on the right in Fig. 2.2 – capable of tracking debris as small as 2 cm [10].

2.1.1.3 Passive RF sensors

Passive RF sensors detect radiofrequency emissions from space objects, relying on the signals naturally emitted by active spacecraft. These sensors are less resource-intensive than radar or laser-based systems, as they do not require active signal transmission, and unlike optical systems, they operate effectively in all weather and lighting conditions. By cross-referencing RF signals collected at multiple ground-based antennas, these systems can accurately calculate the orbit of a satellite. This is similar to how GPS receivers work but in reverse. Time-synchronized captures of RF signals from different antennas allow the calculation of range and velocity through Time Difference of Arrival (TDOA) and Frequency Difference of Arrival (FDOA) methods. With RF measurements, a satellite's orbit can be estimated even with data from just one ground station. This is achieved by combining Doppler and interferometry measurements. For instance, using two antennas at a single ground station allows for interferometry data to complement Doppler data, significantly improving orbit estimation accuracy. This setup provides enough information to estimate the position and velocity of LEO satellites during a single pass, even in the presence of noise and bias [11]

Given their limitation to track active space assets, RF systems are best leveraged when in conjunction with other tracking systems, complementing them with unique features possible only with this method. For example, passive RF sensors can detect satellite maneuvers in real-time, even when traditional optical and radar sensors fail, such as during weather disruptions or solar exclusion windows. This is accomplished by capturing and analyzing shifts in the RF signal's frequency caused by the satellite's acceleration, which may indicate a change in its orbital trajectory. This is critical for identifying both minor station-keeping maneuvers and larger adjustments, which impact the satellite's orbit [12]. This becomes even more significant in light of recent assessments suggesting that maneuvers are likely the most dominant source of error in SSA solutions [13].

In addition to detecting maneuvers, passive RF sensors play a role in maintaining the resilience of satellite communication systems. In fact, they can identify

interference in command and control (C2) links, including intentional jamming (where malicious actors disrupt communication) and piracy (where signals are intercepted or misused) [14]. If an adversary tries to disrupt these signals through deliberate interference or unauthorized access, the sensors detect anomalies in the RF signal patterns. Other important anomalies that can be detected through passive RF include irregularities in a satellite's behavior. By continuously monitoring signals and establishing a "pattern of life" for a satellite, RF data can indicate deviations that may signal equipment malfunctions. A notable example of this occurred in 2017 when the AMC-9 satellite anomaly was first detected through the loss of all carriers across its transponders, alerting operators before optical systems could confirm the event [12].

Though passive RF sensors cannot track non-transmitting objects such as debris, they are becoming increasingly valuable as the number of small satellite constellations grows. As these systems generate vast amounts of data, advancements in machine learning are being explored to process the information more efficiently. Moreover, RF sensor accuracy is particularly high in geostationary orbits, where ground-based radar and optical sensors often face precision limitations. For instance, Kratos' Global Sensor Network (KGSN), comprising over 140 RF sensors worldwide (see Fig. 2.3), provides real-time data that can pinpoint satellite locations with an accuracy within 100 meters.

Fig. 2.3 An antenna from the KGSN [credits: Kratos Defense & Security Solutions]

Compared to radar- or laser-based systems, RF systems are less resource-intensive as they rely on passive detection rather than actively transmit signals. Compared to optical systems, they operate regardless of weather conditions and illumination conditions.

2.1.1.4 Laser ranging systems

Laser ranging systems represent the most precise method of tracking space objects. By emitting a laser pulse and measuring the time it takes to return after reflecting off an object, these sensors can calculate the object's distance with incredible accuracy, often to within millimeters [8]

Laser ranging is primarily used to track large, cooperative objects in space, such as

active satellites equipped with retroreflectors. It is less effective for tracking debris or non-cooperative targets, as few objects are naturally reflective enough to return a laser pulse. However, significant research is focused on developing high-power laser systems capable of illuminating and tracking smaller objects without the need for retroreflectors, although deploying such systems remains a technical challenge. Some stations, like ESA's Izaña-1 laser ranging station (IZN-1) in Tenerife, are being established for this purpose [15]. The IZN-1 station, illustrated in Fig. 2.4, currently uses a 150 mW laser to track satellites with retroreflectors, but it is scheduled for an upgrade to a a 50 W infrared laser that will allow tracking of uncooperative targets, including space debris and older satellites without retroreflecting patches. Interestingly, the station employs a Laser Traffic Control System (LTCS) to prevent interference with aircraft, satellites, and telescopes. This system ensures lasers don't endanger pilots or disrupt astronomers' observations, highlighting ESA's commitment to operational safety.

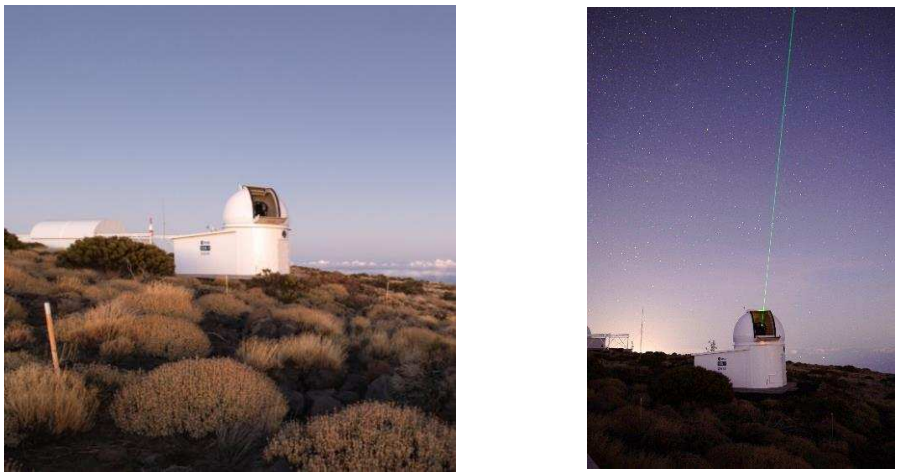

Fig. 2.4 ESA's The IZN-1 laser ranging station in Tenerife [credits: ESA]

Currently, laser ranging is still not as fully established as the other technologies in the SSA field due to challenges such as atmospheric interference and the need for highly specialized equipment. However, laser systems are becoming more integrated into global SSA infrastructures. A notable example is the International Laser Ranging Service (ILRS), a global cooperative effort with stations in the U.S., Europe, and Asia that contribute to highly precise orbital data and are especially useful for calibrating other types of SSA sensors.

SLR stations are still few nowadays, so there's the need for expanding SLR infrastructure to increase the number of tracking stations globally, which struggle to expand as these stations are expensive (millions of euros per station) [16].

The main limitation of this technology is its current inability to function in adverse weather conditions, as clouds and atmospheric particles can easily disrupt laser paths [17]. Other operational limitations include the need for accurate ephemeris[2] data to keep targets within the field of view of these sensors, which is much

[2] An ephemeris is essentially a table including the position and velocity of a spacecraft at specific, usually equally spaced, times over a set period. It may also optionally include covariance data, which represents position and velocity uncertainties.

narrower compared to other sensors [18]. Moreover, laser tracking is significantly more difficult during daylight hours due to increased noise from scattered solar photons. Some strategies to mitigate these effects are band-pass and temporal filters, which help extend observation windows into daylight hours [19].

2.1.1.5 Space-based sensors

The potential of using space-based sensors for detecting and tracking Resident Space Objects (RSOs) was first demonstrated in 1996 with the deployment of the Space-Based Visible (SBV) sensor aboard the Midcourse Space Experiment (MSX) satellite. This system, equipped with a visible imaging charged-coupled device (CCD), allowed for the tracking of RSOs by distinguishing them from a star-filled background [4]. Its success marked a critical milestone in the use of onboard satellite sensors for SSA.

There are several advantages in observing RSOs from space rathrer than from ground. Free from the constraints of atmospheric distortion, weather, and the day-night cycle, space-based sensors can provide continuous, high-quality observations. Positioned closer to RSOs, they experience less radiometric loss, enabling higher sensitivity and better detection capabilities, particularly in GEO, which is difficult for ground-based systems to observe. Systems like the Space-Based Space Surveillance (SBSS) and the Geosynchronous Space Situational Awareness Program (GSSAP) have proven effective in detecting smaller objects and monitoring high-orbit regions. The ability of space-based sensors to operate independently of weather-related disruptions further enhances their value for maintaining uninterrupted surveillance. It is also worth noting that these systems, once deployed, provide coverage without needing permissions or agreements from individual nations; in contrast, the installation of ground-based sensors may be subject to political negotiations, international agreements, or restrictions imposed by host countries.

However, these systems are not without drawbacks. Space-based sensors are expensive to develop, deploy, and maintain [5]. Unlike ground-based systems, they cannot be easily upgraded or repaired once in orbit, leading to higher costs and the need for full replacements as the sensors degrade in the harsh space environment. Additionally, space-based sensors often face bandwidth limitations, slowing down the transmission of data to the ground, which can reduce the real-time applicability of their observations.

The same sensing technologies employed on-ground have been investigated for use in orbit. Concerning space-based radars, a few concepts dedicated to SSA have been developed or proposed but, as of now, they have not been launched or operational. This is mainly due to their challenging requirements in terms of Size, Weight, and Power (SWaP) consumption. Based on theoretical results, spaceborn radars would be well-suited for identifying and characterizing small particles. Debris in the size range of 1 mm to 10 cm, which is abundant in LEO, can significantly damage spacecraft subsystems or cause catastrophic failures. Ground-based radars typically track debris larger than 10 cm, leaving a critical gap for smaller particles, which could be filled from space.

Proposed radar systems are designed to operate at relatively short ranges, dictated by the need for high sensitivity and the limited power and size constraints of space-based platforms. The one described by [20], with a mass limit of 10 kg, is calculated to detect millimeter-sized objects at distances up to 500 meters, while the one in [21], intended for CubeSat platforms, is estimated to detect debris at a maximum range of 100 meters. In terms of techniques, coherent pulse radars can detect and differentiate between objects at various ranges and velocities, but they are complex and consume significant power. On the other hand, Continuous Wave (CW) radars are simpler in design, but cannot measure the range to the target directly, which is a significant limitation. In fact, as the radar transmits continuously, it is difficult to determine how far away an object is because there is no clear "time of flight" measurement as with pulsed radars. A potential mitigation for this involves using multiple antennas on the same platform, which, despite their small distance, can be exploited to do Doppler shift interferometry and derive information about range to the target [21].

Although they are still in their infancy, electro-optical sensors represent a more consolidated option in space thanks to their much more compact and low-power designs. All past spacecraft missions with SSA-related goals – a list of which is provided in Table 1.1 along with planned similar missions – include electro-optical sensors on-board.

Compared to telescopes on ground, in space you get rid of atmospheric distortions, such as diffraction, aberrations, turbulences, and scattering, and the sky background can be up to 100 times fainter, especially when observing away from the ecliptic, which reduces background noise and shifts the detection limit to the sensitivity of the sensor itself [22]. However, there are smaller optics and limited detector options available on space platforms due to the harsh radiation environment. Thanks to continuous advancements miniaturization and cost reduction of optical sensor technologies, the trend toward deploying more optical sensors in orbit is gaining momentum.

2.1.2 Data processing

The data processing part includes all aspects of handling raw observation data and transforming it into meaningful information for collision avoidance. This involves creating and maintaining catalogs of RSOs with trajectory information (e.g., ephemeris and covariance data), screening predicted trajectories of RSOs against one another to identify potential collisions, performing conjunction risk assessments, and other analytical tasks.

The most widely used catalog in the world is generated and maintained by the U.S. 18th Space Defense Squadron (SDS), a unit of the U.S. Space Force (USSF) that controls SSN operations. The 18th SDS maintains the High Accuracy Catalog (HAC), a precise database of RSOs that leverages SSN observational data [40]. Trajectory information are routinely updated by performing Orbit Determination (OD) using fresh observations and predictive ephemeris are generated by propagating the orbits with Special Perturbations (SP) methods. Based on the 18th SDS catalog, the 19th

SDS, another USSF unit, executes trajectory screenings and conjunction risk assessment functions.

Table 2.1 Overview of past, present and future SSA/SDA/SST missions

Launch Year	Name of the satellite / constellation	O/O	Mass [kg]	Orbit	Payload info	Ref.
1996	Midcourse Space Experiment (MSX)	U.S. Ballistic Missile Defense Office	78	SSO, 898 km	Telescope, 15-cm aperture, 1.4×6.6 deg	[23], [24]
2003	MOST (Microvariability and Oscillations of STars)	Canadian Space Agency	54	Dawn-dusk SSO 830 km	Telescope, 15-cm aperture, 14×48 arcmin	[25]
2009	Space Tracking and Surveillance System-Demonstration (STSS-D) (constellation, 2 satellites: STSS-1 and STSS-2)	U.S. Missile Defense Agency through U.S. Air Force	~1000	SSO, 1350 km	Electro-optical and infrared	[26], [27]
2010	Space-Based Space Surveillance Block 10 (SBSS-1) (first of SBSS planned constellation, follow-on of theMSX)	U.S. Air Force	1031	SSO, 630 km	Gimbaled telescope, 30-cm aperture, 2×4 deg	[28], [29]
2013	Sapphire	Canadian Department of National Defence	28.5	Dawn-dusk SSO 771 km × 786 km	15-cm telescope, 1.4×1.4 deg	[30]
2013	Near-Earth Orbit Surveillance Satellite (NEOSSat)	Canadian Department of National Defence	72	785 km, 98° inclination	15-cm aperture telescope, FoV: 0.85×0.85 deg	[31]
2014	Geosynchronous Space Situational Awareness Program (GSSAP) (constellation – 8 satellites)	U.S. Air Force, then U.S. Space Force	-	Near-GEO	Electro-optical and infrared	[32], [33]
2017	Operationally Responsive Space (ORS)-5 SensorSat (follow-on of SBSS-1)	U.S. Space Force	~140	600 km, equatorial	Electro-optical	[34]
2024	Skylark constellation (12 satellites, 4 launched already)	NorthStar Earth & Space	16-U Cubesat equivalent	SSO, 530 km	Electro-optical	[35], [36]
End of 2024 (planned)	Flamingo constellation (12 satellites)	Vyoma Space	60	LEO	Electro-optical	[37], [38]
2027 (planned)	Redwing and Little Innovator in Space Situational Awareness (LISSA)	Canada's Department of National Defence (DND)	-	SSO, 575 km	Short-wave infrared (SWIR) camera	[39]

The 19th also injest predictive ephemeris volontarily shared by satellite owner/operators (O/Os) about their assets, which may include important planned maneuvers for the screenings that cannot be captured by internal solutions. Three main kind of screening are performed: HAC vs. HAC, O/O ephemeris vs. HAC, and O/O ephemeris vs. O/O ephemeris. For identified High Interest Events (HIEs), risk assessment is conducted to determine the probability that the objects collide at the estimated TCA [40].

The resulting products are freely available to governments, commercial operators, and spacefaring entities worldwide through the U.S. "SSA Sharing Program," an initiative by the U.S. Department of Defense (DoD)[3], aimed at improving the global safety and sustainability of space operations. All shared information is provided via the space-track.org platform [41] and is categorized into basic and advanced levels. The basic level is accessible to any operator who applies and includes warnings about potential collisions, delivered in the form of Conjunction Data Messages (CDMs), allowing operators to maneuver their satellites to avoid crashes. By signing an "SSA Sharing Agreement," operators can access additional advanced products, such as SP ephemeris for all unclassified RSOs [40]. However, this agreement requires greater cooperation and data sharing from the operator.

Many countries and national agencies rely exclusively on information from the 18th SDS, while others have developed their own systems that add value or replicate the capabilities offered by the 18th SDS [13]. Although the fundamental pipeline behind SSA data processing is generally similar, these other SSA systems may employ distinct catalogs, software tools, and customized approaches. For example, several companies are exploring or have already incorporated Machine Learning (ML) techniques for improving automation and accuracy of SSA products [42].

In Europe, the European Union (EU) now offers comprehensive, no-cost space safety services to spacecraft operators worldwide, similar to those provided by the U.S. Launched in January 2023, these services mainly rely on observational data generated by the EU SST and can be categorized into collision avoidance, re-entry analysis, and fragmentation analysis, [3, 13]. EU SST capabilities that are not provided by the 18th SDS include accounting for variability in collision probability by applying a range of scaling factors to the size and covariance of space objects, which is a more robust method than the traditional one [3].

At ESA, CDMs issued by the U.S. are used as a foundation, alongside internal ephemeris and databases such as DISCOS (Database and Information System Characterising Objects in Space) [42], which is the most comprehensive repository for launch data, object registration, vehicle specifications, and spacecraft details—

[3] The overall program falls under the responsibility of U.S. Space Command (USSPACECOM), while its subordinate unit, the Combined Force Space Component Command (CFSCC), oversees management. However, the day-to-day tasks of sharing SSA have been delegated to the 18th SDS.

such as size, mass, shape, and mission objectives—covering over 40,000 objects [13]. Although ESA is not involved in the EU SST, it occasionally relies on its services for additional support, such as for the assisted re-entry of the satellite Aeolus into the atmosphere [43].

At NASA, conjunction risk analyses for unmanned assets are managed by the CARA (Conjunction Assessment Risk Analysis) team, which benefits from a close collaboration with the 18th SDS. Rather than relying solely on 18th SDS standard services, the CARA team utilizes 18th SDS resources—such as SSN observations and the Astrodynamics Support Workstation (ASW) capabilities—to conduct their own independent analyses [44]. Moreover, CARA largely employs offline manual tools for in-depth evaluations of HIEs and further investigation of other incidents. This enables NASA to manage higher-risk encounters with greater precision compared to using the standard 18th SDS services alone.

Further details about the analytical methods and tools used by other agencies and nations for SSA data processing can be found in [45].

In this framework, a significant recent trend has seen a private sector involvement – particularly in the U.S. and Europe – through the emergence of specialized commercial providers for each critical component of the SSA data processing pipeline [8]. Companies like COMSPOC Corp., LeoLabs, Slingshot Aerospace, NeuraSpace and Look Up Space, now offer SSA data, tailored analytics products, or even their in-house software, often packaging them as subscription-based services. This modular approach makes it easier for clients to access SSA capabilities without the heavy infrastructure investment previously required, marking a shift from the traditional model.

For instance, USSPACECOM has recently sought to enhance its existing network by integrating data from both international and commercial sources [46]. Similarly, NASA [46] and ESA [42] have either already incorporated or are planning to integrate data from commercial providers into their systems, though they enforce stringent standards to ensure compliance However, outsourcing some SSA functions may not be compatible with security interests of some nations, which do not want to fully depend on private providers for sensitive operations. To maintain control over data and processes, a hybrid model is emerging where private companies supply software and tools while governments retain in-house control of data processing [8]. This primarily applies to processed data, as raw data—especially from RADAR and laser systems—remains strictly guarded by national military entities

2.1.3 Mitigation

Mitigation involves several critical decisions, including when, how, and on what criteria the maneuvers are executed. Individual operators are primarily responsible for these decisions, using analytical data products like CDMs to inform their choices.

However, certain organizations, such as the EU SST, offer support to subscribing operators by providing visual tools that highlight optimal maneuver timing, intensity, and in some cases, duration, to effectively reduce the risk of conjunction. [47].

Operators around the world utilize different Go/No-Go metrics to decide whether a maneuver is necessary. These metrics may include factors like miss distance at the TCA, radial separation, and Probability of Collision (P_C). P_C-based metrics are by far the most popular because they integrate miss distance, object size, and positional uncertainty in a mathematically rigorous way. Many space agencies and operators have established tailored thresholds for P_C to trigger maneuvers. For example, both NASA and ESA typically execute maneuvers for unmanned spacecraft when the P_C exceeds 10^{-4}, which is found as a good a balance between avoiding unnecessary maneuvers and mitigating the risk of collision. The Japan Aerospace Exploration Agency (JAXA) categorizes collision risk into three levels based on the P_C and TCA: monitor (level 1), urgent (level 2), and critical (level 3). For example, level 1 involves early monitoring five days before TCA when the P_C exceeds 10^{-5}, while level 2 requires preparation and possible maneuver implementation if the Pc is higher than 10^{-4} [48].

Interestingly, using of the P_C for maneuver decisions originated with the International Space Station (ISS). Prior to this, Space Shuttle missions used a "shoebox" approach, where any object entering a predefined volume triggered a maneuver [49]. However, this method proved unsustainable for the ISS due to the high number of false positives and the impractical frequency of maneuvers, leading NASA to adopt a more suitable P_C-based approach.

As surveyed by the Space Data Association (SDA), Go/No-Go criteria are slightly different for commercial operators due to operational constraints like limited fuel budgets and the availability of sensor data [50]. Operators may set thresholds based on miss distance or collision probability but are also constrained by mission-specific factors like available fuel and spacecraft configuration. For instance, Starlink adopts a conservative P_C threshold of 10^{-5}, which, while ensuring greater safety, results in a high frequency of maneuvers [51]. Some operators employ metrics that rely on simplifying assumptions, which do not reflect the complexities of actual spacecraft encounters. Decisions based on miss distance alone, while easier to implement, can offer a misleading sense of safety, as they may not capture the true risk of collision. Nevertheless, even when using P_C-based criteria, without accurate positional data and robust data fusion, the metric often falls short of providing reliable, decision-quality information [50].

Regarding the timing of CAMs, operators must balance the size of the mitigation maneuver with the timing of its execution. Smaller maneuvers can be employed if executed further in advance of the TCA. Waiting until closer to the TCA often requires a larger maneuver to achieve the same level of risk reduction. However,

this delay allows for the benefit of additional tracking data that could refine the understanding of the collision probability, potentially lowering it to a point where a maneuver becomes unnecessary. Therefore, the decision is a matter of trading-off risk, fuel consumption, and operational impact [46]. For NASA assets, maneuvers are planned whenever the P_C exceeds 10^{-7} two days before TCA [52] and operators are mandated to submit proposed maneuver plans at least 24 hours before the intended execution. This allows the CARA team enough time to screen the proposed maneuver against other objects to check for potential conflicts [53]. The final Go/No-Go decision point occurs approximately 12 hours before TCA if the conjunction exhibits a P_C above 10^{-4} [52]. Similarly, ESA makes the final maneuver decision when the Pc is still above 10^{-4} less than 24 hours before TCA [54], but it reserves time to cancel or refine the maneuver if additional ground station accesses are available before TCA to send updated commands. At JAXA, the final decision meeting for executing a CAM is set close to the TCA, allowing decision-makers to use the most accurate and up-to-date information about the conjunction before deciding whether to proceed with the maneuver [48]. This final decision point depends on factors such as the time required for preparation (e.g., planning, securing communication links) and the availability of ground stations. The maneuver itself is executed soon after this meeting to ensure that there is enough time to implement the maneuver successfully.

Timings appear to be more conservatives for commercial operators, as found in [50]. Specifically, they often prefer to execute CAMs three days before the TCA, particularly in LEO, as this allows them to avoid last-minute complications, such as ground station availability or uncertainties in the orbital data.

Concerning the kind of CAMs, while this is not the focus of this thesis, the fundamentals are presented in a simplified manner to provide completeness to the description of the avoidance process. CAMs can generally be classified into different types based on the direction of the thrust applied: intrack, radial, and cross-track. Intrack maneuvers, where thrust is applied along the spacecraft's velocity vector, are the most fuel-efficient and commonly used because they alter the spacecraft's orbital period, thereby directly shifting its position at the TCA [49]. However, radial maneuvers (along the orbit's radius) and cross-track maneuvers (perpendicular to the orbit plane) may sometimes be preferred in certain conjunction geometries or due to the mission's operational constraints, such as maintaining the required geometry in satellite constellations in LEO. These maneuvers can provide a greater reduction in collision probability, though they are less efficient in terms of fuel consumption. In some cases, a combination of these maneuver types is used to balance collision probability reduction and fuel use. A second corrective maneuver is generally needed to restore the spacecraft's nominal orbit after a collision threat has passed. At NASA, which pursues mitigation if the P_C exceeds 10^{-4}, the maneuver is designed to reduce the P_C by at least 1.5 orders of magnitude, briging it down to around 3.2×10^{-6} [46].

2.2 Operational concept of the proposed system

The autonomous collision avoidance system proposed in this thesis is schematically illustrated in Fig. 2.5. In the context of the following discussion, the term "primary" refers to the satellite hosting the system, while "secondary" refers to the object involved in a potential conjunction with the primary.

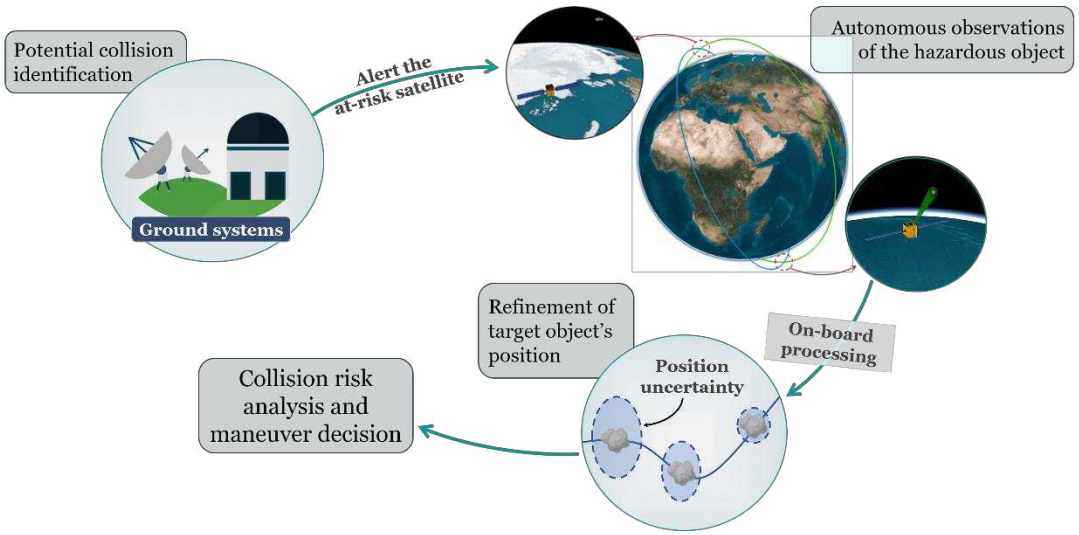

Fig. 2.5 Proposed autonomous collision avoidance approach

The proposed on-board system is designed to execute a series of sequential actions triggered whenever an upcoming conjunction involving the primary spacecraft is identified by ground-based systems. The timing of the first conjunction identification may vary depending on the specific service the spacecraft O/O uses for orbital safety information. For instance, the 18th SDS makes predictions up to 7 days in advance for satellites in LEO, and up to 10 days for those beyond LEO [40].

Following the initial identification, orbital data on the secondary object is transmitted to the primary. This data is needed by the primary for three tasks: 1) determining optimal time windows for conducting observations, 2) calculating at each time window a restricted region of space where the secondary object is expected to be visible during its approach, and 3) refining the secondary's estimated trajectory as new in-orbit measurements are acquired.

Concerning the type of uplinked orbital data about the secondary, ephemeris including predicted positions and velocities at several future times may be sufficient for the first two tasks. However, the third task entails performing OD, which requires an estimate of the secondary's orbital state, a covariance matrix, and details about the force model to be used. While the orbital state could be interpolated from ephemeris at any desired epoch, the other two elements must be provided from the ground to effectively refine the orbital solution. Estimating the covariance matrix through OD is necessary since the calculation of the collision probability relies on it.

Another important element for the three tasks mentioned above is that the primary

has self-position awareness, which can be easily achieved with a GNSS receiver. If such a device is onboard, as is common with modern satellites, the primary satellite can use its onboard processing capabilities to propagate its own state forward in time. Unless ephemeris are uplinked for the secondary, the primary also propagates the secondary's state forward. Once predictive trajectories are available for both objects, they are screened against each other to determine the first available observation opportunity. This operation is repeated by the primary for each subsequent opportunity, always using the most updated data available about the secondary, which is refreshed each time new information is received from the ground or after newly acquired space-based measurements.

There are various criteria that can be used to calculate time windows of the observation opportunities. One option is to determine when the relative distance between the objects falls below a certain threshold, decided according to the detection capabilities of the onboard sensor. For instance, if the primary satellite is equipped with a Sodern AURICAM camera, 1-meter objects would become visible at approximately 800 km of distance [55]. The specific method for identifying observation opportunities will be developed and discussed in Chapter 4, drawing from insights into suitable sensor technologies explored in the following sections.

Before each planned observation, the satellite must calculate the trajectory of the secondary object and orient the sensor's Field of View (FoV) accordingly to maximize the chance of a successful observation. Depending on the approach geometry, it may be more efficient in terms of attitude control to observe the object as it moves away, rather than as it approaches.

The data collected during these observations is then processed onboard to refine the current knowledge of the secondary object's orbit. This is done using a sequential filtering orbit determination process, which updates the object's orbital state in real-time with each new observation.

It should be noted that, in parallel to this onboard process, the secondary object will continue to be tracked by traditional ground-based SSA, and its orbit will be independently refined from the ground. The resulting orbital solutions must be regularly uplinked to the primary satellite during its scheduled ground-station accesses. One reason for this is that space-based observation attempts may sometimes fail, due to factors like the object being in an unexpected position or too dim to be detected by the onboard instruments. In cases where the primary satellite fails to gather observational data, relying solely on the orbital estimate uplinked at the time of the initial conjunction detection would be insufficient for making an autonomous maneuver decision. That initial data could be several days old, and uncertainties in the secondary's position at TCA increase the older the data is. Moreover, combining the latest ground-based orbital data with the onboard observations is what ensures that the orbital solution available onboard is always at least as accurate, if not more accurate, than the ground-based solution, ultimately leading to improvements over the current process.

At a certain point, the entire process of data collection, orbit refinement, and collision risk assessment is entirely moved to the space segment. The exact timing for this transition can be determined in various ways, depending on the operator's needs

and preferences. One option is to let the satellite autonomously handle the process only after the last ground-station access before TCA, or after one of the last ones. Another option is to set a fixed time before the TCA (for example, 1-2 days). In this regard, as noted in Section 2.1.3, many commercial operators make the final maneuver decision more than 3 days before the event. Therefore, by letting the satellite improve the final decision during the remaining 3 days, the likelihood of reducing false alarms is significantly increased.

Finally, the Go/No-Go decision is made by the primary after the last feasible observation opportunity, ideally in the very last orbits before TCA, waiting as long as possible to attempt getting a better orbit estimate. This aspect will be discussed more in detail later in the thesis.

As for the maneuver design—which includes determining its magnitude, direction, timing, and duration—it depends significantly on the type of propulsion system available onboard. Extensive literature exists on autonomous CAM optimization differentiated by propulsion type, but this aspect will not be addressed in detail here. Nevertheless, regardless of the propulsion system, a good approach is to pre-optimize standard CAM sequences and store them onboard, allowing the satellite limited degrees of freedom to further optimize in each instance, resulting in a fast and resource-efficient design [56].

2.2.1 Applicability in GEO

The proposed system is designed for satellites in LEO, as this is the most congested orbital region and prone to collisions. However, while not as densely populated as LEO, the GEO belt is also heavily trafficked and subject to actual collision risk. Therefore, it is natural to consider the applicability of the proposed system for satellites orbiting in GEO as well.

One notable difference between GEO and LEO satellites is that the former, due to their geostationary position over the Earth's surface, typically maintain continuous access to ground stations. As a result, the system would not offer a significant advantage in terms of reducing the gap between the last orbit determination and maneuver execution, as it is much easier to update maneuver commands for GEO satellites based on newly available observational data.

Nevertheless, one benefit of implementing this system in GEO lies in the additional space-based observations, which would enhance the accuracy of the positional data for secondary objects. GEO satellites are more distant and harder to track from Earth than LEO satellites, leading to generally higher uncertainties in their positional data. Incorporating onboard observations could substantially improve orbit determination for secondary objects, which is an area worth further investigation.

Extending the system to GEO satellites, however, introduces different orbital dynamics. Unlike in LEO, where objects frequently encounter each other, GEO satellites move in nearly coplanar orbits and drift along the belt at similar speeds, which changes the nature of collision risks. Collisions in GEO tend to arise from objects changing inclination due to perturbations or nominally inclined orbits, with objects approaching from above or below. The slower relative velocities in GEO are favorable for making observations, but the system would need to be adapted to

account for these dynamics.

Another challenge in GEO arises if the primary satellite aims to track unknown objects, which requires performing Initial Orbit Determination (IOD)[4]. In this case, an observability problem related to the nature of angles-only observations arises due to the observer being in the same plane or a similar one of the target [57]. However, this issue does not apply if the system sticks to observing targets for which prior trajectory information is provided from ground-based systems.

Overall, while additional analysis is required to fully determine the feasibility of extending the system to GEO satellites, the basic principle of using onboard sensors for target observation is sound, and with proper adaptations, it is likely that the system could be successfully extended to GEO operations.

2.2.2 Degree of innovation

The innovative aspect of the proposed system lies in the use of onboard sensors for the self-defense of the host satellite. Currently, the only existing example of autonomous collision avoidance system is found aboard SpaceX's Starlink satellites. However, as the primary goal of this system is to minimize human intervention in the process, it limits to autonomously processing data received from Earth (i.e., CDMs), without contributing to data collection for tracking [58]. Recently, several entities have been working to develop solutions similar to SpaceX's. The Italian Space Agency (ASI) is working on the "e.Cube" project [59], aiming to demonstrate autonomous capabilities for collision analysis and maneuver planning in orbit. On a European scale, ESA's CREAM [56] initiative seeks to develop technologies for automating collision avoidance processes using artificial intelligence aboard satellites. As with SpaceX's system, these initiatives also do not integrate tracking data with observations made in orbit.

Secondly, while significant experience has already been gained in using onboard optical sensors to detect orbiting objects (see Table 1), this has never been purposed for satellite self-defense. Several international initiatives are promoting the launch of optical payloads for detecting various types of space objects, but their focus remains on expanding Earth-based catalogs through complementary in-orbit observations.

2.3 Non-technical aspects of the system

Although technical aspects are crucial in the development of any new engineering system, non-technical factors must also be considered to ensure the solution moves beyond just a concept on paper and is implemented in orbit by operators. For example, a system that proves technically feasible but incompatible with the regulatory framework would not be viable for deployment, nor would it be commercially attractive to operators. This section briefly addresses some non-technical concerns about the system's viability, including market competitiveness and compatibility with emerging regulations.

[4] Initial Orbit Determination (IOD) refers to the process of estimating the orbit of an object when no prior information about its trajectory is available.

2.3.1 Competitiveness with alternative developments

It is important to consider the competitiveness and compatibility of the proposed solution with those being developed by larger players, which are inevitably set to drive global trends. Various methods have been proposed worldwide to minimize the time between the decision to maneuver and the TCA. For instance, ESA is currently exploring options such as [60], [61]:

- Using inter-satellite links to improve timely communication with satellites, enhancing responsiveness even close to the TCA,
- Increasing the number of ground stations to provide broader, more frequent coverage,
- Delegating part of the collision analysis to the satellites themselves, allowing them to process trajectory updates directly. This would enable satellites to handle updates near the TCA without waiting for ground-based processing, optimizing response times and minimizing human intervention.

These solutions are not incompatible with the proposed system; rather, they could be integrated synergistically to maximize overall effectiveness. In fact, the above methods rely on data collected from conventional ground-based surveillance systems, whereas the considered system introduces an additional layer of data collected from space, enhancing the overall quality of orbital predictions. It is worth noting that the benefit also stems from the fact that the timeliest data on hazardous objects can only be collected by the at-risk platform itself, which is why the considered solution adds value to any other solutions.

In fact, in ground-based systems, even assuming uninterrupted communication link with the at-risk satellite, there is a chain of events that must occur—from raw observations to maneuver decisions—involving multiple layers of communication, human intervention, and dependence on network infrastructure, all of which introduce potential delays. By contrast, the at-risk satellite can independently observe, assess, and make maneuver decisions without the need for external communication or human input, thus bypassing ground delays and enabling real-time response.

In any case, even if there were a negligible time difference between ground-based and space-based processes, the additional data gathered from space would still provide unique information. The benefits of integrating diverse data sources ("data fusion") are well-documented in the literature [17], [50], [62].

The proposed system is also sustainable, as it requires only software updates to utilize existing onboard hardware, avoiding the need for more resource-intensive options that involve expanding ground infrastructure or deploying additional satellite networks for real-time communication.

Moreover, the autonomous nature of the proposed system aligns with the trend toward increasing onboard automation, a direction in which both the research community and ESA are significantly investing. This level of automation is especially advantageous for large constellations typical of the New Space era, where space-based data on a same hazardous object could be collected from multiple satellites and shared among the constellation, improving the accuracy of collision assessments.

Therefore, regardless of future changes in the national and international context of this sector, the proposed solution is set to integrate harmoniously with other emerging technologies and remains competitive due to its unique advantages.

2.3.2 Conflicts in active satellite conjunctions and compatibility with emerging regulations

A common concern when a potential conjunction between two operational satellites is anticipated is, 'Who should maneuver?' This dilemma becomes even more complicated when one of the satellites has autonomous capabilities, as it may make a decision without communicating it externally, leaving other satellite's operator uncertain about how to respond. This lack of coordination can lead to conflicting actions such as both satellites maneuvering, potentially increasing the collision risk, or neither satellite taking action, which is equally dangerous. The situation is even more uncertain if both satellites are equipped with autonomous systems, compounding the potential for misaligned actions.

From a regulatory standpoint, there are currently no formal rules dictating who should maneuver in such events, leaving the decision to be handled through informal email exchanges between operators. The current governance framework is largely based on non-binding guidelines, such as international agreements and technical standards that aim to reduce the creation of space debris. However, compliance with these guidelines is limited, and there is a growing consensus that more stringent, binding international rules are needed.

In recent years, this lack of clear rules has led to incidents in conjunction scenarios. A notable case occurred in September 2019, when ESA's Aeolus satellite faced a potential collision with SpaceX's Starlink 44. Despite being notified, SpaceX did not take action, and ESA was ultimately forced to perform a CAM [63]. Another similar case involved OneWeb-0178 and Starlink-1546, where disagreements over responsibility escalated into a diplomatic issue, with both parties accusing the other of false claims and inaccurate statements [64]. As the number of satellites in orbit continues to grow, incidents like these will become more frequent.

This has prompted many entities to advocate for universal guidelines that would clarify the obligations of spacecraft operators. As a result, efforts are underway to establish global norms that promote international collaboration and standardization in STM practices. A prominent example in Europe is the Horizon 2020 "SPACEWAYS" project [65], which is evaluating legal, policy, and regulatory frameworks to develop a unified European approach to STM. Among other things, the project is examining how European regulations might need to adapt to the STM practices of other major space actors like the U.S. and China.

These developing frameworks must be taken into account when designing an autonomous system, as the very nature of autonomy limits the potential for cooperation.

The system in this thesis operates on the idea that, despite the presence of onboard autonomous systems, the decision on which satellite should maneuver in the event of a satellite-satellite conjunction must be made on the ground and communicated to both satellites prior TCA. The satellite authorized to maneuver will either follow

the transmitted command or, if equipped with an autonomous system, independently determine whether a maneuver is necessary. Conversely, the satellite instructed to maintain its path will either take no action or disable its autonomous system, if one is present. Making the decision on the ground is essential, as a satellite cannot determine whether the other object will maneuver without receiving that information from ground control. If ground coordination fails for any reason, the satellite equipped with an autonomous system should assume that the other asset will not maneuver and act accordingly, which is safer than trusting that the other satellite will resolve the situation.

In this direction, international efforts should be directed at ensuring that operator's cordination, which currently relies on outdated email exchanges, is regularly and rapidly achieved each time. This can be done by developing suitable protocols, online platforms, and standards to facilitate and expedite the coordination process.

However, it is important to keep in mind that several factors limit the extent of cooperation that can realistically be accomplished. Achieving consensus among different nations is difficult, and even if agreements are reached, not all countries will comply. Nations like North Korea, which recently launched its first spy satellite into LEO [66], are unlikely to adhere to international norms.

Therefore, while cooperation must be prioritized as the first line of action in managing conflicting STM situations, equipping satellites with independent risk mitigation mechanisms alleviates the dependence on potentially unstable international agreements, which may falter due to potential political uncertainties, as demonstrated by the complexities that have emerged in the cooperation between ESA and the Russian agency Roscosmos for the ExoMars mission.

Overall, achieving a balance between autonomous systems and international cooperation will be key for the realistic future of STM.

References

[1] M. A. Skinner, D. Oltrogge, M. Strah, R. J. Rovetto, A. Lacroix, A. K. Anil Kumar, K. Grattan, L. Francillout, I. Alonso, "Space traffic management terminology," *Journal of Space Safety Engineering*, vol. 9, no. 4, 2022, pp. 644-648, doi: https://doi.org/10.1016/j.jsse.2022.09.001

[2] D. L. Oltrogge, S. Alfano, D. Berry, J. Cooper, D. A. Vallado, E. Kulu, "Contrasting the inflection points and efforts in space traffic coordination and management," in *10th Annual Space Traffic Management Conference*, Austin, TX, USA, 2024

[3] EU SST, "European Union Space Surveillance and Tracking," Accessed Oct 6, 2024. [Online]. Available: https://www.eusst.eu/

[4] J. Sharma, C. von Braun, E. M. Gaposchkin, "Space-based visible data reduction," *Journal of Guidance, Control, and Dynamics*, vol. 23, no. 1, 2000 pp. 170-174, doi: https://doi.org/10.2514/2.4507

[5] A. Bloom, J. Wysack, J. D. Griesbach, A. Lawitzke, "Space and ground-based SDA sensor performance comparisons," in *Advanced Maui Optical and Space Surveillance Technologies Conference (AMOS)*, Maui, Hawaii, 2022

[6] SpaceNews, “Numerica upgrades telescope network to track objects in LEO,” Accessed Oct 6, 2024. [Online]. Available: https://spacenews.com/numerica-upgrades-telescope-network-to-track-objects-in-leo/

[7] Slingshot Aerospace, “Ground-based space object tracking,” Accessed Oct 6, 2024. [Online]. Available: https://www.slingshot.space/solutions/capabilities#ground-based-space-object-tracking

[8] B. Lal, A. Balakrishnan, B. M. Caldwell, R. S. Buenconsejo, S. A. Carioscia, “Global trends in Space Situational Awareness (SSA) and Space Traffic Management (STM),” IDA Science and Technology Policy Institute, Washington, DC, USA, Tech. Rep. GEN-DB-LOG-00288-OPS-SD, v.7, 2023

[9] M. Losacco, P. Di Lizia, M. Massari, A. Mattana, F. Perini, M. Schiaffino, C. Bortolotti, M. Roma, G. Naldi, G. Pupillo, G. Bianchi, L. Lama, D. Cutajar, A. Magro, C. Portelli, M. Reali, W. Villadei, “The multibeam radar sensor BIRALES: performance assessment for space surveillance and tracking,” in *69th International Astronautical Congress*, Bremen, Germany, 2018

[10] NASA, “State-of-the-art small spacecraft technology,” NASA Ames Research Center, Moffett Field, CA, USA, Tech. Rep. NASA/TP—2024–0001462, 2024

[11] S. Henault, “Orbit estimation using passive radio frequency observations,” Defence Research and Development Canada – Ottawa Research Center, Ottawa, Canada, Tech. Rep. DRDC-RDDC-2021-R102, 2021

[12] M. Prechtel, “Passive RF sensing in support of SSA,” in *Advanced Maui Optical and Space Surveillance Technologies Conference (AMOS)*, Wailea, Maui, Hawaii, USA 2018

[13] D. L. Oltrogge, S. Alfano, D. Berry, J. Cooper, D. A. Vallado, E. Kulu, “Contrasting the inflection points and efforts in space traffic coordination and management,” in *10th Annual Space Traffic Management Conference*, Austin, TX, USA, 2024

[14] Kratos Defense and Security Solutions, “Towards complete space domain awareness,” Accessed Oct 8, 2024. [Online]. Available: https://www.kratosdefense.com/-/media/k/pdf/s/si/kratos-rf-space-situational-awareness.pdf

[15] ESA, "The IZN-1 laser ranging station in Tenerife is the first of its kind," Accessed Oct 9. [Online]. Available: https://www.esa.int/Space_Safety/Space_Debris/New_laser_station_lights_the_way_to_debris_reduction

[16] H. Virdeea, P. Bartram, E. Schafer, D. Gooding, J. Luis, "A new global laser ranging network for satellite and debris tracking," in *73rd International Astronautical Congress (IAC)*, Paris, France, 2022.

[17] E. Cordelli, A. Vananti, T. Schildknecht, "Analysis of laser ranges and angular measurements data fusion for space debris orbit determination", *Advances in Space Research*, vol. 65, no. 1, 2020, pp. 419-434, doi:

https://doi.org/10.1016/j.asr.2019.11.009

[18] C. Bamann, U. Hugentobler, "Accurate orbit determination of space debris with laser tracking," in *7th European Conference on Space Debris*, Darmstadt, Germany, 2017

[19] J. Rodriguez-Villamizara, T. Schildknechta, "Laser ranging to space debris: overcoming Challenges," in *74th International Astronautical Congress (IAC)*, Baku, Azerbaijan, 2023

[20] D. Cerutti-Maori, J. Rosebrock, L. Leushacke, H. Krag, "Preliminary concept of a space-based radar for detecting mm-size space debris," in *7th European Conference on Space Debris*, Darmstadt, Germany, 2017

[21] R. Ahmed, N. Majurec, J.W. De Bleser, "A Cubesat-based radar for characterization of millimetric orbital debris," in *The First International Orbital Debris Conference (IOC)*, Sugar Land, TX, USA, Dec. 9–12, 2019

[22] P. Zimmer, "Space-based optical detection of mm-scale space debris," Presented at *SINTRA (Space debris Identification and Tracking) Proposers' Day*, Virtual, Aug 10, 2022. Accessed Oct 16, 2024. [Online]. Available: https://www.iarpa.gov/images/PropsersDayPDFs/SINTRA/Lightning/20_Zimmer_LightningTalk_-_Space-based_optical_-_Zimmer.pdf

[23] C. von Braun, J. Sharma, E.M. Gaposchkin, "Space-Based Visible metric accuracy," Journal of Guidance, Control and Dynamics, vol. 23, no. 1, 2000, pp. 175-181, doi: https://doi.org/10.1016/10.2514/2.4508

[24] D.C. Harrison, J.C. Chow, "The Space-Based Visible sensor," *Johns Hopkins APL Technical Digest*, vol. 17, no. 2, 1996, pp. 226-236

[25] R.L. Scott, B. Wallace, D. Bedard, "Space-based observations of satellites from the MOST microsatellite," Defence R&D Canada, Ottawa, Canada, Tech. Rep. TM 2006-199, 2006

[26] Missile Defense Advocacy Alliance, "Space Tracking and Surveillance System (STSS)," Accessed Oct 11, 2024. [Online]. Available: https://missiledefenseadvocacy.org/defense-systems/space-tracking-and-surveillance-system/

[27] Gunter's Space Page, "STSS 1, 2," Accessed Oct 11, 2024. [Online]. Available: https://space.skyrocket.de/doc_sdat/stss-1.htm

[28] U.S.S.F., "Space Based Space Surveillance," Accessed Oct 11, 2024. [Online]. Available: https://www.spaceforce.mil/About-Us/Fact-Sheets/Article/2197743/space-based-space-surveillance/

[29] eoPortal, "SBSS (Space-Based Surveillance System)," Accessed Oct 11, 2024. [Online]. Available: https://www.eoportal.org/satellite-missions/sbss

[30] A. Scott, J. Hackett, K. Man, "On-orbit results for Canada's Sapphire optical payload," in *Advanced Maui Optical and Space Surveillance Technologies (AMOS) Conference*, Maui, Hawai'i, USA, 2013

[31] R. L. Scott, S. Thorsteinson, V. Abbasi, "On-orbit observations of conjuncting space objects prior to the time of closest approach," *Journal of Astronautical Sciences*, vol. 67, no. 4, 2020, pp. 1735–1754, doi: https://doi.org/10.1007/s40295-

020-00236-x

[32] Gunter's Space Page, “GSSAP 1, 2, 3, 4, 5, 6, 7, 8 (Hornet 1, 2, 3, 4, 5, 6, 7, 8),” Accessed Oct 11, 2024. [Online]. Available: https://space.skyrocket.de/doc_sdat/gssap-1.htm

[33] Air and Space Forces Magazine, "GSSAP," Accessed Oct 11, 2024. [Online]. Available: https://www.airandspaceforces.com/weapons-platforms/gssap/

[34] eoPortal, "ORS-5 (Operationally Responsive Space-5)," Accessed Oct 11, 2024. [Online]. Available: https://www.eoportal.org/satellite-missions/ors-5#ors-5-operationally-responsive-space-5--sensorsat

[35] Gunter’s Space Page, “Skylark 1, ..., 12,” Accessed Oct 11, 2024. [Online]. Available: https://space.skyrocket.de/doc_sdat/skylark-1.htm

[36] Space News, "Electron launches NorthStar satellites in latest recovery test," Accessed Oct 11, 2024. [Online]. Available: https://spacenews.com/electron-launches-northstar-satellites-in-latest-recovery-test/

[37] NewSpace Index, "Vyoma Space (Flamingo)," Accessed Oct 11, 2024. [Online]. Available: https://www.newspace.im/constellations/vyoma-space

[38] Space News, "Aerospacelab to build debris-tracking satellite for Vyoma," Accessed Oct 11, 2024. [Online]. Available: https://spacenews.com/aerospacelab-to-build-debris-tracking-satellite-for-vyoma/

[39] Orbital Today, "UK and Canada collaborate on redwing microsatellite for space domain awareness," Accessed Oct 11, 2024. [Online]. Available: https://orbitaltoday.com/2024/10/10/uk-and-canada-collaborate-on-redwing-microsatellite-for-space-domain-awareness/

[40] 18th and 19th Space Defense Squadrons, “Spaceflight safety handbook for satellite operators,” United States Space Force, Vandenberg, CA, USA, Tech. Report, vers. 1.7, 2023

[41] Space-Track. Accessed Oct 11, 2024. [Online]. Available: https://space-track.org

[42] J. Siminski, K. Merz, B. Bastida Virgili, V. Braun, S. Flegel, T. Flohrer, Q. Funke, A. Horstmann, S. Lemmens, F. Letizia, F. McLean, S. Sanvido, V. Schaus, “ESA's collision avoidance service: current status and special cases,” in *8th European Conference on Space Debris*, Darmstadt, Germany, 2021

[43] EU SST, “EU SST supports ESA on the re-entry of Aeolus,” Accessed Oct 11, 2024. [Online]. Available: https://www.eusst.eu/newsroom/eu-sst-supports-esa-reentry-aeolus/

[44] L. K. Newman, A. K. Mashiku, M. D. Hejduk, M. R. Johnson, J. D. Rosa, “NASA conjunction assessment risk analysis updated requirements architecture,” in *2019 AAS/AIAA Astrodynamics Specialist Conference*, Portland, ME, USA, 2019

[45]. F. Schiemenz, J. Utzmann, H. Kayal “Survey of the operational state of the art in conjunction analysis,” CEAS Space Journal, vol. 11, 2019, pp. 255–268, doi: https://doi.org/10.1007/s12567-019-00242-2

[46] NASA, “NASA: spacecraft conjunction assessment and collision avoidance best practices handbook”, NASA, Washington, DC, USA, Tech. Rep. NASA/SP-

20205011318, 2020

[47] COMSPOC, “Response to Request for Information on Scope of civil Space Situational Awareness services,” Accessed Oct 12, 2024. [Online]. Available: https://www.space.commerce.gov/wp-content/uploads/2023-02-27-COMSPOC.pdf

[48] Japan Aerospace Exploration Agency (JAXA), “Standard for spacecraft collision risk management,” JAXA, Tokyo, Japan, Tech. Rep. JMR-016(E), 2022

[49] J. Wolfhagen, “Collision avoidance in the New Space era,” Delft University of Technology, Delft, Netherlands, PhD thesis, 2020

[50] S. Alfano, D. L. Oltrogge, L. Arona, "Operators’ requirements for SSA services," *The Journal of the Astronautical Sciences*, vol. 69, 2022, pp. 1441–1476, doi: https://doi.org/10.1007/s40295-022-00346-8

[51] SpaceX, “SpaceX constellation status report, december 1, 2022 – May 31, 2023,” SpaceX, Washington, DC, USA, Tech. Rep., 2023

[52] A.K. Mashiku, “NASA conjunction assessment risk analysis (CARA): CARA process overview, large constellations and light pollution,” Advisory group meetings - Astronomy and Astrophysics Advisory Committee (AAAC), Virtual, Jan. 2024. Accessed Oct 13, 2024. [Online]. Available: https://www.nsf.gov/attachments/308703/public/8_CARA_Overview_Alinda_Mashiku.pdf

[53] NASA’s Office of the Chief Engineer, “Collision avoidance for space environment protection,” NASA, Washington, DC, USA, Tech. Rep. NID 7120.132, 2021

[54] F. Letizia, "ESA operational collision avoidance," UNOOSA –Promoting Space Sustainability, Virtual, Feb. 2021. Accessed Oct 13, 2024. [Online]. Available: https://www.unoosa.org/documents/pdf/PromotingSpaceSustainability/PresentationsCaseStudies/2_SpaceAgencyOperators/ESA_Operational_Collision_Avoidance.pdf

[55] Sodern, "AURICAM," Feb 2024, Accessed Oct 13, 2024. [Online]. Available: https://sodern.com/wp-content/uploads/2023/11/2023-10-04-AURICAM-datasheet.pdf

[56] V. B. Bastida, T. Flohrer, H. Krag, K. Merz, S. Lemmens, “CREAM — ESA's Proposal for Collision Risk Estimation and Automated Mitigation,” in *First International Orbital Debris Conference*, Houston, TX, USA, 2019

[57] D. A. Vallado, “Evaluating gooding angles-only orbit determination of space based space surveillance measurements,” in *Born Symposium*, Boulder, CO, USA, May 11-14, 2010

[58] SpaceX, “Starlink orbital space safety,” Aug 2021, Accessed: Oct 15, 2024. [Online]. Available: https://forum.nasaspaceflight.com/index.php?PHPSESSID=tu14od0adpt8lrslne9nr33tug&action=dlattach;topic=48297.0;attach=2054365;sess=0

[59] C. Colombo, M. Mirko, F. Scala, M.P. Brenna, J.L. Gonzalo, S. Antonetti, F. Di Tolle, R. Redaelli, F. Lisi, L. Marrocchi, M. Alberti, A. Francesconi, L. Olivieri, M. Tipaldi, "e.Cube mission: the environmental CubeSat," in *8th European Conference on Space Debris*, Darmstadt, Germany, 2021

[60] GMV News, No. 88, "Galileo PRS service as an essential element of resilient PNT," p.31. Accessed Oct 13, 2024. [Online]. Available: https://www.gmv.com/sites/default/files/content/file/2024/01/25/114/gmv_news_88_0.pdf

[61] K. Mertz, "Online Space Debris Training Course 2022, Lecture 11: colllision avoidance," Lecture, ESA Space Debris Office, Darmstadt, Germany, 2022

[62] D.L. Oltrogge, P. Wauthier, D.A. Vallado, S. Alfano, T.S. Kelso, "Results of comprehensive STCM data fusion experiment," in *8th European Conference on Space Debris*, Darmstadt, Germany, 2021

[63] ESA, "ESA spacecraft dodges large constellation," Accessed Oct 15, 2024. [Online]. Available: https://www.esa.int/Space_Safety/ESA_spacecraft_dodges_large_constellation

[64] Space News, "SpaceX and OneWeb spar over satellite close approach," Accessed Oct 15, 2024. [Online]. Available: https://spacenews.com/spacex-and-oneweb-spar-over-satellite-close-approach/

[65] SPACEWAYS H2020 website. Accessed Oct 15, 2024. [Online]. Available: https://spaceways-h2020.eu/

[66] Reuters, "North Korea's first spy satellite is 'alive', can manoeuvre, expert says," Accessed Oct 15, 2024. [Online]. Available: https://www.reuters.com/technology/space/north-koreas-first-spy-satellite-is-alive-can-manoeuvre-expert-says-2024-02-28/

Chapter 3

Deriving system requirements through orbital dynamics analysis

The core of the autonomous system is the onboard sensor, which is tasked with tracking distant objects—ranging from tens to possibly hundreds of kilometers away—traveling at velocities on the order of kilometers per second. Unless a satellite is already equipped with a suitable sensor, a dedicated secondary payload would be required. This may only be feasible for satellites weighing at least a few hundred kilograms, where a small additional payload would represent only a small fraction of the total mass.

Regarding sensing technology, Section 2.1.1.5 has emphasized that, among spaceborn sensors, electro-optical ones represent by far the most established technology. Their widespread use is primarily due to their relatively low SWaP (Size, Weight, and Power) requirements compared to active sensors like radars or laser-based systems. However, active technologies offer significant advantages for space-based SSA, such as their independence from external light sources. Unlike optical systems, which are limited by the need for the target to be illuminated by the Sun, the signal in active technologies is generated by the sensor itself, eliminating the reliance on external lighting conditions. Optical sensors may face non-visibility conditions whenever target objects are in Earth's shadow or are positioned between the observer satellite and the Sun. Another key advantage of active sensors is their ability to provide highly accurate measurements of the target's range and relative velocity, based on precise Time of Flight (ToF) and Doppler shift measurements. This contrasts with optical systems, which can only provide information on the target's position and velocity in the image plane of the camera [1, 2], which is perpendicular to the range direction. While optical measurements offer superior angular accuracy [3], accurate range measurements in orbit can be extremely valuable as they help reduce position uncertainty along the object's direction of motion (known as "along-track" or "in-track"), which is typically the direction with the greatest uncertainty. Additionally, processing ToF measurements can be simpler than analyzing images to extract information, thereby directly impacting onboard resource efficiency.

Despite their strengths, the challenging SWaP requirements of these systems can easily outweigh their benefits. For example, radars have often been proposed as primary payloads for debris monitoring applications, but they are not compatible with secondary payload constraints. In fact, studies on space-based radars for SSA

(e.g., [4], [5]) estimate range distances in the order of 100-200 meters, which are far too limited for tracking distant debris. Conversely, recent advancements in LiDAR (Light Detection and Ranging) miniaturization, including the integration of LiDAR systems into a single Photonic Integrated Circuit (PIC), have significantly reduced the SWaP of these systems, making them a more attractive option for secondary payload applications. In 2021, the U.S. included in its 'National Orbital Debris Research and Development Plan' the investigation of in-situ active beacons as a relevant technology for autonomous collision avoidance [6]. Past missions also highlight the potential of this technology for long-range detection, such as NASA's NEAR Laser Rangefinder (NLR) instrument aboard the Near-Earth Asteroid Rendezvous (NEAR) spacecraft, which used pulsed ToF to achieve a maximum range of 160 km with a range accuracy of 6 meters, while weighing just under 5 kg and consuming 15.1 W of power [7].

For these reasons, both electro-optical and LiDAR systems are being considered at this stage of the design.

3.1 Groundwork for requirements derivation

The main objective of the system is to acquire data on ground-identified, potentially colliding objects before the TCA and process that data to improve the trajectory knowledge of these objects. To translate this general objective into more specific sensor requirements, it is essential to understand the relationships between the technological parameters driving the performance of the sensors under consideration (i.e., electro-optical and LiDAR sensors) and the specific characteristics of the application. By connecting factors such as target size and required data accuracy to parameters like optical aperture or laser beamwidth, critical features of the detection scenario that directly impact sensor performance can be identified. This is done here by examining established performance metrics and the underlying formulas for both sensor technologies.

The Signal-to-Noise Ratio (SNR) is a universally applicable performance metric for any electronic detection system. However, the sources contributing to signal and noise vary significantly depending on the technology used, and the expressions for these sources also change depending on the specific operating modes or observation techniques. For instance, LiDAR measurements can be based on ToF, Frequency Modulated Continuous Wave (FMCW), or photon counting techniques, while optical observations can be conducted in tracking or sidereal stare modes.

After analyzing the relevant SNR expressions for these different techniques, a series of key relationships have been identified, as summarized in Table 3.1.

Starting from the identified application-specific features, each must be further quantified to detail sensor requirements.

Regarding the targets' cross-sectional area, since the targets for observation are expected to be initially identified from ground, the minimum size threshold is determined by the current capabilities of ground-based systems, which can track objects as small as 5-10 cm [8]. This size range serves as the baseline for the analysis, though larger target sizes could be considered to reduce system demands.

Table 3.1 Impact of key application-specific features on sensor parameters

Application-specific feature	Impact on LiDAR	Impact on electro-optical sensor
Relative distance to the target	Determines the required transmitted power, since the received power decreases with the fourth power of the distance, and the required beam divergence, which in turn drives the required optical aperture size. - For FMCW, determines the required modulation period for an unambiguous measurement. - For pulsed lasers, determines the energy per pulse	Primarily affects the required optical aperture and exposure time, since the received photon flux decreases with the square of the distance
Relative angular rate to the target	Affects beam steering capabilities	In tracking mode: impacts required steering, which drives ADCS capabilities In sidereal mode: determines the pixel spread, influencing exposure time, pixel dimensions, andFoV
Solar phase angle	Affects the amount of diffused sunlight reaching the sensor, influencing the SNR	Influences how much light hits the target, determining its brightness
Target cross-sectional area	Determines the amount of energy reflected from the target, influencing the received signal power.	Directly proportional to the signal from the target
Target material	Affects the reflectivity of the target, influencing the received signal power	Affects reflectivity, and therefore the target's signal strength is proportional to its material properties
Target positional uncertainty at the time of a planned observation	Impacts the area that must be scanned by the laser, i.e., its field of regard. Coupling this with available observation time determines how fast the area should be scanned	Determines the required FoV to ensure the target is in sight

Required positional uncertainty in the range direction	- For pulsed lasers, determines both the pulse repetition frequency (PRF), to avoid range ambiguity, and the required timing resolution of the system, in turn affecting the required pulse width and PRF. - For FMCW, drives the required modulation bandwidth. Also, higher accuracy demands better control over phase noise and frequency stability in the laser source	Unaffected (cannot provide measurements in the range direction)
Required positional uncertainty in angular directions	Determines the quality of the detectors' spatial resolution - For pulsed lasers, determines the beamwidth depends on the beam divergence and the precision of the scanning mechanism - For FMCW, determines the optical aperture size, which in turn affect the laser beam size	Determines the trade-off between FoV size and detector size. A larger detector and narrower FoV improve accuracy, and vice versa
Total visibility time within one observation window	This is the total time the sensor has to *detect* the target by scanning an area defined by positional uncertainty, followed by *observing* the target for the remainder of the time	Determines the amount of data that can be acquired

As for the required accuracy of the data to be collected in orbit, it must be sufficient to enhance orbit estimates to a level that significantly reduces the positional uncertainties currently used in collision risk assessments. To estimate these uncertainties, a database containing thousands of CDMs published by ESA in 2019 has been analyzed [9]. The database, known as 'Kelvins,' was made publicly available during ESA's 'Collision Avoidance Challenge' [9], a competition aimed at developing machine learning models to predict the final risk of collision based on the time history of CDMs. The database includes CDMs on approximately 15,000 unique events, making it the only large-scale, publicly available dataset on CDMs, thus providing a valuable resource for deriving statistically meaningful insights.

The dataset has been downloaded and processed on Matlab to convert it from its original csv format to useful form for information extraction. For each CDMs, 103 different features are available, such as the probability of collision and the estimated TCA. For the two objects in each CDMs, one represents an ESA satellite and labeled as 'target', while the other represents the space debris or other object that must be avoided and is labeled as 'chaser'. As ESA's satellites are likely better tracked than the chaser objects, positional uncertainties reported for them are not representing of

the uncertainties typically available on hazardous objects before a collision. Hence, out of all 103 features, the only pieces of information extracted for each CDMs are the three positional uncertainties for the chaser object (coming in the along-track, cross-track, and radial direction), and the time of issuance of the CDM.

The challenge mentions that potential CAMs are planned two days in advance of the TCA; however, realistically, the latest usable TCA for making a decision maneuver is within the last day prior to TCA, as confirmed by the common CAM decision-making timings analyzed in Section 2.1.3. Therefore, CDMs issued between 0.5 and 1.1 days before TCA are taken as representative of the positional uncertainties typically available for maneuver decisions. The results are reported in Fig. 3.1, which shows the distribution of 1-sigma positional uncertainties, and Fig. 3.2, which further highlights the distribution in terms of the radial, along-track, and cross-track components. It should be noted that the uncertainties reported in CDMs are already propagated at the TCA, meaning they precisely represent the values analysts use to calculate collision probabilities and make maneuver decisions accordingly.

Notably, over 40% of chaser objects have positional uncertainties exceeding 1 km. According to the derived statistics, achieving uncertainties within 207.2 meters at the TCA would improve accuracy in more than 80% of cases. Additionally, informal discussions with SSA data/service providers indicated that any data with accuracies below 100 meters at the time of collection would typically enhance current SSA products. For this reason, the target positional accuracy at collection time is set here to be below 100 meters.

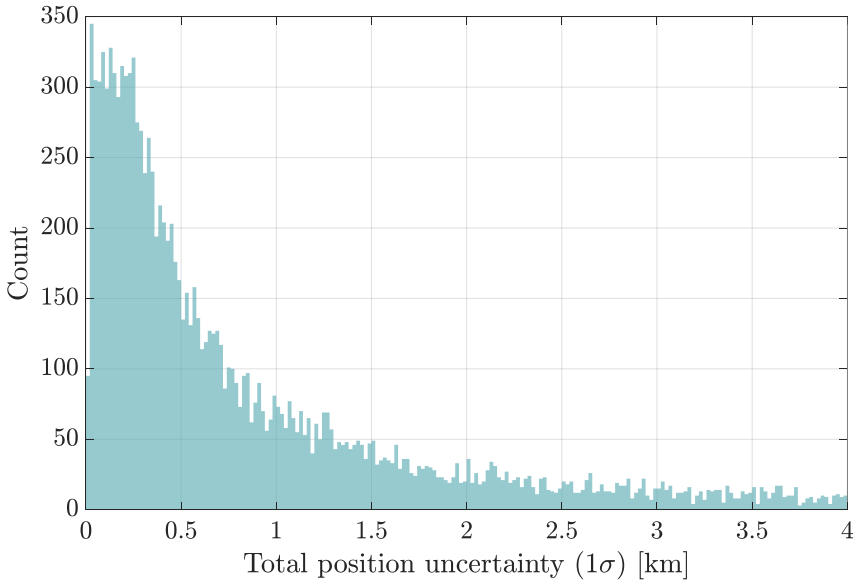

Fig. 3.1 Distribution of positional uncertainty for chaser objects included in CDMs between 0.5 and 1.1 days before TCA

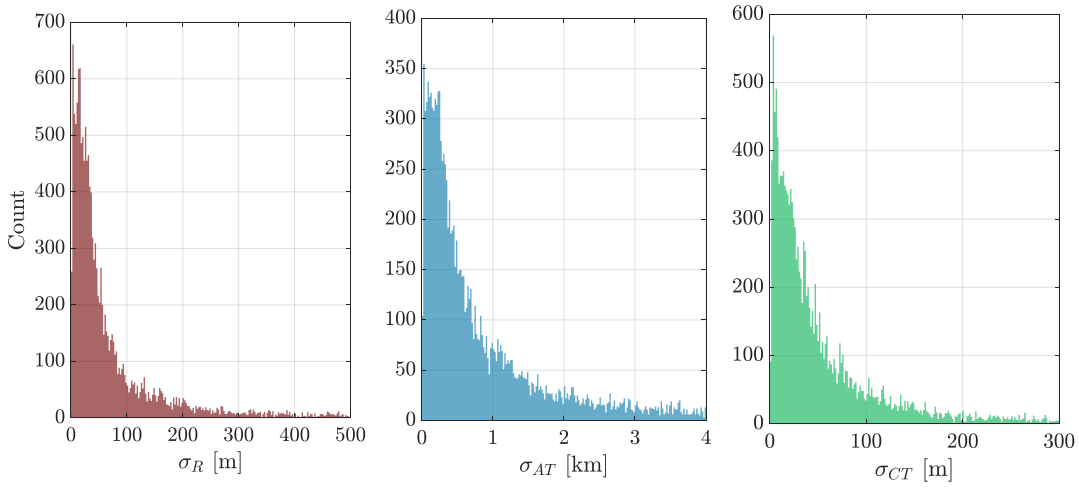

Fig. 3.2 Distributions of radial (σ_R), along-track (σ_{AT}), and cross-track (σ_{CT}) uncertainty components

It is also interesting to compare the positional uncertainties of chasers (see Fig. 3.1) with those of targets (i.e., ESA satellites) (see Fig. 3.3). As observed, target data is significantly more accurate than that of the chasers, with over 75% of targets known to have uncertainties between 5 and 30 meters in the last 24 hours before TCA, and only 5.7% showing uncertainties greater than 100 meters. This discrepancy is likely due to several factors, including the availability of onboard devices that relay SSA information, such as GNSS or passive RF measurement systems, and the larger size of ESA satellites compared to many of the debris pieces constituting the chasers.

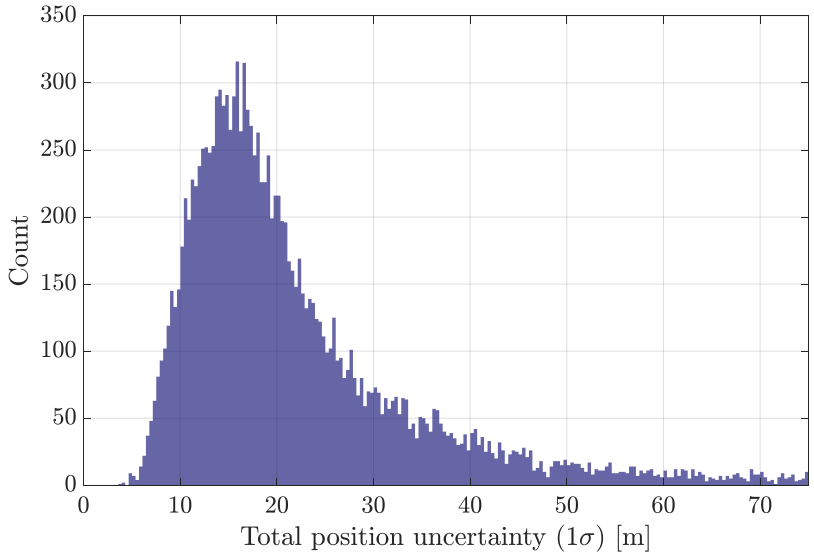

Fig. 3.3 Distribution of positional uncertainties for target objects appearing in CDMs between 0.5 and 1.1 days before TCA

The positional accuracy available for targets at the time of observation cannot be precisely determined at this stage. A lower limit on the minimum observation time can only be set by ensuring that observations are not made too close to the TCA, as the satellite needs sufficient time to plan and execute a fuel-efficient maneuver. In this context, the maximum observation time is considered to be half an orbit before TCA, as this marks the last opportunity for the satellite to perform a tangential

maneuver. ESA satellites commonly execute maneuvers half an orbit before TCA, providing a balance between minimizing disruption to routine satellite operations and ensuring fuel efficiency. However, positional uncertainties at half an orbit before TCA may underestimate those present at earlier observation times. To quantify this requirement, an estimate of statistically favorable observation times must be first established.

Among the remaining application-specific features, the target's material and cross-sectional area are the only ones that can be more easily quantified based on a review of available literature on the mass and size distribution of space objects. For the other features, such as relative distance, angular rates, and total visibility time within potential observation windows, no readily available data exists, except for the required positional uncertainty assessed earlier in this section. To assess these aspects, an in-depth investigation of the orbital dynamics of conjuncting objects in LEO must be performed.

3.2 Orbital dynamics analysis

This section characterizes the orbital dynamics and kinematics of encounters between conjuncting objects in LEO prior to their TCA without making specific assumptions about onboard sensors.

3.2.1 Data collection on past conjunction events

The data used in this analysis has been collected through the SOCRATES web service [10] offered by the Center for Space Standards & Innovation (CSSI), which every day publishes a list of forecasted conjunctions for the coming week. Besides reporting general information on each event such as the collision probability and the predicted TCA, orbital data are also provided for each object in the form of TLEs, as shown in the example of Fig. 3.4.

Action	NORAD Catalog Number	Name	Days Since Epoch	Max Probability	Dilution Threshold (km)	Min Range (km)	Relative Velocity (km/sec)
				Start (UTC)	TCA (UTC)	Stop (UTC)	
TLE Data	45437	ONEWEB-0092 [+]	1.145	1.708E-04	0.065	0.094	14.378
	31990	FENGYUN 1C DEB [-]	1.804	2023 Jan 12 06:55:32.784	2023 Jan 12 06:55:33.132	2023 Jan 12 06:55:33.479	

Fig. 3.4 Data reported by SOCRATES on a conjunction predicted for January 12, 2023 [11]

More accurate orbital information on conjunction events could be found in CDMs. However, there is currently only one large database of publicly available CDMs [12], but it contains partial information that prevents the reconstruction of kinematics before TCA. Conversely, TLEs allow for a straightforward propagation of the orbital states both forwards and backwards in time, but they do not include any uncertainty information. Nevertheless, TLEs error levels have little influence on the results of this analysis, as it will be shown in Section 3.2.5.

A web-scraping algorithm has been used to automatically retrieve data from the website three times per day that is the rate at which new information is uploaded

online, over the period from April 26 to June 7, 2022. Additional data has been collected from past SOCRATES reports dating from January to March 2022.

For a more realistic and meaningful analysis, only high-interest conjunctions meeting specific criteria have been retained, such as a maximum distance at the closest approach of 1 km. To limit propagation error, conjunctions for which the available TLEs were generated more than 2 days before TCA have been discarded. Only events occurring inside LEO have been retained, as this is the target orbital region for the designed system. Conjunctions between members of the same constellation or in formation flying have also been neglected, as in those cases satellites are more realistically maneuvered frequently to keep safe relative distances. In fact, SOCRATES reports are always more than half occupied by Starlink-Starlink approaches, which however never turn into actual collisions. Finally, to avoid repetitions, only one set of data has been retained per conjunction, since most events appeared several times in subsequent reports following updates on objects' position. The dataset containing the closest information to TCA has been kept for each conjunction. The obtained database includes data on 10,960 unique events, involving 21,920 objects, and is available on Mendeley Data (http://dx.doi.org/10.17632/yfcn6b52yz.1), along with all necessary information for replicating the analysis described here.

3.2.2 Orbital and kinematics features of conjuncting objects

Fig. 3.5 shows the distribution of mean altitudes (h), orbital eccentricities (e) and inclinations (i) of the objects. The altitude is taken as the difference between the semi-major axis and the equatorial Earth's radius.

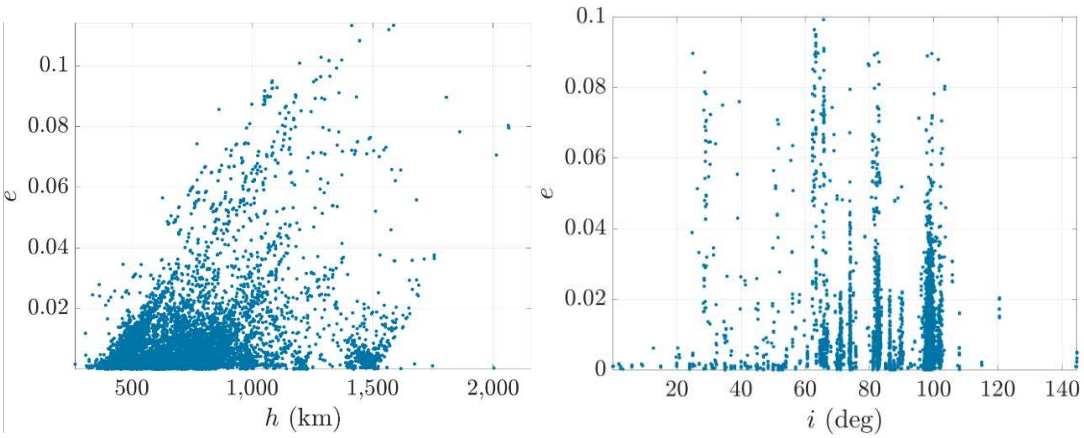

Fig. 3.5 Mean altitude, eccentricity, and inclination of the objects [11]. Objects with $h > 2{,}000$ km or eccentricities > 0.1, corresponding to less than 1% of cases, have been omitted for clarity.

As might be expected, most dangerous approaches occur below 1,000 km of altitude, where the spatial density is the highest. Conjuncting objects typically have very similar orbital periods, with a difference of less than one minute in 77% of the cases and less than two minutes in 88% of the cases. In addition, they usually share similar orbital shapes, as 87% of all orbits are nearly-circular ($e < 0.01$) and 96% of the remaining still have moderate eccentricity ($e < 0.1$). The inclination distribution

shows a high prevalence of nearly-polar orbits, with 78.23% of objects having inclinations between 80 and 100 deg.

Because of these features, conjuncting orbits usually exhibit a similar geometry to that illustrated in Fig. 3.6, with two points of close orbital proximity on diametrically opposite sides, where the two objects regularly encounter before TCA due to their temporal synchronization. The nearly-periodic nature of this peculiar kinematics is investigated more in detail in Section 3.2.2.1.

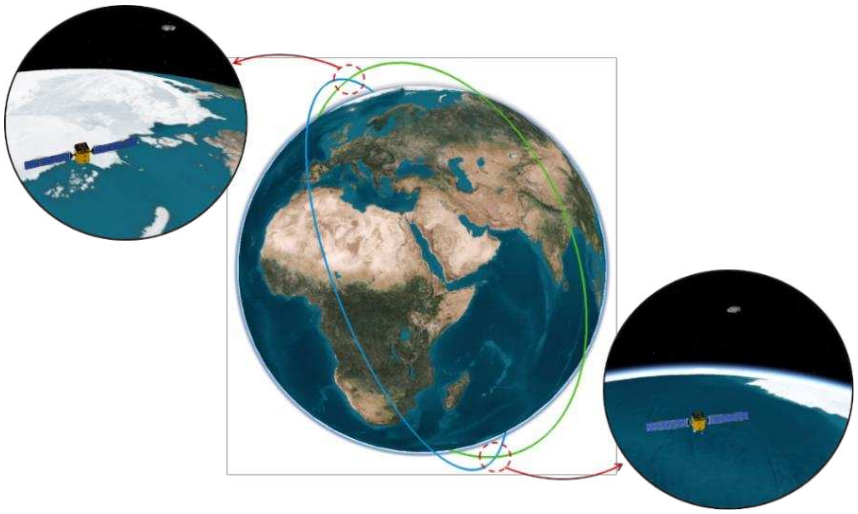

Fig. 3.6 Typical geometry of conjuncting orbits in LEO [11]

Although only conjunctions in LEO have been selected, in 0.63% of the cases one of the two objects crosses the LEO region for just a portion of its orbit and has a marked orbital eccentricity. These cases always involve conjuncting objects with quite different orbits and whose motion is significantly out of time phase.

Fig. 3.7 shows the distribution of relative velocities and impact angles (θ) at TCA. The impact angle is taken as the angle between the projections of the velocity vectors of the two objects on the local horizontal plane of either object, which of the two makes no difference in the analysis. This angle is useful to describe the geometry of a conjunction, which can be categorized as head-on ($135° < \theta < 180°$), cross-track ($45° < \theta < 135°$) or overtaking ($0° < \theta < 45°$).

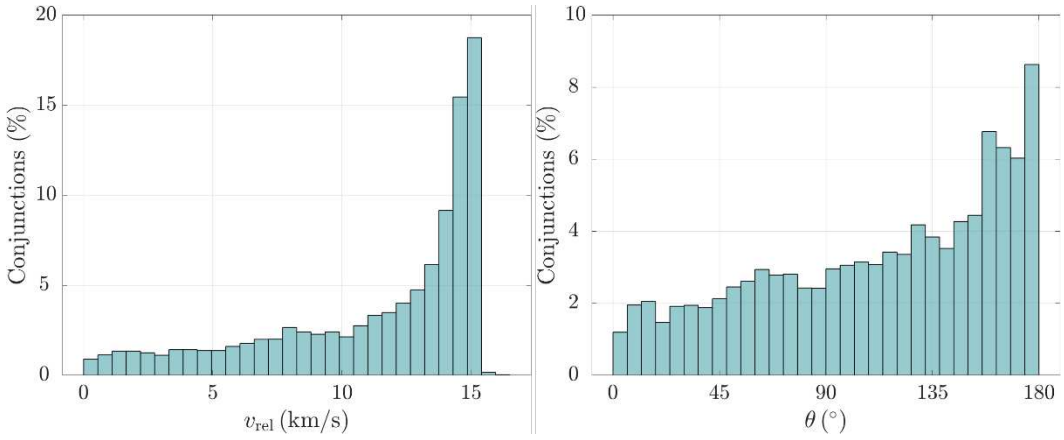

Fig. 3.7 Relative velocities (*left*) and impact angles (*right*) of conjuncting objects at TCA [11]

Since most objects in LEO travel with similar speeds (7–8 km/s), the different values of v_{rel} are mainly due to different conjunction geometries. Fig. 3.7 suggests that most encounters occur with a head-on geometry, i.e., between objects traveling in nearly opposite directions, thus with high relative speeds and kinetic energies. The following example provides an intuitive explanation of why this occurs.

Consider the two scenarios of Fig. 3.8, both of which illustrate two objects traveling in circular coplanar orbits of similar radii. The two objects on the left are orbiting with opposite direction of rotation (i.e., one orbit is prograde, the other is retrograde), whereas the objects on the right have the same direction of rotation (i.e., both orbits are either prograde or retrograde).

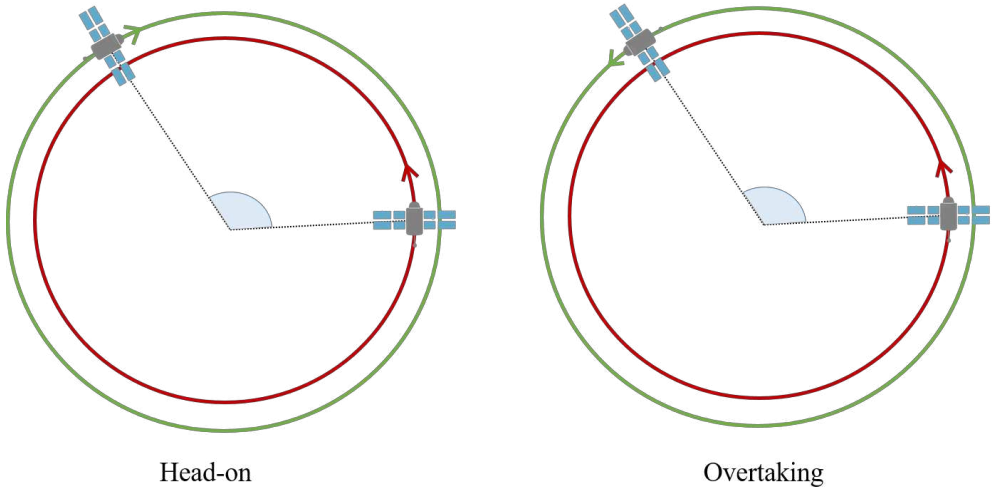

Fig. 3.8. Example scenarios of head-on (*left*) and overtaking (*right*) conjunctions

For the scenario on the left, it can be expected that the objects will close pass by each other several times during their motion (about once every half orbit), each time with a perfectly head-on geometry (θ=180°).

In contrast, the objects on the right are traveling in the same rotational direction and with a similar velocity, so their relative distance evolves much more slowly over time. Consequently, it takes much longer before the phasing angle that exists between the two reduces to 0°, which would eventually lead to an overtaking encounter (θ= 0°). In addition, the time required by the objects get close may be so large that the concurrent nodal precession effect due to the Earth-oblateness may bring the two orbits into very different orbital planes, such that the two objects will never actually encounter. Therefore, considering a generic satellite in LEO, and assuming that a similar number of other objects are traveling in opposite and parallel direction to it, it is reasonable to expect more head-on conjunctions than overtaking ones over any given time interval.

This evidence is relevant for the design of any space-based system for debris monitoring, even those not focused on collision avoidance. Since head-on conjunctions are more frequent, the spacecraft's surface facing the direction of motion is exposed to the highest debris flux. Therefore, to maximize detection rates, an effective design would likely involve placing the sensor on the front surface.

An analysis using ESA's DRAMA (Debris Risk Assessment and Mitigation Analysis) software is conducted to better quantify the differential debris flux across various spacecraft surfaces. Specifically, the MIDAS tool within DRAMA is utilized, which enables the estimation of debris and meteoroid impact flux levels for Earth-orbiting spacecraft based on user-defined parameters (e.g., orbit, dimensions, mass, and drag coefficient). To model the space debris population, the software leverages the widely validated ESA's MASTER representation of the debris environment. In the simulation, a cube-shaped spacecraft with a 5-meter side in a Sun-synchronous orbit at an altitude of 780 km is considered. The satellite maintains an Earth-oriented attitude, and the analysis period spans from the start to the end of 2020.

Figure 3.9 illustrates the estimated number of impacts versus object diameter for two of the spacecraft's surfaces: the front and rear surfaces.

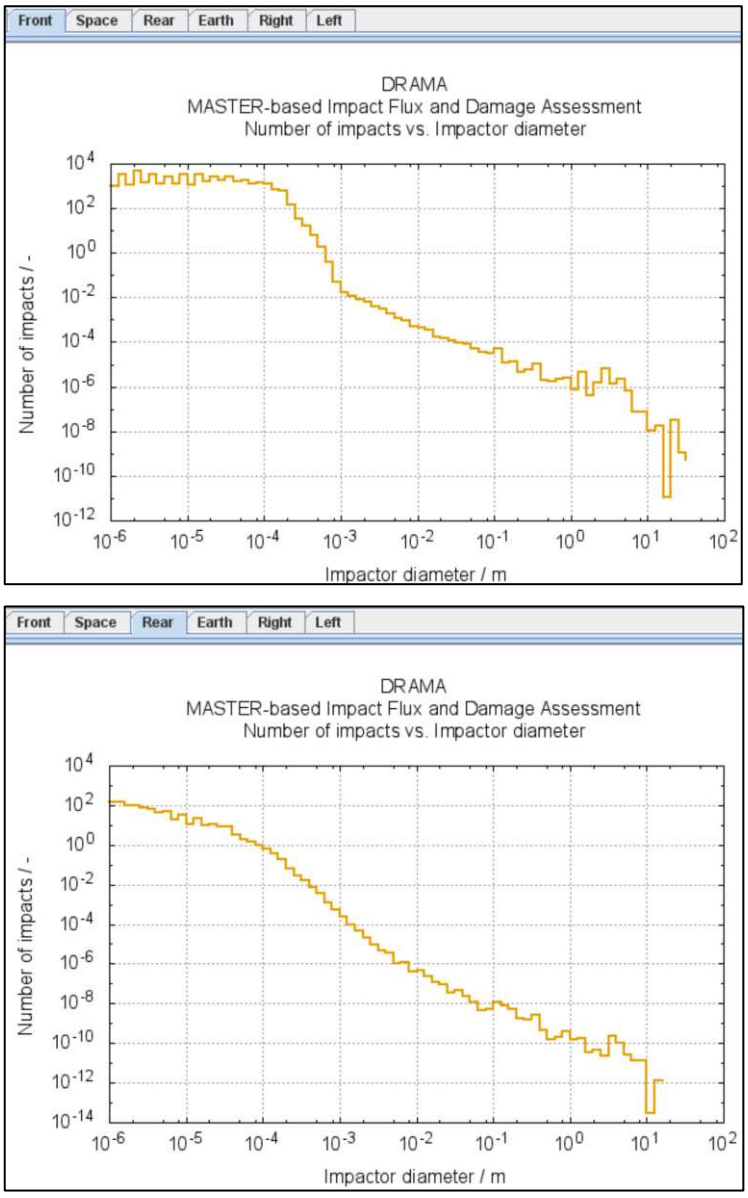

Fig. 3.9 Number of impacts vs objects diameters for the front surface (*top*) and the rear one (*bottom*)

The front surface's normal vector is aligned with the flight direction, while the rear surface's normal vector points opposite to the flight direction. Due to this definition, the number of impacts on the front surface is indicative of the amount of objects striking with a head-on geometry, while objects impacting on the rear surface are essentially approaching the satellite from behind with an overtaking geometry. As it can be noted, the number of impacts on the front surface is consistently higher by approximately 1–2 orders of magnitude across all object diameters.

3.2.2.1 Temporal periodic patterns in the relative motion of conjuncting objects

In this section, a simplified model of the kinematics of conjuncting objects in LEO is used to study the temporal periodic patterns underlying their relative motion.

As more than 99% of those objects have moderate eccentricities, the considered model assumes circular Keplerian (i.e., unperturbed) orbits, allowing the problem to be treated analytically while still retaining the necessary accuracy for the analysis.

Consider the motion of two objects in circular orbits of arbitrary radii R_1 and R_2 and whose orbital planes have a relative inclination angle i_R. This latter is defined as the angle between the normal vectors to the orbital planes of the two bodies and can range between 0° and 180° [13]. Referring to Fig. 3.10, assume a fixed X, Y, Z-coordinate system where the X, Y-axes lie on the first object's orbital plane and the X-axis is aligned with the line of intersection of the two orbital planes. Let $t = 0$ identify the TCA between the objects and assume that both lie on the positive axis X at this time, thus reaching their closest possible distance $(R_2 - R_1)$. Although actual conjuncting objects do not exactly achieve the minimum possible distance allowed by their orbits, they generally come close to it, especially in particularly high-risk events.

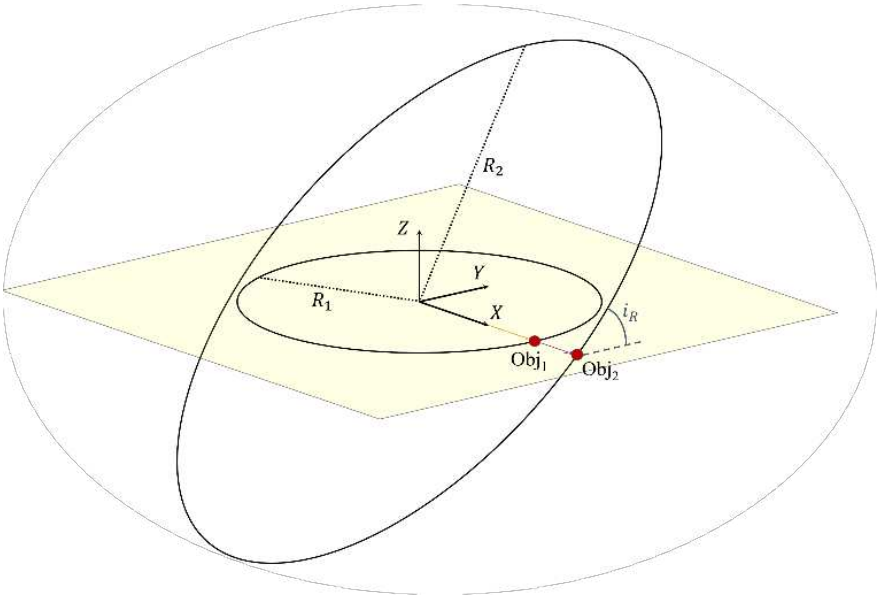

Fig. 3.10 Position of the two objects at time $t = 0$ relative to the X, Y, Z-reference frame [11]

The motion of the two bodies as a function of time can be expressed in the X, Y, Z-reference frame as:

$$\boldsymbol{r}_1(t) = R_1 \begin{bmatrix} \cos(n_1 t) \\ \sin(n_1 t) \\ 0 \end{bmatrix}$$
$$\boldsymbol{r}_2(t) = R_2 \begin{bmatrix} 1 & 0 & 0 \\ 0 & \cos(i_R) & -\sin(i_R) \\ 0 & \sin(i_R) & \cos(i_R) \end{bmatrix} \begin{bmatrix} \cos(n_2 t) \\ \sin(n_2 t) \\ 0 \end{bmatrix} \tag{3.1}$$

where n denotes the orbital angular velocity, which is linked to the orbital period T through the relation:

$$n = 2\pi/T \tag{3.2}$$

As the objects proceed in their orbits, their relative position r_{rel} is given by:

$$\boldsymbol{r}_{\text{rel}}(t) = \boldsymbol{r}_2(t) - \boldsymbol{r}_1(t) = \begin{bmatrix} R_2\cos(n_2 t) - R_1\cos(n_1 t) \\ R_2\sin(n_2 t)\cos(i_R) - R_1\sin(n_1 t) \\ R_2\sin(n_2 t)\sin(i_R) \end{bmatrix} \tag{3.3}$$

and their separation (or miss-distance) $r_{\text{rel}}(t)$ is simply the norm of $\boldsymbol{r}_{\text{rel}}(t)$. By taking the square of $r_{\text{rel}}(t)$, and after some manipulation, leads to:

$$\begin{aligned} r_{\text{rel}}^2(t) &= R_1^2 + R_2^2 - 2R_1R_2\big(\cos(n_1 t)\cos(n_2 t) + \cos(i_R)\sin(n_1 t)\sin(n_2 t)\big) = \\ &= R_1^2 + R_2^2 - 2R_1R_2 \cdot g(t) \end{aligned} \tag{3.4}$$

It is shown that the function $g(t)$, which groups the time-dependent terms of Eq. (3.4), can be decomposed into the linear combination of elementary sine and cosine waves with frequencies $n_2 - n_1$ and $n_2 + n_1$, by stating the following problem:

$$g(t) = \sum_{k=1}^{2} \left[a_k \cos\Big(\big(n_2 - (-1)^k n_1\big)\, t\Big) + b_k \sin\Big(\big(n_2 - \big(-1^k\big)\, n_1\big)\, t\Big)\right] \tag{3.5}$$

By equating the two expressions of $g(t)$ from Eqs. (3.4), (3.5) and solving for the unknown coefficients a_k, b_k, yields:

$$\begin{cases} a_1 = \dfrac{1 + \cos(i_R)}{2} \\ a_2 = \dfrac{1 - \cos(i_R)}{2} \\ b_1 = b_2 = 0 \end{cases} \tag{3.6}$$

Hence:

$$g(t) = \frac{1 + \cos(i_R)}{2}\cos\big((n_2 - n_1)\, t\big) + \frac{1 - \cos(i_R)}{2}\cos\big((n_2 + n_1)\, t\big) \tag{3.7}$$

The two frequencies $n_2 - n_1$ and $n_2 + n_1$ can be expressed in terms of the corresponding temporal periods through Eq. (3.2):

$$n_2 - n_1 = \frac{2\pi}{T_2} - \frac{2\pi}{T_1} = \frac{2\pi}{\frac{T_1 T_2}{T_1 - T_2}} = \frac{2\pi}{T_L}$$
$$n_2 + n_1 = \frac{2\pi}{T_2} + \frac{2\pi}{T_1} = \frac{2\pi}{\frac{T_1 T_2}{T_1 + T_2}} = \frac{2\pi}{T_S} \quad (3.8)$$

where the sub-scripts L, S are used to identify the longest and shortest period between the two. Substituting Eqs. (3.7), (3.8) inside Eq. (3.4) yields:

$$r_{\text{rel}}^2(t) = R_1^2 + R_2^2 - 2R_1R_2\left[\frac{1+\cos(i_R)}{2}\cos\left(\frac{2\pi}{T_L}t\right) + \frac{1-\cos(i_R)}{2}\cos\left(\frac{2\pi}{T_S}t\right)\right] \quad (3.9)$$

and so the miss-distance is:

$$r_{\text{rel}}(t) = \sqrt{R_1^2 + R_2^2 - 2R_1R_2\left[\frac{1+\cos(i_R)}{2}\cos\left(\frac{2\pi}{T_L}t\right) + \frac{1-\cos(i_R)}{2}\cos\left(\frac{2\pi}{T_S}t\right)\right]} \quad (3.10)$$

Eq. (3.9) shows that the evolution of $r_{\text{rel}}^2(t)$ is given by the superposition of two sinusoidal functions with different periods (T_L and T_S), whose relative weight depends on i_R. Despite the presence of the square root in Eq. (3.10), it can be shown that $r_{\text{rel}}(t)$ has the same frequency content of $r_{\text{rel}}^2(t)$. Indeed, by taking the first derivative of both Eqs. (3.9), (3.10), it can be verified that the functions $r_{\text{rel}}^2(t)$ and $r_{\text{rel}}(t)$ have the same points of local maxima and local minima, meaning that they feature the same oscillatory pattern.

The superposition of the two sinusoids is evident in the example of Fig. 3.11, which shows the evolution of r_{rel} prior to TCA ($t < 0$) for two objects orbiting the Earth at 700 km and 800 km of altitudes and considering three different values of i_R. For the considered altitudes, T_L = 3.29 days and T_S = 49.83 minutes, which reflect the long- and short-period oscillations noticeable in the three graphs.

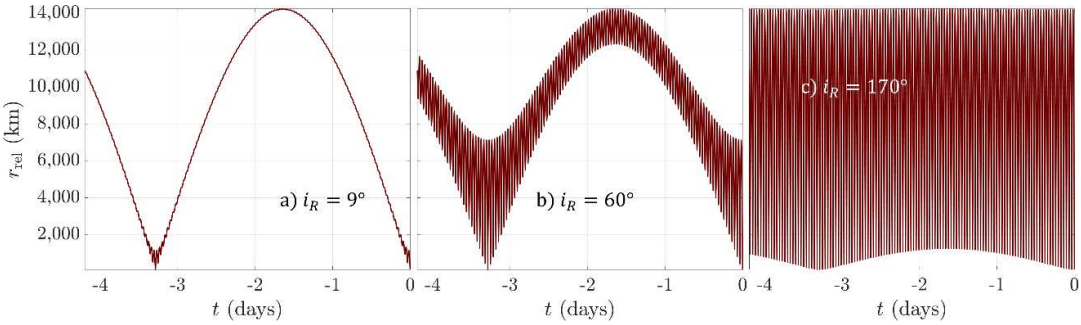

Fig. 3.11 Miss-distance between two circular Earth orbits with radii $R_1 = r_E$ + 700 km and $R_2 = r_E$ + 800 km, where r_E is the Earth's radius, considering three values of i_R: a) 9°, b) 60° and c) 170° [11]

For i_R close to 0°, i.e., nearly-coplanar orbits with same direction of rotation, $\cos(i_R) \sim 1$ and so the miss-distance is governed by the long periodicity T_L, as in Fig. 3.11.a). This case well reflects, for example, the relative motion between any couple of planets in the Solar System, whose orbits have all the same rotation direction and are close to the ecliptic plane, except for Mercury. In fact, T_L corresponds to the well-

known formula of the synodic period, which gives the time required by two planets to return to a same angular position with respect to the Sun. For i_R close to 180°, i.e., nearly-coplanar orbits with opposite direction of rotation, $\cos(i_R) \sim -1$ and the miss-distance is mostly governed by the short periodicity T_S, as shown in Fig. 3.11.c). For each intermediate case, such as that in Fig. 3.11.b), both frequencies are clearly distinguishable in the relative motion.

Regarding conjuncting objects in LEO, i_R can assume all values between 0° and 180°, with a skewed distribution toward i_R = 180°. A good approximation of this distribution is given by that of the impact angle θ shown in Fig. 3.7, given that, for circular orbits, i_R and θ coincide. Therefore, apart from few rare cases where i_R is close to 0°, the contribution of the T_S-periodic sinusoid is always evident the relative motion of conjuncting objects in LEO. In addition, as seen in Section 3.2, those objects generally feature very similar orbital periods. Considering the limit case $T_1 = T_2$, T_S corresponds to exactly half of the orbital period of the two objects. For these reasons, the relative distance between conjuncting objects typically reach local minima every half-orbit prior to TCA, and more precisely with a periodicity of T_S.

3.2.3 Orbit propagation

The trajectory of each couple of conjuncting objects in the database is reconstructed over the 2-days preceding their predicted closest approach. For the orbital propagation, Vallado's Matlab® implementation of the SGP4 propagator [14] is used. SGP4 is an analytical model accounting for the periodic and secular effects caused by atmospheric drag, Earth's oblateness, third body perturbations (Sun and Moon) and gravitational resonance effects. When TLEs are being used, SGP4 is the most faithful propagator as it was specifically designed for use in conjunction with them. Starting from a TLE as input, SGP4 can analytically estimate an object's position $\boldsymbol{r}$ and velocity $\boldsymbol{v}$ at any point in time, without the need for numerical integration.

For each couple of objects, $\boldsymbol{r}$ and $\boldsymbol{v}$ are evaluated at the same time instants, and the relative kinematics is reconstructed in parallel by computing at each point the relative distance r_{rel}, the relative velocity v_{rel} and the angular rate ω. The first two are simply obtained as $\|\boldsymbol{r}_2 - \boldsymbol{r}_1\|$ and $\|\boldsymbol{v}_2 - \boldsymbol{v}_1\|$ respectively, where the sub-scripts 1 and 2 denote the two objects. To calculate ω, it is assumed that object 1 (arbitrary choice) is a satellite hosting a tracking sensor whose Field of View (FoV) direction coincides with the surface normal of the satellite's front surface. Identifying with $\hat{\boldsymbol{s}}$ the direction of the sensor axis, ω is calculated at each instant as the time variation of the angle between $\hat{\boldsymbol{s}}$ and the relative position $\boldsymbol{r}_{\text{rel}}$.

For onboard radar or LiDAR sensors, $\hat{\boldsymbol{s}}$ and $\boldsymbol{r}_{\text{rel}}$ should be as closely aligned as possible during the observation window to correctly track the secondary object. Therefore, ω provides information on how fast the FoV of such sensors would need to be rotated in a real scenario. The definition of $\hat{\boldsymbol{s}}$ further assumes that the spacecraft maintains an Earth-pointing attitude orientation, as done by most active satellites in LEO. Whereas, the sensor has been assumed to be mounted on the front surface as this latter is exposed to the highest flux of debris, as previously demonstrated.

Given the huge relative velocities of orbital encounters, to correctly evaluate the objects' kinematics a fine propagation time-step (Δt) is required to compute the

trajectories. Here, Δt is calculated at each instant so as to always ensure a resolution of 1 km in the computed $r_{\text{rel}}(t)$ for each couple of objects. Higher resolutions would make poor sense as TLEs are not generally reliable at a sub-kilometer level [14]. Unfortunately, this leads to evaluate millions of points just for the trajectory of a single object, which translates into a total estimated time of around one month to propagate the entire database. Therefore, a more targeted strategy is used to reduce the computational burden.

As the overall purpose is the characterization of potential observation opportunities, instead of propagating all trajectories over the entire two days preceding TCA, the focus can be placed on the points of local minima of r_{rel}, since there is where the best chances of making observations are. Considering that most orbits have moderate eccentricities and recalling the discussion of Section 3.2.2.1, the times of local minima of $r_{\text{rel}}(t)$ can be approximately located for each couple of objects as follows:

$$t_{min,j} = \text{TCA} - j \cdot T_S = \text{TCA} - j \cdot \frac{T_1 T_2}{T_1 + T_2} \quad \text{with} \quad j = 1, 2, 3, \ldots \tag{3.11}$$

where the TCA is known from the database information (see Fig. 3.4) and the j-loop is stopped when the last computed $t_{min,j}$ is farther than 2 days from TCA. Although Eq. (3.11) applies primarily to circular orbits, it produces negligible errors when both objects have moderate eccentricities (e < 0.1). For example, using Eq. (3.11) to calculate the local minima for conjunction no. 67 in the database, which involves an object with eccentricity of 0.108, yields a maximum deviation of 2.95 minutes for one of the local minima as compared with the full trajectory solution. Hence, $t_{\text{min},j}$ represent good starting points from which the actual minima are very close. The latter are computed in a second step by locally minimizing r_{rel} on short intervals (±5 minutes) around each $t_{\text{min},j}$. Here, the minimization is carried out by means of Brent's algorithm for functions of one variable [15], which converges very rapidly to the sought minima.

Figure 3.12 provides a visual comparison of a point-by-point calculated miss-distance with the location of its local minima obtained using the above procedure[5]. Once the points of true minima are known, the objects' trajectories are only propagated on short intervals around the minima, as in the example of Fig. 3.13. For each interval, the propagation is stopped at the two points where the miss-distance exceeds 2,500 km, a value beyond which it has been assumed that making quality observations becomes difficult for a satellite, especially with a secondary payload.

Note from Fig. 3.13 that the trajectory is not propagated across the global minimum at TCA, because the interest is only on the previous encounters. The above described procedure has been applied for all conjunctions where both objects had a smaller eccentricity than 0.1, for which minimization by Brent's algorithm always succeeded in finding the sought minima. In all other cases (less than 1%), the trajectories have been fully propagated over the two days before TCA.

[5] The graph has been plotted using conjunction no. 25 from the database, which involves the active Ningxia-1 3 satellite and a piece of debris from the Yuanhai 1-02 satellite.

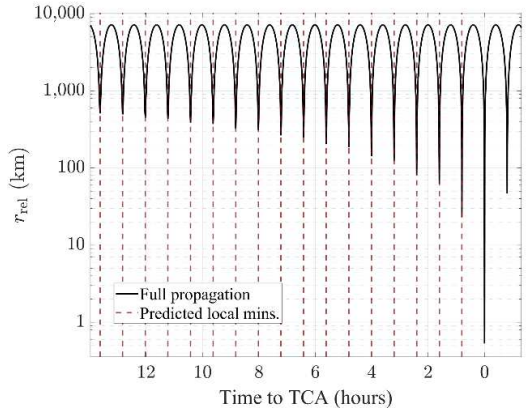

Fig. 3.12 Fully propagated relative trajectory (*solid line*) vs predicted times of local minima (*dashed lines*) [11]

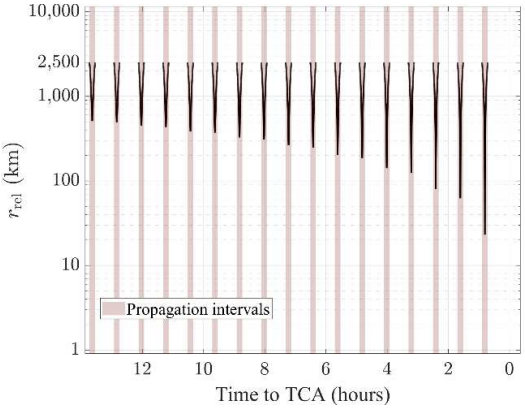

Fig. 3.13 Propagation intervals [11]

Fig. 3.14 shows the evolution of the miss-distance for nine examples of conjunctions from the database[6]. Unlike as seen in the graphs of Fig. 3.11 obtained with the simplified model, here the local minima do not always decrease monotonically as the TCA approaches. An alternating trend (up and down) between adjacent minima is especially evident in cases a), d), g) and i). It was verified with some simple tests that this effect is due to the non-zero orbital eccentricities of real-world objects, which cause the distance between conjuncting orbits to be slightly different at the two points of proximity where the encounters occur.

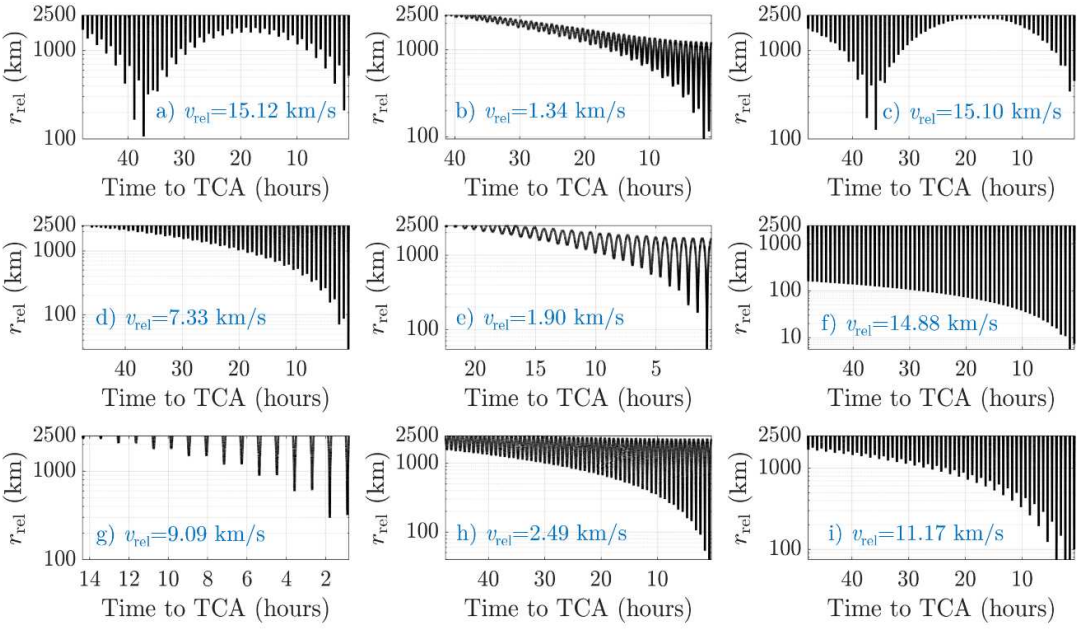

Fig. 3.14 Miss-distance evolution for a few conjunction events. In blue are reported the relative velocities at TCA [11]

Another distinctive feature is shown in cases a) and c), where the two objects

[6] The graphs correspond in alphabetical order to conjunctions nos. 4014, 40, 37, 153, 91, 3515, 2943, 96, 4007 from the database

experience an additional close approach several hours before the closest one. This occurs when conjuncting objects have a particularly different orbital period, such that the value of T_L (see Eq. (3.8)) is smaller than the two days time-span considered here, so another close approach is visible in the plots. In fact, orbital periods differ by less than 1 minute in all cases of Fig. 3.14 except for a) and c), where the difference is larger than 4 minutes, resulting in a T_L of 37.94 hours in case a) and 36.43 hours in case c). Lastly, it can be noticed that objects with low relative velocities (around 2 km/s) remain in proximity more continuously in the hours before TCA because of their nearly parallel motion in the along-track direction.

3.2.4 Analysis of observation opportunities

The propagated trajectories are analyzed in terms of relative distances, relative velocities, and other relevant features that contribute to determine whether the repeated encounters between conjuncting objects can actually translate into opportunities for making observations.

3.2.4.1 Relative distances

The relative distances are one of the aspects influencing how bright a target object will appear to an observer satellite. Other important factors are the size of the object, its material properties and the Sun phase angle, which is the angle formed between the Sun, the object and the spacecraft. In the case of NEOSSat, objects were regularly detectable from distances spanning 3,000 to 4,000 km. Nonetheless, the spacecraft was equipped with a 15-cm aperture telescope, whose SWaP is not compliant with the typical requirements of secondary payloads.

An overview of the minimum miss-distances achieved by conjuncting objects in the two days before TCA is shown in Fig. 3.15.

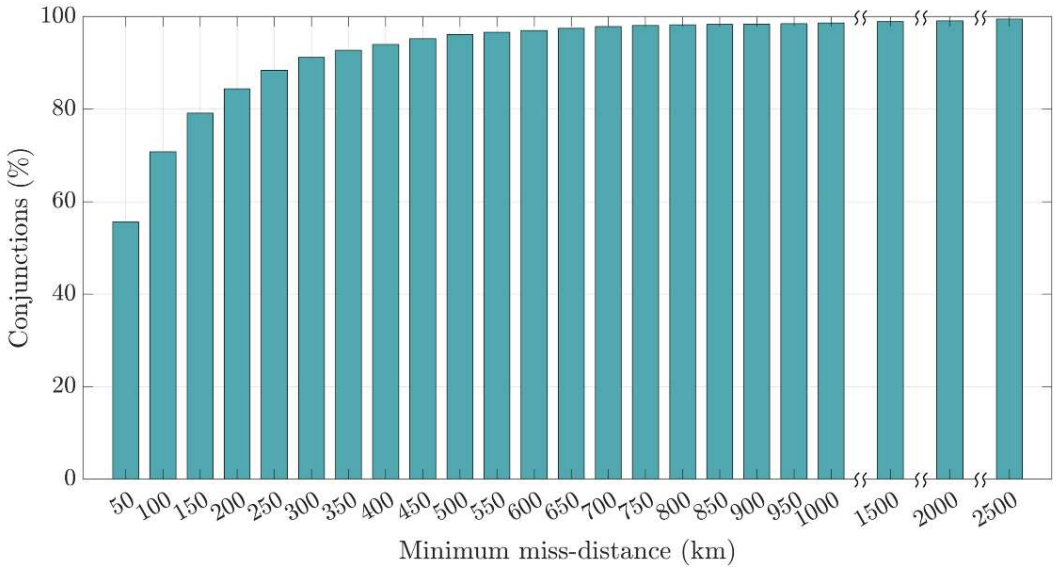

Fig. 3.15 Minimum miss-distance achieved by conjuncting objects in the two days before TCA (cumulative graph) [11]

It can be seen that around 70% of the times two objects make a pass at less than 100 km before making the closest approach.

Note that, even if a satellite was able to detect targets at a range of 1,000 km, a few secondary objects would still not be visible in the two days before TCA. Closer investigation of these cases revealed that they always involve one object with a marked orbital eccentricity, whose motion is out of phase with respect to that of the other object. An example of such scenario is given in Fig. 3.16, where one of the objects is a debris from Cosmos 2251 satellite that travels in nearly-circular orbit at 841 km of altitude, while the other is a piece of rocket body in Molniya orbit, with an eccentricity of 0.74 and a semi-major axis of 26,890 km. In this case, the two orbits form a larger synodic period that leads the objects to come close together about once every 3.3 days. A space-based observing strategy here would not bring any particular value over ground-derived data, especially because of the last available observing opportunity being too far away from TCA.

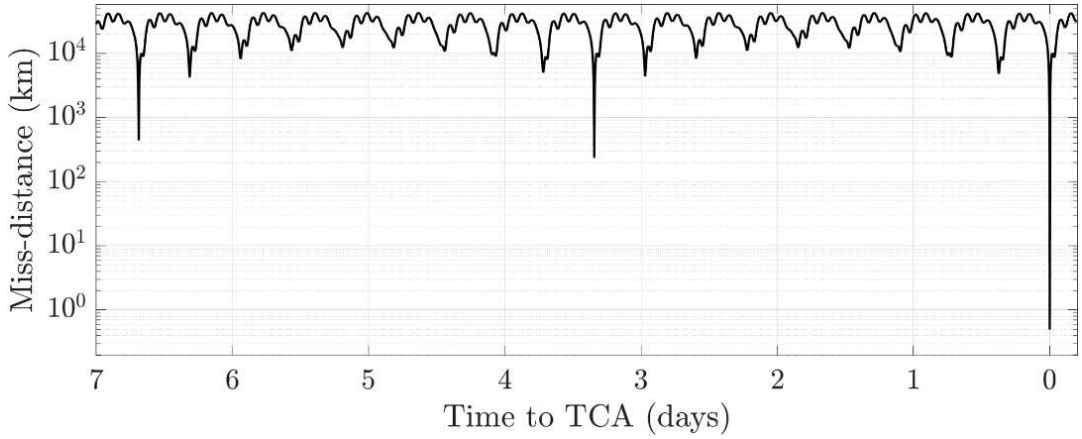

Fig. 3.16 Relative distance between an object in LEO and one in Molniya orbit [11]

3.2.4.2 Relative velocities and angular rates

The example of Fig. 3.17 shows that the local minima of r_{rel} correspond to local maxima in v_{rel}. Note that, as it is defined, v_{rel} does not coincide with the time derivative of r_{rel}, which would otherwise be zero in correspondence of the local minima of r_{rel}. The pattern of the relative velocity can greatly vary from case to case. A generally valid feature is that during the various encounters before TCA, the velocity reaches peak levels more or less similar to that reached at TCA. In other words, if v_{rel} is 3 km/s at TCA, it is unlikely to reach 15 km/s in the preceding passages. An interesting feature noticeable in Fig. 3.17 is that the velocity peaks can follow two different trends, one ascending and one descending, looking at the encounters two by two. This can occur when successive passages occur at opposite orbital points. In any case, the design of an onboard sensing system should primarily address relative velocities ranging between 13-15 km/s, as most conjunctions occur at those velocities (see Fig. 3.7) and they pose the biggest technical challenges.

Another key aspect concerns the angular rates experienced during the encounters, which may drive important considerations on the pointing performance required to onboard sensing system. The typical pattern of ω is shown on the right of Fig. 3.17. When two objects are still far apart before a generic encounter, the angular rate is almost null. As they get closer, ω rapidly increases until reaching a sharp peak at the

time of minimum distance, after which it decreases again.

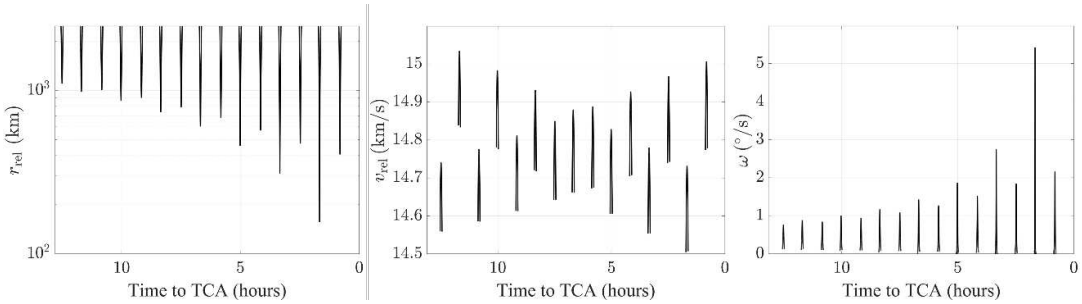

Fig. 3.17 Evolution of miss-distance (*left*), relative velocity (*center*) and angular rate (*right*) for conjunction no. 6 from the database [11]

The relationship between angular rates and relative distance is further illustrated in Fig. 3.18, which displays the angular rates observed for each couple of objects at their closest encounter before TCA, plotted against their relative distance. The graph clearly demonstrates a strong correlation: the closer the objects pass, the higher the angular rate.

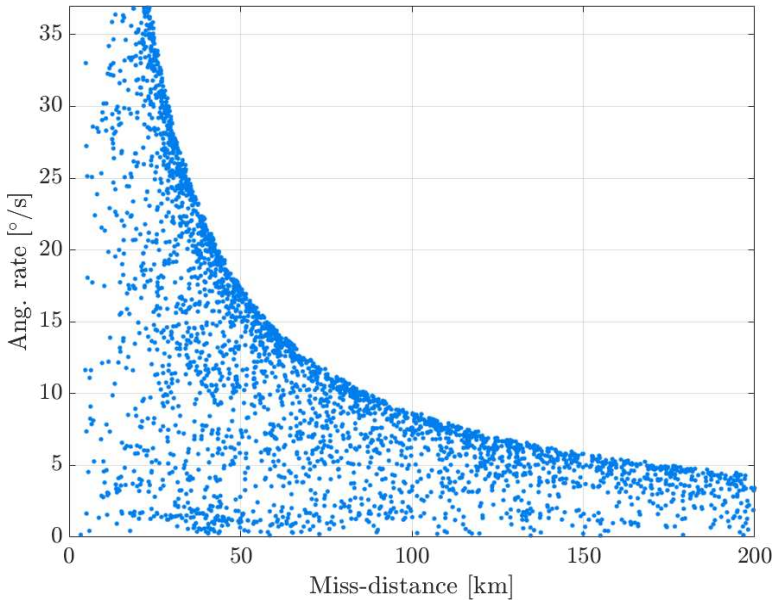

Fig. 3.18 Angular rate reached by each couple of objects in their closest encounter prior to TCA [11]

In quantitative terms, the peaks reached by ω during the orbits prior to TCA are typically extremely high. In more than 90% of the conjunctions, ω reaches more than 100°/s during the encounter occurring one orbit before TCA, if there is one. Encounters with a frontal geometry and involving close relative distances produce the highest values, often reaching over 1000°/s. These angular rates clearly exceed any realistic sensor or attitude pointing control capability. Therefore, the useful time for making observations during an observing window is limited by the maximum angular rate beyond which the observer satellite can no longer track the other object. If an object first becomes visible to the satellite when its angular rate is already too high for tracking, no data can be acquired. In the NEOSSat experiment, the satellite regularly lost track of its conjuncting objects once their relative distance fell below 250 km during the various passes [16]. As shown in Fig. 3.18, at such distances,

objects exhibit angular rates of approximately 0–4°/s. Therefore, for the next results, a threshold on the angular rate of 1°/s is assumed, beyond which secondary objects are considered not to be visible. It should be noted that this represents a realistic limitation for active sensors or narrow-FoV optical sensors (e.g., NEOSSat), where objects may traverse the entire FoV within a timeframe comparable to the exposure time. In contrast, this limitation does not apply to wide-FoV optical sensors, as better studied in Chapter 4.

3.2.4.3 Time to first opportunity

In order to provide a satellite with sufficient response time to execute a maneuver, observations should not be performed too close to a potential collision. However, the best observing opportunities tend to arise close to TCA, when conjuncting objects typically spend more time in close proximity and their future states can be predicted with greater accuracy. Therefore, the decision on when to execute a maneuver results in a trade-off between the amount of warning time and the probability of a false alert.

Currently, collision avoidance maneuvers are typically performed 0.5-1.5 revolutions before the expected collision by slightly firing in the direction of motion of the spacecraft [17]. Exceptions exist, but the current general trend is to reduce the time between maneuver execution and potential collision. In order to assess whether close passes before TCA would provide satellites with adequate warning times for maneuvering, an analysis of when secondary objects first become visible before the closest approach has been performed. Encounters where the angular rates were always above a threshold of 1°/s have not been considered as observing opportunities.

Results shown in Fig. 3.19 exhibit a strong dependence on the maximum distance at which an observer satellite would be able to distinguish a secondary object.

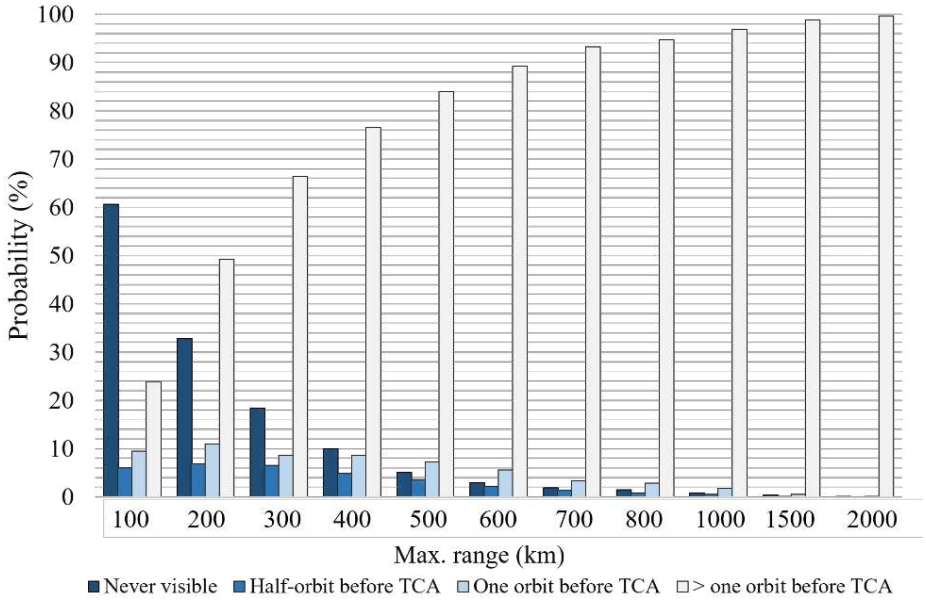

Fig. 3.19 Probability of when secondary objects first become visible depending on the maximum detection range of the sensor [11]

The timings are categorized into four classes to highlight the cases where objects first appear half or one orbit before TCA, i.e., when typically a maneuver decision has already been made. For the lowest values of the detection range considered, most of the objects are never visible and first opportunities tend to cluster towards TCA, making strategies of in-situ observations inefficient. Instead, starting from ranges of 500–600 km, about 90% of secondary objects would be detectable with adequate lead-time.

An interesting aspect can be noticed by comparing Fig. 3.15 with Fig. 3.19. Even though 70% of secondary objects pass within a distance of 100 km from their primary before TCA, Fig. 3.19 by contrast shows that 60% of objects would not be visible with a sensor range of 100 km. This is because most of the encounters below 100 km feature angular rates exceeding 1°/s, and were considered as valuable opportunities for making observations.

3.2.4.4 Average number and duration of observing windows

The number and duration of available observing opportunities determine the amount of information that can be collected on a target object. When multiple observation points are available, orbit determination can be performed to a higher confidence level.

Fig. 3.20 provides a statistic on the number of observation windows arising during the two days before TCA to a satellite that is able to detect targets at 500 km.

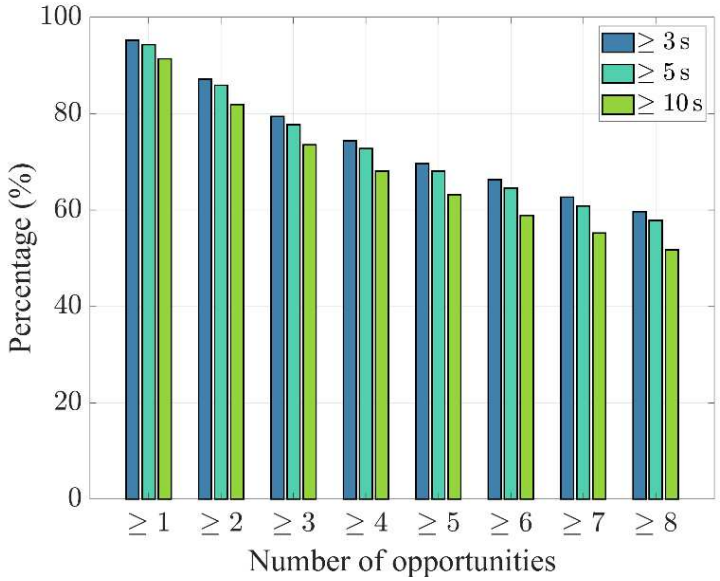

Fig. 3.20 Number of observing opportunities lasting more than 3 s, 5 s and 10 s during the two days before TCA and considering a maximum detection range of 500 km [11]

The graph shows how the number of opportunities varies by selecting different thresholds of the minimum windows duration. The duration has been calculated by considering that each two objects are in visibility from the time their distance falls below 500 km until their angular rate exceeds 1°/s. The FoV of the sensor is assumed to be correctly pointed toward the target at the time the range falls below the selected threshold, since the onboard available orbital data is processed each time to determine the azimuth/elevation sector from where the object is expected to appear.

Opportunities occurring half a revolution before TCA have been neglected from the count, assuming that a satellite would have generally already maneuvered by that time. For the considered value of the detection range, at least two opportunities lasting more than 10 seconds are available in more than 80% of the cases.

Finally, Fig. 3.21 shows the duration of the longest observing window for each event, considering several detection ranges. Assuming for instance that 10 seconds is a reasonable enough time for detecting and observing a target object, a range of 600 km guarantees at least one observing opportunity of this kind in about 90% of the cases. By increasing the range to 1,000 km, a one-minute opportunity is almost always available.

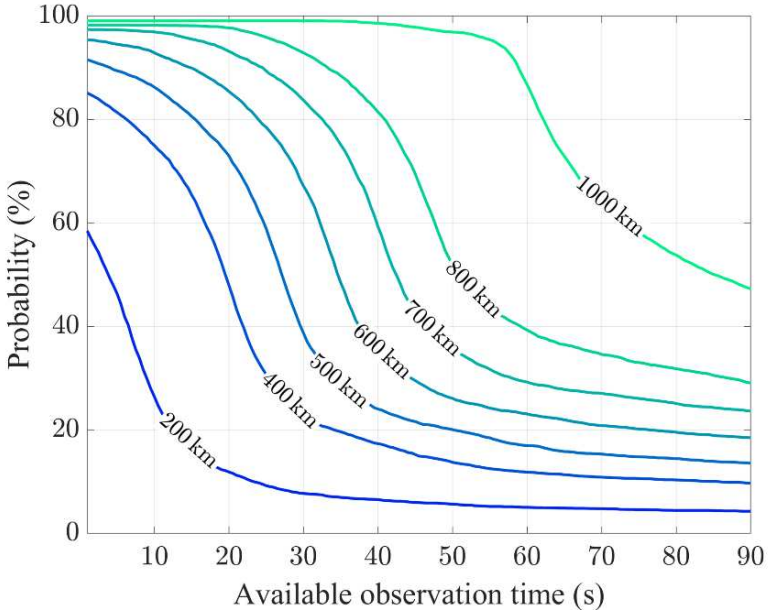

Fig. 3.21 Duration of the longest observing opportunity depending on the maximum detection range [11]

3.2.4.5 Azimuth and elevation angles

Observing a secondary requires the FoV to be properly aligned with the oncoming object direction. Here, an investigation on the provenance direction of secondary objects during the repeated encounters is done by analyzing their angular position evolution with respect to their primaries. The angular position of a secondary relative to its primary can be expressed in terms of azimuth and elevation angles. The azimuth A ranges from 0° to 360° and is defined within the primary's Local Horizontal Plane (LHP), whose normal vector alignes with the outward radial direction. The angle A is measured clock-wise from the projection of the primary's flight direction onto the LHP to the projection of the relative position vector. The elevation h ranges from -90° to 90° and is defined as the angle between the LHP and the relative position vector. For each couple of objects in the database, the role of secondary one has been assigned randomly.

The $A - h$ evolution can vary significantly depending on the specific trajectories of two objects. A couple of features can be highlighted by examining the values assumed by those angles at different relative distances. Fig. 3.22 displays the

distributions of A and h during the last encounter before TCA and for three different values of r_{rel}. The elevation angle is typically small regardless of the distances, and its distributions are nearly symmetrical around a mean value that changes depending on r_{rel}. h tends to assume values around -10° at distances of 1500 km, but it gradually increases toward 0° as the objects get closer. Analyzing distributions of h at longer distances than 1500 km has shown that the mean value remains close to -10°. Therefore, if a secondary object is visible at distances of >1500 km, it will typically appear from below the LHP of the primary, which should point its FoV at an elevation of about -10°. At a range of 1000 km, the mean elevation is -5°.

The A distributions all cluster towards 0° and 360°, meaning that the encounters prior to TCA are typically characterized by a frontal geometry, similarly to what occurs at TCA. This suggests that a sensor should be oriented in the satellite's direction of motion most of the times.

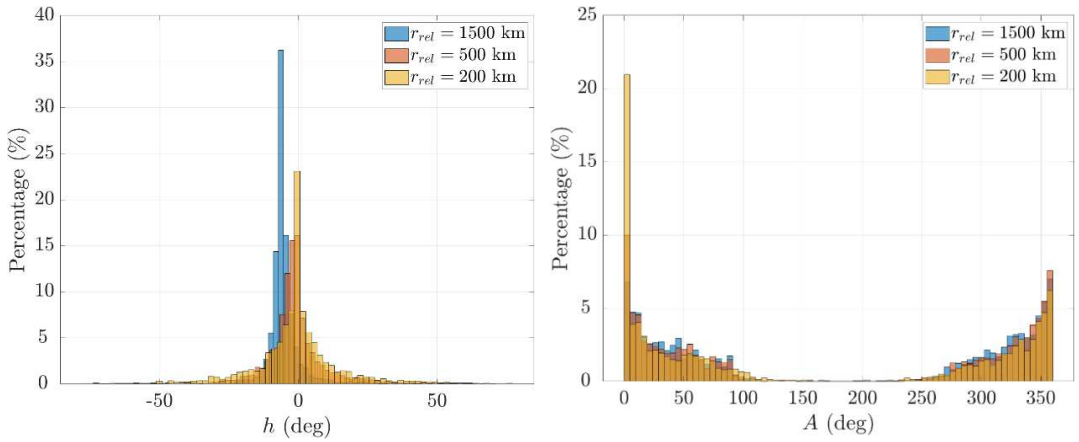

Fig. 3.22 Distribution of h (*left*) and A (*right*) at the last encounter prior to TCA [11]

3.2.5 Accuracy of the results

The results of the analyses in this chapter rely on orbits derived from TLE data, whose reliability is limited.

The accuracy of TLEs can vary considerably due to factors such as the altitude of the object, the occurrence of maneuvers, and the number and distribution of observations used to generate the TLE. To estimate the accuracy of the results in this chapter, which uses a sample of over 20,000 TLEs, a statistically representative rule is employed. According to [18], the positional error for LEO objects using TLE data can reach 1 km at the epoch and grows by 1–3 km per day of propagation when using the SGP4 propagator. Several other authors compared TLEs and numerical propagators or GPS-derived orbits, confirming comparable error levels. For instance, the authors in [19] report a typical growth rate of 1.5 km/day for the analyzed objects. As reported in [20], the authors in [21] find that 'the accuracy of the propagator is generally in the kilometer-level range.' Similarly, the studied cases in [22] show a positional error roughly lower than 5 km after two days of propagation. Analogous results were reported in [23], [24], [25], [26], and [27], with all works focusing on objects in LEO. Therefore, while in some cases positional errors can reach several tens of kilometers after a few days, the aforementioned rule

is considered reliable for representing the error across the entire dataset.

On one hand, errors in the kilometer level are certainly insufficient for accurately estimating the closest distance at TCA, which can be in the meter range. However, during encounters before TCA, the relative distances are considerably larger and so an error of few kilometers has a much smaller impact.

A simple analysis can be done to assess how the error on object position affects the calculated relative distances, since most of the results in this chapter are based on the latter. Denoting with $\boldsymbol{r}_1(t)$ and $\boldsymbol{r}_2(t)$ the nominal positional vectors predicted through TLEs, the true positional vectors can be expressed as:

$$\begin{aligned} \tilde{\boldsymbol{r}}_1(t) &= \boldsymbol{r}_1(t) + \boldsymbol{e}_1(t) \\ \tilde{\boldsymbol{r}}_2(t) &= \boldsymbol{r}_2(t) + \boldsymbol{e}_2(t) \end{aligned} \tag{3.12}$$

where $\boldsymbol{e}_1(t)$, $\boldsymbol{e}_2(t)$ are two error vectors, whose magnitude is assumed to be of 1 km at epoch and grows by 3 km per day of propagation. No assumption is made about the orientation of the error vectors, even though it is well known that the error component in the along-track direction is usually significantly greater than that in the other directions. Note that, as all TLEs were generated no more than 2 days away from the TCA, the maximum magnitude that each error vector can reach through propagation is 7 km (1 km + 2 days · 3 km/day). This can only occur for an object whose TLE was generated either exactly at TCA or 2 days before, otherwise the propagation time is always smaller than 2 days. The error between the true relative distance and the predicted one can be computed as:

$$\Delta r_{\text{rel}}(t) = \|\tilde{\boldsymbol{r}}_{\text{rel}}(t)\| - \|\boldsymbol{r}_{\text{rel}}(t)\| = \|\tilde{\boldsymbol{r}}_2(t) - \tilde{\boldsymbol{r}}_1(t)\| - \|\boldsymbol{r}_2(t) - \boldsymbol{r}_1(t)\| \tag{3.13}$$

By expanding and simplifying Eq. (3.13) eventually leads to:

$$\Delta r_{\text{rel}}(t) = \sqrt{\|\boldsymbol{r}_{\text{rel}}(t)\|^2 - 2\,\boldsymbol{r}_{\text{rel}}(t) \cdot \boldsymbol{e}_{\text{rel}}(t) + \|\boldsymbol{e}_{\text{rel}}(t)\|^2} - \sqrt{\|\boldsymbol{r}_{\text{rel}}(t)\|^2} \tag{3.14}$$

where $\boldsymbol{e}_{\text{rel}}(t) = \boldsymbol{e}_2(t) - \boldsymbol{e}_1(t)$. From Eq. (3.14), it can be verified that the error is maximized when the following two conditions are matched: 1) $\boldsymbol{r}_{\text{rel}}(t)$ is parallel to $\boldsymbol{e}_{\text{rel}}(t)$, and 2) the two error vectors are parallel and opposite. In this case, $\|\boldsymbol{e}_{\text{rel}}(t)\|$ becomes the sum of the magnitudes of the individual error vectors and Eq. (3.14) reduces to:

$$\begin{aligned} \Delta r_{\text{rel}}(t) \quad &= \sqrt{(\|\boldsymbol{r}_{\text{rel}}(t)\| \pm \|\boldsymbol{e}_{\text{rel}}(t)\|)^2} - \sqrt{\|\boldsymbol{r}_{\text{rel}}(t)\|^2} = \pm\,\|\boldsymbol{e}_{\text{rel}}(t)\| = \\ &= \pm(\|\boldsymbol{e}_1(t)\| + \|\boldsymbol{e}_2(t)\|) \end{aligned} \tag{3.15}$$

where the $\pm$ accounts for when $\boldsymbol{r}_{\text{rel}}(t)$ is directed in the same or opposite direction to $\boldsymbol{e}_{\text{rel}}(t)$.

Equation (3.15) has been used to plot the graph in Fig. 3.23, which shows the relative position uncertainty across a local minimum for a conjunction event from the database. Specifically, the lower and upper limits of the blue region have been computed using Eq. (3.15) and considering the error growth rule of 3 km/day previously mentioned.

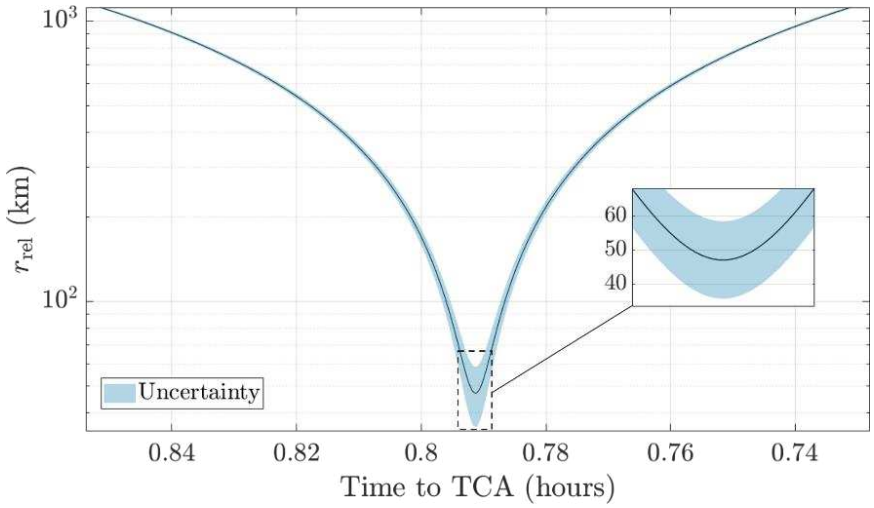

Fig. 3.23 Uncertainty in the relative distance across a local minimum [11]

Considering Eq. (3.15), the maximum theoretical error between the true and the calculated miss-distance is obtained if, in addition to the above two conditions, both objects' TLEs were generated either exactly at TCA or 2 days before. For example, if they were generated 2 days before, the maximum $\Delta r_{\mathrm{rel}}(t)$ possible occurs at TCA and is 14 km (7 km + 7 km). Although several unlikely conditions should align for this case to occur, a distance of 14 km is still small compared to the several hundreds to thousands of kilometers that separate objects during the orbits before TCA. In terms of duration of an observation window, if an encounter occurs with a high relative velocity (12–15 km/s), an error of 14 km on r_{rel} translates into an error of about one second on the estimated duration of the window. For lower relative velocities, the error can grow to 4–5 seconds, but in this case the observing windows tend to last much more, so it would still be negligible.

3.3 Summary of findings and implications for sensor selection

Summarizing the above results, it is observed that conjuncting objects in LEO consistently perform several close passes before a potential collision. Observation opportunities are enabled by the natural motion of conjuncting objects, which typically make several close passes with decreasing relative distances before the closest approach. Since most LEO objects travel in nearly-circular orbits and with similar orbital periods, conjuncting objects tend to meet twice per orbit before the TCA and at opposite nodal intersections, potentially providing with different observation geometries. A small number (<1%) of conjunctions in LEO involve one object with a marked orbital eccentricity that only passes through this orbital region when close to its perigee. In those cases, observation opportunities are scarce and do not allow for a convenient implementation of the proposed approach.

In terms of relative distances, it was found that in 70% of cases, conjuncting objects in LEO pass within 100 km of each other in the orbits leading up to TCA, and within 300 km in 90% of cases. While these are relatively close distances, their exploitability for observation is limited by the high angular rates at such proximities, which can easily reach several hundred degrees per second. This makes it impossible to

continuously keep the target object within the sensor's FoV. To address this, an upper limit of 1°/s was applied in the calculations to evaluate more realistic portions of the trajectory for observation. The results show that if the onboard sensor has a maximum detection range of 300 km, a significant number of conjuncting objects may either go undetected or only become visible in the final orbits before TCA—during the moments typically predisposed to maneuver execution. A detection range of over 500 km yields better outcomes, as most objects would be visible with sufficient advance time to allow the satellite to respond effectively.

One last considered aspect has been the time available for making observations during each close encounter. The analysis has evidenced that if a payload was able to distinguish any object at a range of 500–600 km, around 90% of the secondaries could be observed for at least 10 s in one of the opportunities available before TCA.

Given that the estimated relative distances range from several hundred to thousands of kilometers, the most feasible option with current technology is optical-based sensors. However, future advancements in LiDAR technology are not out of the question, as several ongoing efforts by space agencies and companies indicate promising potential. For example, as part of its space-based sensor suite for SSA/SDA, Jena Optronik is exploring a LiDAR solution capable of achieving ranges beyond 100 km [28]. Similarly, NASA is developing a LiDAR system about the size of two CubeSat units and weighing approximately 4 kg for estimated ranges above 100 km, although this is intended for asteroid exploration and planetary science missions [29].

Motivated by these advancements, an attempt was made to design a LiDAR system that meets the performance requirements for the considered application, with the full design process detailed in two separate papers, [30] and [31]. However, the results confirmed that it was not feasible to meet all the requirements in a compact form factor. Consequently, only electro-optical sensors are considered for further analysis in this work.

References

[1] D. Spiller, E. Magionami, V. Schiattarella, F. Curti, C. Facchinetti, L. Ansalone, A. Tuozzi, "On-orbit recognition of resident space objects by using star trackers," *Acta Astronautica*, vol. 177, 2020, pp. 478–496, doi: https://doi.org/10.1016/j.actaastro.2020.08.009

[2] L. Felicetti, M.R. Emami, "Image-based attitude maneuvers for space debris tracking," *Aerospace Science and Technology*, vol. 76, 2018, pp. 58-71, doi: https://doi.org/10.1016/j.ast.2018.02.002

[3] A. B. Poore, J. M. Aristoff, J. T. Horwood, R. Armellin, W. T. Cerven, Y. Cheng, C. M. Cox, R. S. Erwin, J. H. Frisbee, M. D. Hejduk, B. A. Jones, P. Di Lizia, D. J. Scheeres, D. A. Vallado, R. Weisman, "Covariance and uncertainty

realism in space surveillance and tracking," Numerica Corporation, Fort Collins, CO, USA, Tech. Rep., 2016

[4] D. Cerutti-Maori, J. Rosebrock, L. Leushacke, H. Krag, "Preliminary concept of a space-based radar for detecting mm-size space debris," in *7th European Conference on Space Debris*, Darmstadt, Germany, 2017

[5] R. Ahmed, N. Majurec, J.W. De Bleser, "A Cubesat-based radar for characterization of millimetric orbital debris," in *The First International Orbital Debris Conference (IOC)*, Sugar Land, TX, USA, Dec. 9–12, 2019

[6] Orbital Debris Research And Development Interagency Working Group, "National orbital debris research and development plan," National Science And Technology Council, Washington, DC, USA, Tech. Rep. 2021. Accessed Oct 22, 2024. [Online]. Available: https://trumpwhitehouse.archives.gov/wp-content/uploads/2021/01/National-Orbital-Debris-RD-Plan-2021.pdf

[7] T. D. Cole, M. T. Boies, A. S. El-Dinary, A. Cheng, M. T. Zuber, D. E. Smith, "The near-earth asteroid rendezvous laser altimeter," *The Near Earth Asteroid Rendezvous Mission*, Springer, Dordrecht, 1997, doi: https://doi.org/10.1007/978-94-011-5200-6_5

[8] D. L. Oltrogge, S. Alfano, D. Berry, J. Cooper, D. A. Vallado, E. Kulu, "Contrasting the inflection points and efforts in space traffic coordination and management," in *10th Annual Space Traffic Management Conference*, Austin, TX, USA, 2024

[9] ESA, "Collision avoidance challenge," Accessed Oct 23, 2024. [Online]. Available: https://kelvins.esa.int/collision-avoidance-challenge/home/

[10] Celestrak's SOCRATES service. Accessed Oct 16, 2023. [Online]. Available: https://celestrak.com/SOCRATES/

[11] G. Campiti, G. Brunetti, V. Braun, E. Di Sciascio, C. Ciminelli, "Orbital kinematics of conjuncting objects in low-earth orbit and opportunities for autonomous observations," *Acta Astronautica*, vol. 208, 2023, pp. 355-366, doi: https://doi.org/10.1016/j.actaastro.2023.04.032

[12] ESA Advanced Concepts Team, "Collision Avoidance Challenge," Accessed Oct 16, 2023. [Online]. Available: https://kelvins.esa.int/collision-avoidance-challenge/data

[13] L. Chen, X. Z. Bai, Y. G. Liang, K. B. Li, "Chapter 4 - Close approach analysis between space object," in *Orbital data applications for space objects*, Springer, Singapore, 2017, ISBN 978-981-10-2962-2

[14] D. A. Vallado, P. Crawford, "SGP4 orbit determination," in *AIAA/AAS Astrodynamics Specialist Conference and Exhibit*, Reston, VA, USA, 2008

[15] R. P. Brent, *Algorithms for Minimization without Derivatives*, Prentice-Hall, Englewood Cliffs, NJ, USA, 1973, ISBN 0-13-022335-2

[16] R. L. Scott, S. Thorsteinson, V. Abbasi, "On-orbit observations of conjuncting space objects prior to the time of closest approach," *Journal of Astronautical Sciences*, vol. 67, no. 4, 2020, pp. 1735–1754, doi: https://doi.org/10.1007/s40295-020-00236-x

[17] V. B. Bastida, T. Flohrer, H. Krag, K. Merz, S. Lemmens, "CREAM — ESA's

Proposal for Collision Risk Estimation and Automated Mitigation," in *First International Orbital Debris Conference*, Houston, TX, USA, 2019

[18] D. A. Vallado, P. Crawford, R. Hujsak, T. S. Kelso, "Revisiting spacetrack report #3," Presented at *AIAA/AAS Astrodynamics Specialist Conference and Exhibit*, Keystone, CO, USA, Aug 21-26, 2006, p. 8. Accessed Oct 16, 2024. [Online]. Available: https://slideplayer.com/slide/2518474/

[19] C. Levit, W. Marshall, "Improved orbit predictions using two-line elements," *Advances in Space Research*, vol. 47, no. 7, pp. 1107-1115, 2011, doi: https://doi.org/10.1016/j.asr.2010.10.017

[20] D. A. Vallado, P. Crawford, R. Hujsak, T. S. Kelso, "Revisiting spacetrack report #3," in *AIAA/AAS Astrodynamics Specialist Conference and Exhibit*, Keystone, CO, USA, Aug 21-26, 2006

[21] P. G. Hartman, "Long-term SGP4 Performance," US Space Command/J3SO, Colorado Springs, CO, USA, Tech. Rep. J3SOM-TN-93-01, 1993

[22] E. Kahr, O. Montenbruck, K. O'Keefe, "Estimation and analysis of two line elements for small satellites," *AIAA Journal of Spacecraft and Rockets*, vol. 50, no. 1, 2013, doi: https://doi.org/10.2514/1.A32352

[23] B. Coffee, R. Bishop, K. Cahoy, "Propagation of CubeSats in LEO using NORAD two line element sets: accuracy and update frequency," in *AIAA Guidance, Navigation, and Control (GNC) Conference*, Boston, MA , USA, Aug 19-22, 2013

[24] F. S. Patt, F. S. Patt, C. M. Hoisington, W. W. Gregg, P. L. Coronado, "SeaWiFS technical report series. Volume 11: analysis of selected orbit propagation models for the SeaWiFS mission," NASA, Greenbelt, MD, USA, Tech. Rep. 104566 (vol. 11), 1993. Accessed Oct 16, 2024. [Online]. Available: https://oceancolor.gsfc.nasa.gov/SeaWiFS/TECH_REPORTS/PreLPDF/PreLVol11.pdf

[25] S. Baghel, D. Mohanty, A. Tamrakar, T. Dewangan, "Accuracy assessment of SGP4 and TLE orbital information," *Mathematical Statistician and Engineering Applications*, vol. 71, no. 4, 2023, pp. 9675-9680, doi: https://doi.org/10.17762/msea.v71i4.1768

[26] J. W. Gangestad, B. S. Hardy, D. Hinkley, "Operations, Orbit Determination, and Formation Control of the AeroCube-4 CubeSats," in *27th Annual AIAA/USU Conference on Small Satellite*, Logan, UT, USA, Aug 10-15, 2013

[27] J. Yang, C. Han, P. Li, K. Ding, "Reliability Analysis of SGP4 Using GOCE Satellite," in *AIAA/AAS Astrodynamics Specialist Conference*, San Diego, CA, USA, 4-7 Aug 2014

[28] Jena Optronik, "Space-based Sensor Suite for Space Situational Awareness and Space Domain Awareness applications," Accessed Oct 23, 2024. [Online]. Available: https://www.jena-optronik.de/products/cameras-and-camera-systems/ssa-sensor-suite.html?file=tl_files/pdf/Conference%20poster%20Sensor%20Suite%20DLRK%202023.pdf.pdf

[29] NASA TechPort, "3D imaging Cubesat LiDAR for asteroid and planetary sciences," Accessed Oct 23, 2024. [Online]. Available: https://techport.nasa.gov/view/33412

[30] G. Campiti, M. Tagliente, G. Brunetti, M. N. Armenise, C. Ciminelli, "Debris detection and tracking through on-board LiDAR", in Berta, R., De Gloria, A. (eds) Applications in Electronics Pervading Industry, Environment and Society. ApplePies 2022. *Lecture Notes in Electrical Engineering*, vol 1036. Springer, Cham., 2023, doi: https://doi.org/10.1007/978-3-031-30333-3_31

[31] M. Tagliente, G. Campiti, G. Brunetti, M. N. Armenise, C. Ciminelli, "Spaceborne LiDAR for debris detection and tracking," in *SIE 2022 – 53rd Annual Meeting of the Associazione Società Italiana di Elettronica*, Pizzo, Italy, September 7-9, 2022

Chapter 4

Detection performance of onboard cameras and star trackers

As established in Chapter 3, electro-opical sensors are the only potentially feasible option for the application under consideration. This also offers the advantage that many LEO satellites are already equipped with optical payloads for scientific purposes, which can be repurposed for SSA with obvious benefits in terms of SWaP. For instance, nearly 600 3U CubeSats launched by PlanetLabs as part of its Earth observation constellations carry a camera [1]. In addition, most active spacecraft features onboard star trackers, whose imaging capabilities could be harnessed for collision avoidance. The repurposing of these devices for uses beyond attitude determination, such as deep-space navigation [2] or SSA [3], has seen growing interest in recent years. A notable example is the Japanese Hayabusa2 probe, which used its onboard star tracker to image the asteroid Ryugu in May 2023 [4].

Nevertheless, small cameras and star trackers generally have limited sensitivity, which becomes even lower when trying to capture fast-moving targets, as the signal is spread across multiple pixel. Additional difficulties related to potentially unfavourable illumination conditions in orbit, and the small size and low reflectivity of debris objects, further impair the feasibility of this approach. To address these aspects, this chapter investigates the detection limits of various optical sensors for space-based observations of conjuncting objects during the lead-up to TCA.

4.1 Models and simulation environment

Emulating space-based observations requires a combination of complex modeling and analytics capabilities, including orbital dynamics, sensors' optics and radiometric responsitivity, geometric calculations of FoV intersections, and space lighting conditions. To address these capabilities, simulations are conducted by interfacing STK, a 3D multi-physics software used for space applications, with Matlab, which offers the necessary automation level.

The block diagram in Fig. 4.1 outlines the procedure for simulating a conjunction scenario where one object, called "primary" and assumed an active satellite with an optical sensor, attempts multiple observations of the other object, called "secondary" and assumed uncooperative, during the pre-TCA time. Four primary steps can be identified: propagation of the objects' trajectories, identification of potential

windows for observations, simulation of the space-based measurements through EOIR, and image processing. Importantly, to plan and conduct autonomous real-world operations, the primary must know both its own and the secondary's orbital state, as well as autonomous processing capabilities to perform orbit propagation, visibility interval calculations, and conjunction assessments. Self-position awareness is assumed to be achieved through an onboard GNSS receiver, whereas initial positional information on the secondary object is considered to be uplinked from the ground during the days prior to TCA.

The next subsections further detail the building blocks in Fig. 4.1.

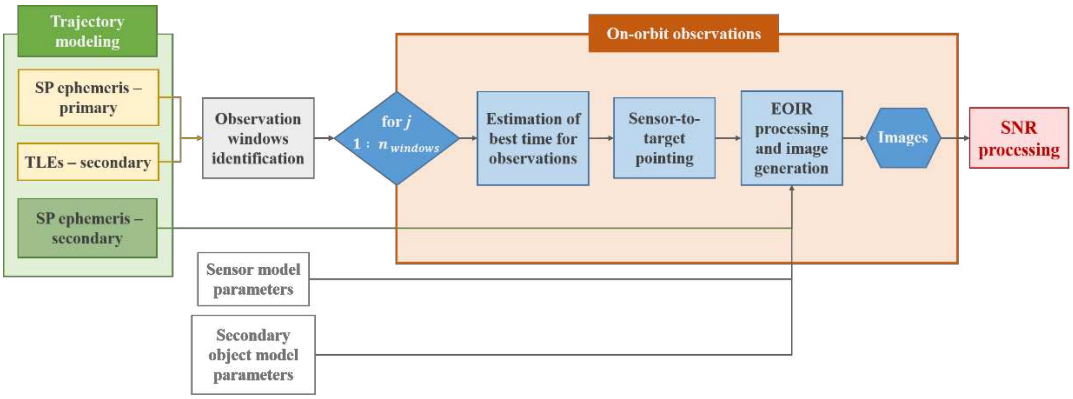

Fig. 4.1 Overview of the steps for simulating a conjunction scenario and analyzing the outcomes. "SP" stands for Special Perturbation and "TLE" refers to Two-Line Elements

4.1.1 Trajectory modeling

Conjunction scenarios are generated once again starting from data on real-world events retrieved from Celestrak's SOCRATES online service. All selected events involve one active satellite and an inactive object, assumed respectively as the primary and secondary for the simulations. Moreover, only high-risk conjunctions with predicted miss-distances lower than 1 km have been retained, ultimately resulting in a database of 180 events. The objects' trajectories are modeled on STK over the one-day interval leading to TCA and starting from Special Perturbation (SP) ephemeris. The SP ephemeris, generated by the U.S. 18th SDS [5], is a highly accurate resource of orbital information relied upon by many space agencies and operators, including NASA, for making collision avoidance decisions. While such ephemeris are used in the simulations to model the "true" objects' trajectories, a primary satellite realistically does not have accurate knowledge of the secondary's state for predicting observation windows. For this reason, TLEs, which offer lower accuray compared to SP data, are also obtained for the secondary objects and considered the information source available to the primary for the onboard analyses. Instead, as depicted in Fig. 4.1, ephemeris associated with the primary objects serve as both the trajectory reference and the onboard data, given that GNSS receivers in LEO achieve meter-level accuracy, providing satellites with very good knowledge of their state.

4.1.2 Observation windows identification

Observation windows are determined by first calculating the time intervals in which unobstructed view is available between objects, then applying some constraints. These include a minimum solar exclusion angle of 40 deg, to prevent sunlight

interference, the requirement for the secondary object to be sunlit, and a minimum elevation angle of the secondary object above the Earth's limb, to avoid atmosphere interference. The elevation angle is computed such that the scene within the sensor's FoV is at least 18 deg above the horizon, since typical earthlight exclusion angles for star trackers range between 15–20 degrees [6]. A lunar exlusion angle was not considered, as most modern star trackers are capable of operating with full Moon inside the FoV. Because CAMs in LEO are typically executed no later than half an orbit before TCA, observation opportunities within the last 40 minutes prior to the event are discarded, which is just under half a revolution in LEO.

4.1.3 Observation strategy

For each identified window, the simulation mimics the primary capturing images of the secondary. A sidereal strategy is considered, whereby the primary points the sensor towards the expected secondary location and acquires images while keeping a fixed orientation relative to the stars. Thus, the object is imaged as it moves across the FoV, until it exits the frame. Since relative distances during the encounters are in the order of hundreds of kilometers, secondaries appear almost as point sources from the primary's perspective, leaving streaks in the images against fixed stellar backgrounds. An alternative observation strategy would be to adjust the sensor's orientation in real time to track the secondary movement, keeping it centered in the FoV. This potentially yields clearer images, as the target maintains a consistent position within the camera's pixels throughout the exposure, thereby resulting in an increased SNR. However, this approach requires accurate trajectory knowledge as well as remarkable attitude control capabilities, which are overly optimistic conditions to assume for generic scenarios. A sidereal strategy is more feasible, besides reflecting the standard operational mode of star trackers.

Before an observation opportunity, the primary calculates the optimal direction for sensor pointing by first identifying the time within the window expected to yield the maximum SNR, denoted as t_{opt}. This is done by solving a maximization problem based on an approximated analytical model of the SNR for sidereal detection, as detailed later. Maximizing the SNR is fundamental for this application, given the inherent dimness of the detected targets. Once t_{opt} is estimated, the sensor's boresight is oriented towards the predicted position of the secondary at that time. As motivated below, the implemented observation strategy results in images featuring very short streaks – roughly 1-3 pixels long – associated with detected secondaries. One challenge in analzying low-SNR images featuring short streaks is the difficulty to distinguish targets from highly noisy pixels. This midentification issue can be mitigated through the acquisition and correlation of multiple sequential images of the target. As shown in Fig 4.2, repeatedly imaging a moving object will reveal its trajectory as a sequence of aligned streaks, which are unlikely to result from random noise. For this reason, the primary acquires multiple images every second over a time interval around t_{opt}, when the secondary is expected to be within the FoV.

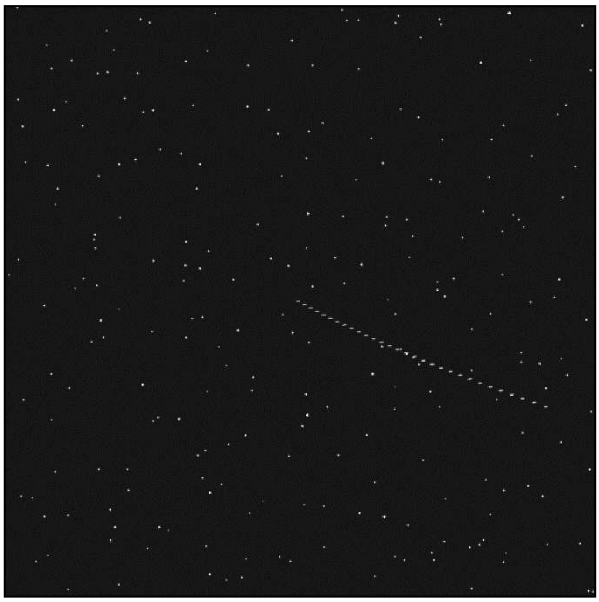

Fig. 4.2 Composite image obtained by superimposing successive captures of a transiting object, revealing its trajectory as a sequence of aligned dots

4.1.3.1 Onboard SNR model and calculation of t_{opt} and τ_{opt}

According to [7], the signal from a target observed at time t can be expressed in number of photoelectrons per second as:

$$\dot{S}_e(t) = F_0 10^{-0.4 m_v(t)} \cdot T \cdot A_{\text{eff}} \cdot QE \tag{4.1}$$

where F_0 (photons/m²s) is the flux of a zero-magnitude object, $m_v(t)$ (adimensional) is the apparent visual magnitude of the target, T (adimensional) is the transmittance of the optical system, A_{eff} (m²) is the effective aperture area of the sensor, and QE (adimensional) is the detector quantum efficiency. The apparent magnitude is given by:

$$m_v(t) = -26.8 - 2.5 \log_{10}\left(\frac{\mu A F(\phi(t))}{\|\boldsymbol{r}_{\text{rel}}(t)\|^2}\right) \tag{4.2}$$

where μ (adimensional) is the target's reflectance (or superficial albedo), A (m²) is its cross-sectional area, $\|\boldsymbol{r}_{\text{rel}}(t)\|$ (m) is the primary-to-secondary distance, and $F(\Phi(t))$ (adimensional) is the solar phase angle function. The target body is assumed as a sphere with diffuse reflection behavior – also known as Lambertian sphere – and with uniform surface material, as done in [8]. With these assumptions, $F(\Phi(t))$ can be expressed as:

$$F(\phi(t)) = \frac{2}{3\pi^2}\left((\pi - \phi(t))\cos\phi(t) + \sin\phi(t)\right) \tag{4.3}$$

where $\Phi(t)$ (rad) is the solar phase angle formed between the Sun and the primary with respect to the secondary. This model is solely used for simulating the primary's estimation of peak SNR times. More accurate models are employed within EOIR for simulating the entire detection process, including the targets' brightness characteristics and the sensors' acquisition capabilities, as detailed in Section 4.1.4.

For a given observation time t and exposure time τ, the target's signal will spread onto a number of pixels p, given by:

$$p(t,\tau) = \omega(t) \cdot \frac{\tau}{IFOV} \tag{4.4}$$

where *IFOV* (rad) is the pixel's instantaneous horizontal or vertical FoV, which are usually equal in common detectors, and $\omega(t)$ (rad/s) is the target's instantaneous angular rate in the focal plane. Then, the estimated signal $S_e(t, \tau)$ in each streak pixel can be expressed in number of photoelectrons as:

$$S_e(t,\tau) = \begin{cases} \dot{S}_e(t)\tau\sqrt{k_f}, & p(t,\tau) \leq 1 \\ \dfrac{\dot{S}_e(t)\tau\sqrt{k_f}}{p(t,\tau)}, & p(t,\tau) > 1 \end{cases} \tag{4.5}$$

where k_f (adimensional) is known as the "straddle factor", defined as the fraction of signal expected to fall on the most illuminated pixel [7]. This factor takes into account the realistic distribution of light from a target across the sensor's pixels. When an imaging system captures a point source that is perfectly centered on a pixel, it creates a blurred spot of a certain size. However, as point sources are generally not exactly pixel-centered, causing the blurred spot to overlap multiple pixels, k_f is used to quantify the fraction of blur energy expected to fall within the brightest pixel. Its value is statistically calculated assuming that the source may be located anywhere within a pixel area, and it typically ranges between 0.4–0.5 [9]. Equation (4.5) essentially reflects the fact that, in sidereal mode, the signal increases proportionally with τ as long as it lands on the same pixel. Then, once the streak exceeds one pixel ($p > 1$), the signal stops increasing and reaches a maximum, as can be inferred by merging Eqs. (2) and (3).

The overall noise figure N is modeled as:

$$N(\tau) = \sqrt{B \cdot \tau + \sigma_{rn} + \sigma_{dc} \cdot \tau} \tag{4.6}$$

where B (e^-/s) is the background sky photoelectron production rate, σ_{rn} (e^-)is the variance of the read noise, and σ_{dc} (e^-/s) is the variance of the dark current. The parameter B is due to the background sky radiance [7], which accounts for contributions from skyglow, airglow, zodiacal light, scattered light, and atmospheric conditions. This is mainly significant for ground-to-space observations, so it is neglected here.

Concerning τ, it is assumed that the onboard sensor is capable of configuring it internally across a defined range, a common feature of detectors found in modern star trackers. For sidereal imaging of point sources, an optimal exposure time $\tau_{opt}(t)$ exists at each observation instant t that maximizes the SNR, corresponding to the time taken by the target to traverse one pixel. This can be intuitively verified by considering how the expected SNR, given by the ratio between S_e and N, evolves with increasing exposure time. In fact, as long as the photons from a target accumulate on the same pixel during an exposure (i.e., $p \leq 1$), S_e increases faster than N, growing proportionally to the square root of τ. Once the object "moves" to the next pixel (i.e., $p > 1$), the signal on the first pixel stops increasing while the background noise continues to grow, reducing the overall SNR. Therefore, $\tau_{opt}(t)$ can be expressed as:

$$\tau_{opt}(t) = \frac{IFOV}{\omega(t)} \tag{4.7}$$

Since calculating $\tau_{opt}(t)$ requires knowledge of ω, adopting this strategy is feasible when a priori trajectory information is available for the intended targets, as in the present application. For all other cases, such as for ground-based detection of uncataloged objects, τ must be adjusted based on several factors, including the specific orbital regime targeted (e.g., LEO, GEO, etc.), which affects the expected angular rates of the objects, and constraints related to the detection algorithm used in post-processing.

One practical challenge with using $\tau_{opt}(t)$ is that the streak produced by a target during an exposure, which is one pixel long, is very unlikely to be confined to a single pixel. Instead, photons will spread unevenly across adjacent pixels, as depicted in illustration of Fig. 4.3(b). Moreover, when the object's trajectory is very inclined to the focal plane's principal axes, the streak may extend across three pixels. Consequently, this phenomenon reduces the resulting SNR compared to the ideal scenario illustrated in Fig. 4.3(a). For this reason, an exposure time of $2\tau_{opt}(t)$ has been selected. Moreover, the sensor is always oriented such that one of the focal plane's axes aligns with the expected direction of motion of the secondary. This strategy inevitably introduces more noise, but ensures that the target traverses at least one full pixel during the acquisition, which overall leads to a higher SNR on average.

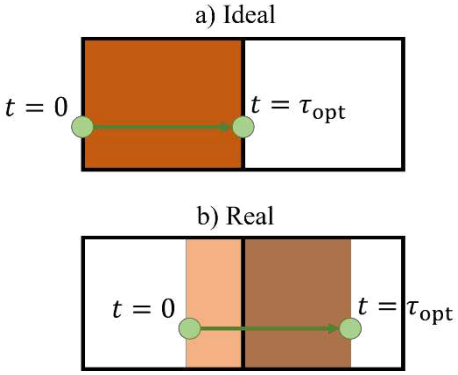

Fig. 4.3 Ideal (a) and realistic (b) target's signal distribution over two pixels having used an exposure time of τ_{opt}

Substituting $2\tau_{opt}(t)$ in Eqs. (4.5), (4.6), and by using Eq. (4.7) to explicit $\tau_{opt}(t)$, the SNR can be conveniently expressed as function of t only:

$$SNR(t) = \frac{S_e\left(t, 2\tau_{opt}(t)\right)}{N\left(2\tau_{opt}(t)\right)} =$$

$$= \frac{F_0 10^{-0.4\left[-26.8-2.5\log_{10}\left(\frac{\mu AF(\phi(t))}{\|\boldsymbol{r}_{\text{rel}}(t)\|^2}\right)\right]} \cdot T \cdot A_{\text{eff}} \cdot QE \cdot \frac{IFOV}{\omega(t)}}{\sqrt{\sigma_{rn} + \sigma_{dc} \cdot 2\frac{IFOV}{\omega(t)}}} \tag{4.8}$$

Therefore, to estimate the best time $t_{opt}(t)$, the primary can minimize the above expression of $SNR(t)$ across each observation interval. Since the time-invariant factors in Eq. (4.8) do not influence the minimization, the problem can be reduced

to:

$$t_{opt} = \arg\max_{t\epsilon\Delta t}(SNR(t)) = \frac{\frac{\|\boldsymbol{r}_{\mathrm{rel}}(t)\|^2}{F(\phi(t))\cdot\omega(t)}}{\sqrt{2\frac{IFOV}{\omega(t)}\sigma_{dc}+\sigma_{rn}}} \tag{4.9}$$

where Δt denotes a specific observation interval. The values of $\boldsymbol{r}_{\mathrm{rel}}(t)$ and $F(\Phi(t))$ are derived through basic geometric calculations based on the available TLE-knowledge of the secondaries. The angular rate $\omega(t)$ is obtained in two steps: first, the angular position of the secondary is calculated at times $t \pm \varepsilon$ with respect to an ICRF frame fixed on the primary's body, where ε is a small value such as 10^{-6} s, then a center differencing method is used, obtaining the angular rate as the numerical derivative of the angular position. The remaining parameters (i.e., $IFOV$, ω, σ_{rn}, σ_{dc}) are related to sensor attributes, for which the nominal values specific to the sensor being modeled are used, since they are varied across simulations.

4.1.4 EOIR processing and image generation

Starting from the modeled STK scenario, EOIR simulates what the onboard sensor sees at each instant and provide resulting digitized image outputs. This process involves several advanced modeling capabilities, such as the simulation of optical and thermal properties of targets, as well as the sensor's radiometric response. A comprehensive overview of these capabilities and the underlying processes of EOIR is provided in the Appendix A.

4.1.4.1 Image post-processing and SNR calculation

After simulating sensor's response to generated scenes, two types of outputs can be retrieved: an ASCII raw data file (.txt) or a bitmap file (.bmp). The former is a space-delimited text file containing the number of electrons for each pixel, while the latter represents a synthetic image created by further simulating the A/D conversion process. This entails a quantization step in which electrons numbers are converted into discrete digital levels based on the specified bit depth.

Fig. 4.4 displays a magnified bitmap image and Fig. 4.5 shows its corresponding pixel values extracted from the image through Matlab. Within the image, a few stars can be identified alongside a streak created by a detected object. To enhance interpretability, the pixel matrix has been imported into Excel, with cells color-coded according to their pixel values.

The images are post-processed to determine the SNR of the detected secondary objects. The SNR is a critical metric for assessing the quality and overall performance of electronic measurement systems. An SNR threshold is typically utilized to decide whether a target has been detected, the specific value of which may be selected differently depending on the application. To identify the target in each image, several detection algorithms could be employed. These can often be tailored to take advantage of specific image characteristics inherent to the considered application, thereby enhancing the SNR or reducing the necessary threshold for reliable detection. When some a priori knowledge is available on the target's trajectory, such as in the present application, techniques such as matched filter can be leveraged to focus the analysis on limited areas where the target is likely to appear. However, the

focus of this chapter is on evaluating the detection capabilities of various sensor systems regardless of the specific algorithms used for image post-processing, which will be explored in a future research. Therefore, as part of the image-processing steps, target detection is done here by partially exploiting inherent capabilities of EOIR, as outlined in the flowchart presented in Fig. 4.6.

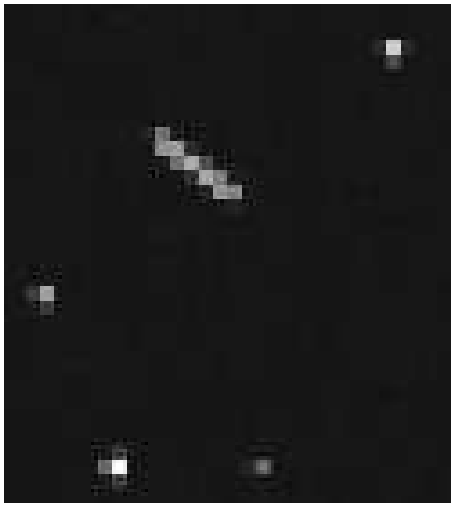

Fig. 4.4 Magnified bitmap image displaying four stars and a streak associated with a moving object.

21	22	22	22	21	22	22	22	20	23	22	22	21	23	23	22	23	21	23	23	22	22	21	23	22	22	22	23	22	25
21	22	23	22	24	22	22	23	24	22	24	23	22	21	22	23	23	23	22	21	22	22	22	22	22	22	41	205	40	21	23
23	22	23	20	20	23	23	21	21	22	19	24	22	23	22	23	22	22	22	22	22	21	22	22	22	22	21	73	26	23	22
23	23	23	21	22	22	23	21	21	21	22	22	24	23	22	23	23	23	22	21	21	22	23	22	22	22	22	21	21	22	24
22	23	23	23	23	21	22	22	22	22	23	22	21	24	22	23	22	22	22	21	22	22	23	21	24	23	22	22	22	23	23
22	22	21	22	22	22	21	23	22	22	22	24	21	23	22	24	22	23	22	22	21	21	23	24	23	20	23	22	23	24	22
22	22	23	23	21	21	22	22	22	23	19	22	23	22	23	21	24	22	21	22	22	21	22	22	22	23	22	23	22	24	22
22	23	23	22	23	23	22	23	22	23	33	111	31	20	23	22	22	23	22	20	23	22	22	23	23	23	22	22	23	23	22
21	22	24	22	23	21	23	23	24	23	25	141	155	41	23	20	24	22	23	22	23	22	21	23	22	22	23	22	22	21	22
22	21	22	22	23	22	24	20	23	22	22	27	110	168	79	25	21	22	21	23	22	22	22	22	23	22	23	22	23	22	23
22	23	23	23	21	21	23	20	23	23	20	21	22	50	164	126	31	24	22	23	23	22	23	22	23	23	23	23	22	22	22
23	21	23	21	23	23	22	23	21	23	20	23	23	21	34	146	130	26	22	20	22	21	22	23	19	22	20	22	22	24	22
21	23	24	22	23	22	22	22	23	23	22	21	21	22	22	27	33	23	23	22	23	22	21	23	22	23	22	24	24	22	23
23	21	22	22	23	23	23	22	22	22	22	22	22	24	23	23	22	21	22	22	22	22	22	23	22	22	22	19	21	21	22
22	23	22	22	23	23	22	20	21	20	23	24	23	22	23	21	23	23	22	24	23	23	21	22	21	22	22	22	21	24	23
22	23	22	22	22	23	22	23	22	23	20	21	23	21	23	22	22	21	22	23	22	22	21	22	23	20	24	22	21	22	21	23
23	22	22	23	23	20	22	21	23	22	22	23	23	21	22	20	23	22	22	22	23	22	23	22	23	22	23	21	22	24	23
22	23	21	24	22	22	23	22	22	23	23	22	22	23	23	22	23	21	22	23	21	22	21	23	22	23	22	22	23	23	23
23	23	57	159	24	22	23	21	22	20	21	22	23	19	22	21	23	24	21	20	23	21	20	21	22	21	22	22	22	23	22
22	21	26	57	21	22	22	22	22	22	21	21	22	20	22	22	22	22	21	24	23	22	22	23	23	24	22	23	22	23	23
21	21	21	24	22	23	22	22	22	22	23	22	22	22	22	23	23	23	21	23	20	24	21	22	23	22	23	21	22	23	22
20	22	22	22	23	24	23	23	23	21	23	24	23	21	23	22	22	23	21	22	22	22	19	23	23	23	22	23	23	22	23
22	22	22	22	22	23	21	20	23	22	22	22	22	23	22	22	21	22	22	22	21	22	22	22	22	23	23	23	23	21	23
21	22	23	23	22	24	23	23	22	23	23	22	23	22	23	21	24	22	23	20	22	23	21	21	24	22	22	22	24	22	23
23	22	22	21	22	19	23	22	22	22	23	21	21	23	23	22	22	22	23	24	22	22	23	23	22	22	23	23	24	22	20
23	23	23	23	22	22	23	24	23	23	23	23	22	22	22	23	21	22	21	21	22	21	22	24	23	23	20	20	22	22	22
20	23	23	23	23	22	21	24	23	22	22	20	22	22	22	21	22	22	23	21	22	23	22	22	22	22	21	22	24	22	22
22	21	21	21	22	23	22	21	21	22	21	22	22	21	22	23	21	21	23	22	22	21	21	24	22	22	23	24	22	22	22
22	20	22	21	20	22	23	22	22	22	21	22	22	22	23	22	23	21	24	22	23	23	23	22	21	22	23	22	22	22	22
22	22	23	21	24	22	22	27	58	24	21	23	22	22	22	24	24	23	25	23	23	21	23	23	23	22	22	23	23	23	
21	22	23	23	21	22	22	106	255	21	21	23	23	22	22	21	22	38	106	22	20	22	23	23	22	21	22	21	23	22	21
22	22	23	22	21	23	22	26	57	22	23	23	24	21	23	21	22	23	25	22	20	22	20	22	22	21	22	23	23	21	20
22	21	21	22	22	23	23	20	23	23	23	22	22	23	23	22	21	23	24	22	22	23	23	20	22	22	22	23	21	22	21

Fig. 4.5 Pixel values for the same scene of Fig. 4.4, as read through Matlab

Using the STK's graphical user interface, a user can click on individual pixels and view details about the objects they contain, such as stars or targets. However, this kind of metadata cannot be retrieved through external scripts, and manually extracting it for each image is impractical due to the high number of simulations. To address this, an intricate yet effective approach is employed that allows identifying all pixels geometrically crossed by the target. For each image generated during the simulations, a second image of the same scene is generated by removing stars and all noise sources from the scenario. Under these conditions, all detector outputs will be attributable to detected secondary objects, resulting in pixel matrices filled with

zeros except for a few values associated with the pixels crossed by the objects, as illustrated in Fig. 4.6. Note that these pixels are those geometrically crossed by the target, but the digital values for some of them could be comparable to the noise level in the original image. The sole purpose of generating the second image is to identify a "Region of Interest" (RoI) within the first image. The RoI is taken from the second image as the smallest matrix encompassing non-zero values, with with zero-valued pixels at the periphery, as shown in Fig. 4.6.

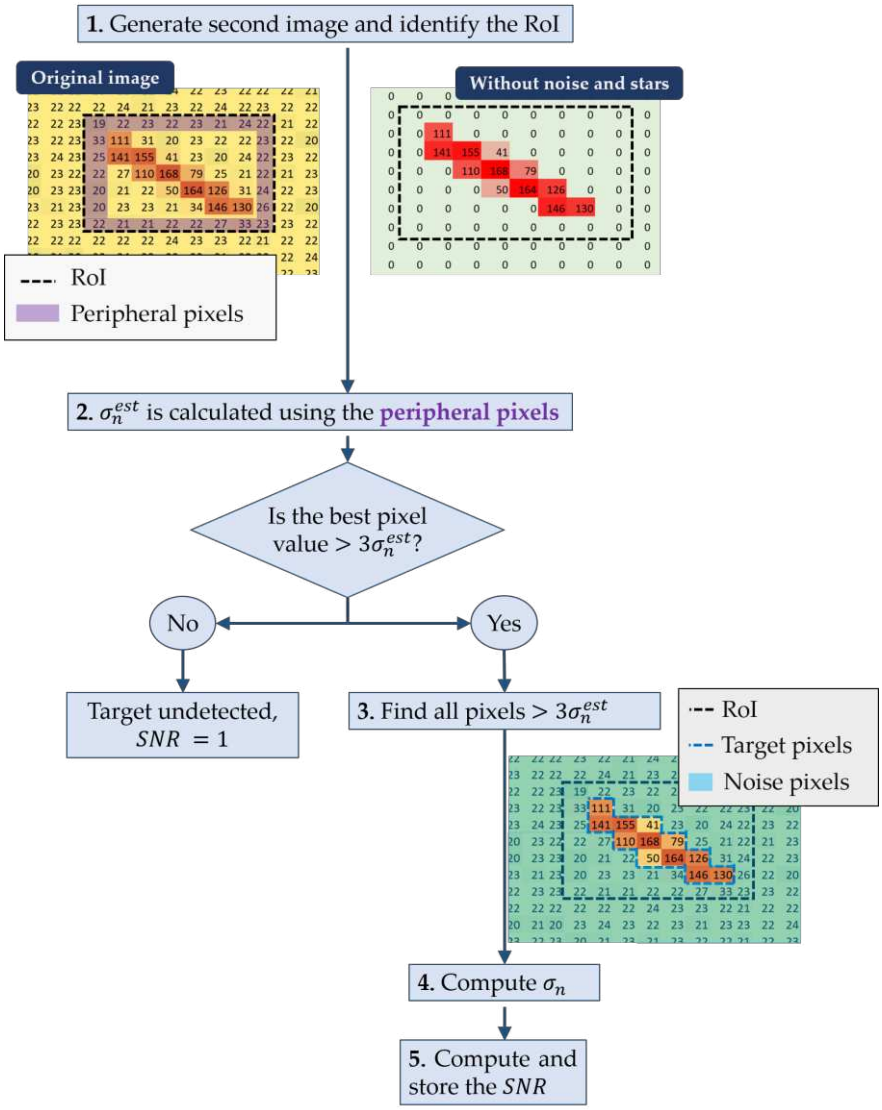

Fig. 4.6. Flowchart of the image-processing steps

Since the peripheral pixels are necessarily associated with the background in the original image, their values are used to compute an initial estimate of the noise standard deviation σ_n, denoted with σ_n^{est}. Then, if the highest pixel value within the RoI is lower than $3\sigma_n^{est}$ the target is considered undetected and the SNR is assigned a value of 1. Otherwise, a region-growing algorithm is utilized to identify all pixels exceeding $3\sigma_n^{est}$ and connected to the best pixel. The remaining pixels within the RoI, denoted in Fig. 4.6 as "noise pixels," are used to calculate a better estimate of σ_n^{est}. Finally, the SNR is taken as the ratio between the best pixel value and σ_n.

Note that, because EOIR's scene generation utilizes stochastic processes to model

sensor's noise, the outcome of the steps in Fig. 4.6 is not deterministic. Therefore, if a same scene is generated multiple times, the resulting SNR may slightly vary. To mitigate variability and avoid outliers, each image is generated three times and the SNR taken as the average from the three runs.

4.2. Simulation parameters

As mentioned in Section 4.1.4, data on 180 events have been collected. These events are simulated multiple times by varying the parameters of both the onboard sensor model and the secondary object.

4.2.1 Onboard sensor

Despite the broad range of parameters available in EOIR for modeling the onboard sensor, preliminary simulations have shown that few of them account for most variability in the detection performance. These include the optical aperture D_A, FoV, quantum efficiency QE, fill factor FF, exposure time τ, readout noise σ_{rn}, and dark current noise σ_{dc}. For this reason, only these parameters are varied across the different modeled sensors, keeping all the others at standard values.

The selection of parameter values has been primarily concerned with typical star tracker specifications. This stems from the consideration that primary payload cameras and telescopes usually offer higher performance, making it more relevant to clarify the detection capabilities of star trackers, which is particularly interesting given that they are also standard equipment on spacecraft. A market survey has been conducted to identify common specifications for star trackers, with the findings collected in Tables 4.1 and 4.2. Table 4.1 reports the selected devices and provides information on the manufacturer, optical aperture D_A, dimensions, FoV, detector name, power requirements, and weight. Where D_A is not available, device dimensions can only be taken as indicative of it. For instance, advanced star trackers such as Jena Optronik's Astro-XP feature catoptric optics, which typically involve an arrangement of mirrors to fold the optical path. In these cases, the effective focal length exceeds physical dimensions of the sensor. Meanwhile, Table 4.2 provides the range of parameters for the detectors listed in Table 4.1 and for those of similar devices used in spacecraft applications. Detectors such as FaintStar2, CMV4000, and HAS-2, are utilized on common spacecraft imaging systems [8].

Table 4.1 Characteristics of different commercial star trackers. "OH" and "EU" denote "Optical Head" and "Electronic Unit", respectively.

Device name	Manufacturer	D_A [mm]	x-y-z dimensions [mm]	FoV [deg]	Detector	Power [W]	Weight [g]	Ref.
T1	Terma	26	92×92×68 (OH) 100×100×40 (EU)	20×20	Faintstar2	0.8 (OH) 2.5 (EU)	313 (OH) 450 (EU)	[10], [11]
T2	Terma	26	92×92×68 (OH) 100×100×40 (EU)	20×20	–	0.8 (OH) 2.5 (EU)	313 (OH) 450 (EU)	[10, [11]

STAR-T3	Terma and Space Inventor	18	60×60×100 (incl. baffle)	20×20	–	2	350	[12]
HE-5AS	Terma	20 (*f*/1.6)		21.6×21.6		1.5	1000	[13]
Auriga CP	Sodern	–	66×59×94	–	–	0.8–1.1	225	[14]
HYDRA M	Sodern	–	147×147×283 (OH) 171×156×65 (EU, incl. baffle)	–	HAS-2 detector	–	1400 (OH) 1400 (EU)	[15]
HORUS	Sodern	–	141×141×250 (OH)	–	FaintStar2	9.5 – 14	1600 (OH)	[16]
A-STR	Leonardo	–	195×175×290.5	16.4x16.4	–	8.9 @20°C 13.5 @60°C	3550	[17]
AA-STR	Leonardo	–	164×156×348	20×20	HAS2	5.6 @20°C 12.6 @60°C	2600	[17]
Astro APS	Jena Optronik	36 (*f*/1.2)	–	20×20	HAS2 or STAR1000	5-12	2000	[18]
Astro APS3	Jena Optronik	–	137×137×213	20×20	FaintStar2	< 8	< 1800	[19]
Astro-CL	Jena Optronik	–	60×60×110	25×25	–	< 1	< 305	[20]
Astro-XP	Jena Optronik	85 (*f*/2)	–	3.3×3.3	Faintstar2	< 1 (OH) < 10 (EU)	–	[21]
MicroASC	DTU	8 (*f*/4)	–	13.7×18.3	–	1.9	425	[22], [23], [24]
ST-16RT2	Rocket Lab	16 (*f*/1.6)	–	15×20	–	0.5 (avg)–1 (peak)	158 (excl. baffle)	[25]
HAST	Ball Aerospace	110 (*f*/2)	–	8.8×8.8	–	–	–	[26], [27]
Standard NST	Blue Canyon Technologies	–	55×50×100	10×12	–	< 1.5 @5V	350	[28]
Redwire Star Tracker	Redwire	22 (*f*/0.77)	–	19×14	–	2	475	[29]
Arcsec	Sagitta	–	44×50×95	25.4×25.4	–	1.5	270	[30]
CT-2020	Ball Aerospace	34	–	10×10	–	< 8 (avg), 12 (peak)	3400	[31]

Star trackers generally feature small apertures and wide FoV. Typical apertures range from 2 to 5 cm, although devices designed for medium-to-large satellites can reach up to 11 cm. The FoV generally spans between 15 and 20 deg, driven by the requirement to achieve extensive sky coverage for effective stars identification.

Based on the survey, 25 different sensors have been conceived and modeled. Table 4.3 details the parameters that are varied across these sensors, while Table 4.4 lists those that are mantained constant. Sensors #1 to #24 reflect the range of star trackers and small cameras typically mounted on satellites, while sensor #25 more properly mirrors the characteristics of a larger telescope. This sensor's radiometric properties are modeled after NEOSSat's payload detector [38], [39], boasting a sensitivity of 0.78 and a readout noise of 2e^- Root Mean Square (RMS).

Table 4.2 Characteristics of different different detectors used in commercial star trackers and image sensors. *S* indicates the sensitivity, calculated as the product between *QE* and *FF*, while FWC stands for Full Well Capacity.

Detector	**Technology**	**Pixel grid**	σ_{rn} [e^-]	σ_{dc} [e^-/s]	τ [ms]	*S* [-]	*FWC* [ke^-]	**ADC resolution [bit]**	**Ref.**
FaintStar2	CMOS	1024×1024	21	25	–	0.55	108	11 or 12	[32]
CMV4000	CMOS	2048×2048	–	125	*	0.6	–	–	[33]
HAS2	CMOS	1024×1024	–	–	–	0.45	–	–	[34]
Detector from MicroASC star tracker	CCD	752×580	19	2	–	–	4.366	8	[22], [23]
Detector from HE-5AS star tracker	CCD	1024x1024	30	< 50 (avg.)	–	–	–	8	[13]
Detector from ST-16RT2 star tracker	CMOS	2592×1944	3	–	–	–	–	–	[25]
Detector from CT-2020 star tracker	CMOS	1024×1024	–	–	10 – 98*	– (*QE*=0.9)	–	–	[31], [35], [36]
ESA's Cryosat-2 star tracker detector	–	1024×1024	40	–	300*	–	–	8	[37]
ESA's Sentinel 2A and 2B star tracker detector	–	1020×1020	35	–	1	–	–	–	[37]
ESA's Sentinel-5p star tracker detector	–	600×699	–	–	1– 8000*	–	–	8	[37]

*configurable integration time

Table 4.3 Characteristics of the modeled onboard sensors.

#	D_A [cm]	S [–]	FoV [deg]	σ_{rn} [e^-]	σ_{dc} [e^-/s]
1	2	0.5	10×10	30	80
2	2	0.5	15×15	30	80
3	2	0.5	20×20	30	80
4	2	0.6	10×10	8	30
5	2	0.6	15×15	8	30
6	2	0.6	20×20	8	30
7	5	0.5	10×10	30	80
8	5	0.5	15×15	30	80
9	5	0.5	20×20	30	80
10	5	0.6	10×10	8	30
11	5	0.6	15×15	8	30
12	5	0.6	20×20	8	30
13	7.5	0.5	10×10	30	80
14	7.5	0.5	15×15	30	80
15	7.5	0.5	20×20	30	80
16	7.5	0.6	10×10	8	30
17	7.5	0.6	15×15	8	30
18	7.5	0.6	20×20	8	30
19	10	0.5	10×10	30	80
20	10	0.5	15×15	30	80
21	10	0.5	20×20	30	80
22	10	0.6	10×10	8	30
23	10	0.6	15×15	8	30
24	10	0.6	20×20	8	30
25	15	0.8	10×10	3	25

Table 4.4 Fixed sensor parameters.

Parameter	Value
Bit depth	8 bit
τ	10 – 500 ms (configurable)
FWC	80,000 e^-
Line-of-sight jitter	0.05 mrad
T	0.9
Detector grid	1024×1024
RMS wavefront error	0.07

Regarding the parameters in Table 4.4, the chosen RMS wavefront error represents moderate aberrations [40], while a jitter of 0.05 mrad corresponds to average pointing requirements [41]. Most surveyed detectors utilize a 1024×1024 pixel grid, although some, especially those used in higher performance imaging systems, have a larger pixel count. A finer grid means that transiting objects spend less time in each pixel, resulting in higher resolution but lower SNR. However, since EOIR currently supports a maximum grid size of 1024×1024 pixels, this parameter is herein kept constant across all sensors.

4.2.2 Secondary object parameters

Real-world secondary objects display a wide variety of shapes and sizes, from small irregular debris fragments to large defunct spacecraft. For this reason, here they are modeled through EOIR as spheres with uniform surface material, varying their diameter D and surface reflectivity μ (or superficial albedo) across simulations. Specifically, for each conjunction event and sensor model, 15 different simulations are conducted by varying D and μ using all combinations of values outlined in Table 4.5. The lower diameter end roughly corresponds to the current minimum detectable size from ground-based systems [42], while the higher end is representative of the large-class payloads, although larger objects are present in orbit. As for the reflectivity, accurate modeling is challenging due to the variety of materials used in satellites and debris, each with unique wavelength-dependent reflectance properties. Tumbling motions, particularly prevalent in debris objects, cause additional variations in the overall reflectance spectrum over time. For these reasons, the reflectance is usually modeled using statistically representative values derived from empirical measurements. For fragmentation debris, a global albedo of 0.175 was recommended in 2007 by NASA's Johnson Space Center [43], a revised value from the 1990s estimates of 0.09-0.12 [44]. Although a value of 0.175 is currently the most widely accepted, further experiments by the same scientists have highlighted the need for additional studies to establish a more precise and reliable value [45]. For non-fragmentation objects, such as intact rocket bodies and mission-related objects, the smoothness of their unimpacted surfaces typically results in a higher average reflectance. A value of 0.2 is generally utilized in literature [46], although higher values are possible depending on the specific coatings of the object. Materials such as white and gold paints, found on surfaces of the Titan 3C Transtage [47], can exhibit reflectances approaching the unity. The three values of μ listed in Table 4.5 aim to capture the distribution of reflectance characteristics observed in LEO, from the dimness of fragmentation debris to the higher reflectivity of intact objects.

Table 4.5 Secondary objects parameters.

Parameter	Values
D	10, 20, 40, 100, 200 cm
μ	0.13, 0.175, 0.21

The outcome of each simulated conjunction is a list of SNR values, each reflecting how well the secondary could be seen by the primary during one of the

observation windows.

4.3 Results and discussion

First analyzed features include the visibility conditions in orbit and the timing of observations. In approximately 50% of cases, conjuncting objects have one visibility window per orbit at the same orbital location, with favorable conditions—meaning the secondary object is sunlit, and the viewing geometry includes an adequate Sun exclusion angle and sufficient elevation above the Earth's limb. Of the remaining cases, around 48.8% show two observation opportunities per orbit at roughly opposite orbital nodes, while about 1% of cases present no viable observation opportunities. Figure 4.7 illustrates the timing of visibility windows in the two days prior to the TCA for 23 random conjunctions from the database, highlighting, with horizontal shaded bands, those conjunctions for which two visibility windows per orbit are available.

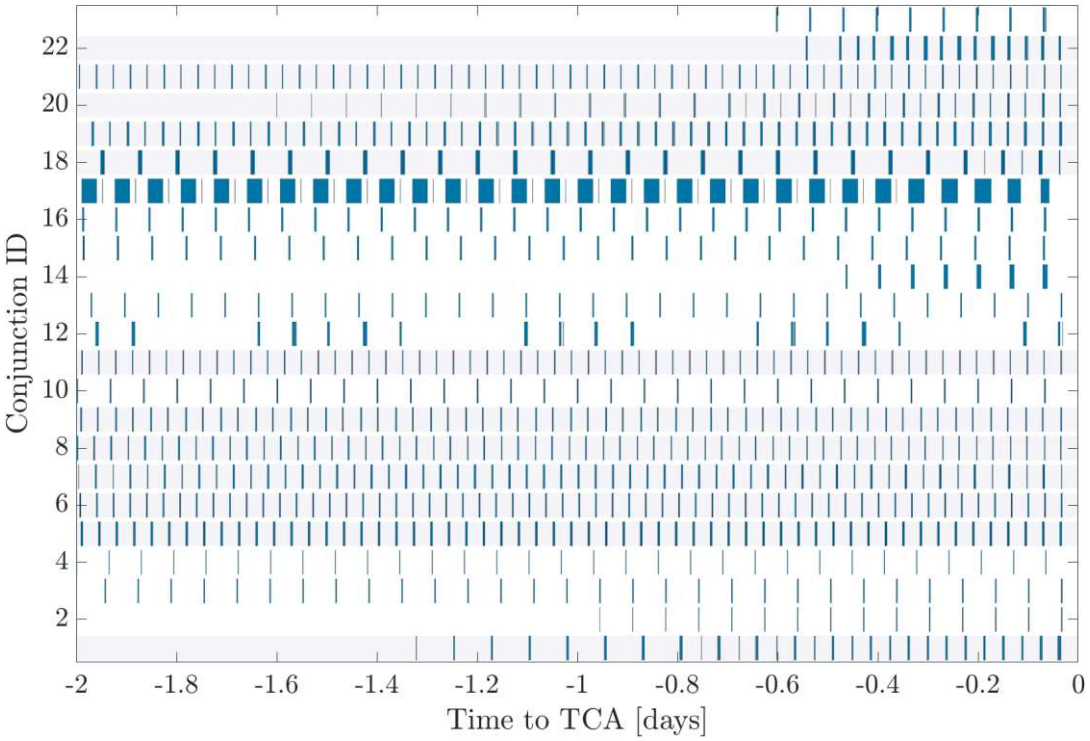

Fig 4.7 Visibility windows for 23 conjunctions during the two days before TCA. The blue bars indicate the observation intervals during which each conjunction is visible, with the length of each bar representing the duration of each visibility window. The shaded horizontal bands highlight conjunctions with two visibility windows per orbit.

The number of conjunctions featuring two good opportunities was higher than anticipated. If two orbits have two points of close proximity, it would be reasonable to assume that one point may be sunlit while the other remains in Earth's shadow. However, this did not hold true in the outcomes, requiring further investigation to understand the underlying causes.

Findings reveal a combination of two main factors. As shown in Fig. 3.5, most objects are in nearly polar orbits, often leading the proximity points between two conjuncting orbits to occur approximately above the Earth's poles. Coupling this

with the high altitude of satellites often allows them to remain illuminated by the Sun even when the Earth's surface directly below is in shadow. This phenomenon is illustrated in Fig. 4.8, which shows the orbital geometry for a conjunction between the Iridium Next SV117 satellite and a debris fragment from the Fengyun 1C satellite, a remnant of the 2007 Chinese anti-satellite test.

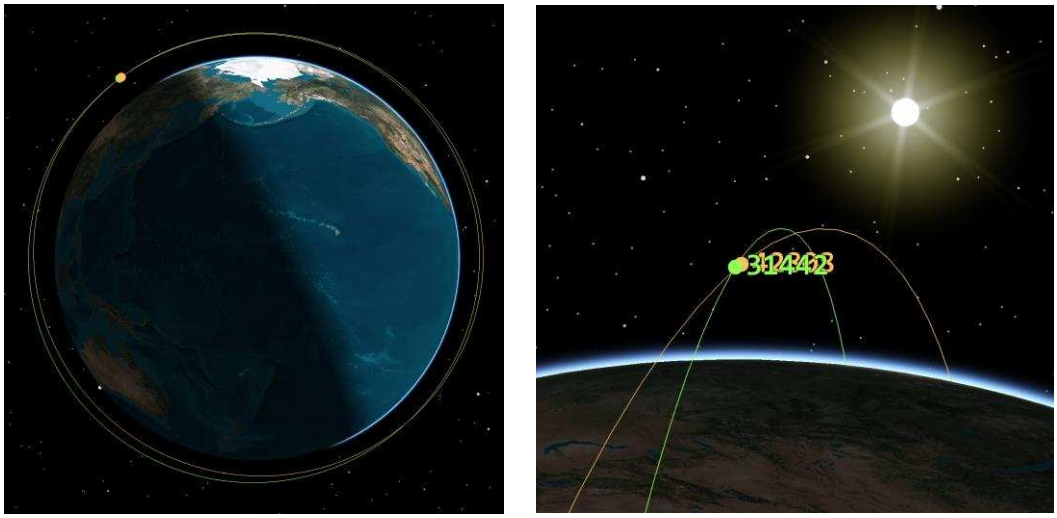

Fig. 4.8 Orbital geometry of a conjunction event, illustrating how both objects remain sunlit even when the point on Earth directly below them is in shadow.

Another factor—occurring in a smaller percentage of events—that causes two visibility windows at opposite nodal points is when one of the objects is in a nearly polar orbit that closely follows the terminator line on the ground, allowing the object to remain nearly continuously illuminated. As a result, favorable visibility conditions are maintained regardless of where the near-intersections occur. This is illustrated in Fig. 4.9, which shows a conjunction between Starlink 1350 and debris from the Iridium 33 fragmentation (i = 86.4 deg), where two good visibility windows are available close to the equator.

Fig. 4.9 Conjunction between Starlink 1350 (*orange*) and Iridium 33 fragmentation debris (*green*)

While the conditions in Fig. 4.7 represent favorable visibility, the likelihood of obtaining a quality observation depends on the specific performance characteristics of the sensor.

In nearly all cases, the peak SNR is achieved during the encounter that occurs either half or a full orbit before TCA, with variations dependent on the orbital geometry and illumination conditions. In temporal terms, this suggests that optimal observation conditions in LEO usually occur between 40 and 120 minutes ahead of the TCA.

The peak SNR from each conjunction is used to evaluate the performance of each sensor in terms of probability of detection (P_D) and image quality. In evaluating detection systems, successful object detection is usually determined by setting a threshold on the minimum SNR, whose value can vary depending on the operational context. According to the Rose criterion [48], the signal intensity should be at least five times σ_n, however thresholds for space surveillance may be set lower. For example, operational values at ESA are in the order of 4 [49] and even 3 [50]. This is feasible because, although a single pixel with a larger value than $3\sigma_n$ does not make a target, when several of such pixels align over multiple frames forming an apparent trajectory, the probability that it is an object increase steeply.

To avoid tying the results to a specific threshold, the P_D is calculated for each sensor twice, once with a SNR threshold of $3\sigma_n$ and again at $5\sigma_n$. Specifically, P_D is simply calculated as the percentage of conjunctions where detection is achieved with respect to the total number of simulated conjunctions. Given the many simulation variables, results are organized into different graphs where some of the parameters are held constant, to facilitate understanding the impact of the other parameters. In Fig. 4.10 to 4.13, the P_D is presented for all sensors by varying D while maintaining a constant μ=0.175. Each graph displays results for three sensors with same aperture size and electronics but different FoV, enabling a direct visual assessment of the individual impact of the FoV on the P_D. On average, increasing the FoV of 5 degrees enhances the P_D by approximately 5-10%. However, this improvement comes at the expense of a reduced image resolution, consequently amplifying the uncertainties in determining the positions of detected objects. Further evaluations, which incorporate the algorithms used for extracting orbital information from the images, are necessary to precisely quantify the loss in positional accuracy. Considering the stringent accuracy requirements of the proposed avoidance system, which aims to improve on ground-based estimates, a smaller FoV might be preferable despite the slight reduction in P_D. Conversely, other space-based SSA applications that prioritize detecting as many objects as possible, such as the uncued detection of uncatalogued objects, may benefit from a larger FoV.

As evident from Fig. 4.10, star trackers with a 2-cm aperture generally provide a low P_D, therefore not guaranteeing consistent object detection. Comparing the outcomes between the left graph of Fig. 4.10 (sensors #1, #2, #3) and the right graph (sensors #4, #5, #6) shows how better electronics, particularly in terms of a higher sensitivity and lower electronic noise, affects performance. The P_D for sensors #4, #5, #6 is significantly better, highlighting how selecting a good quality detector has a predominant impact on detection performance. Among the two modeled sources of

electronic noise, the readout one is observed to play a major role with respect to the P_D. This is due to the specific observation strategy employed here, entailing small exposure times. The influence of dark current noise accumulates more significantly over longer exposures, whereas the readout noise affects every image frame regardless of exposure duration.

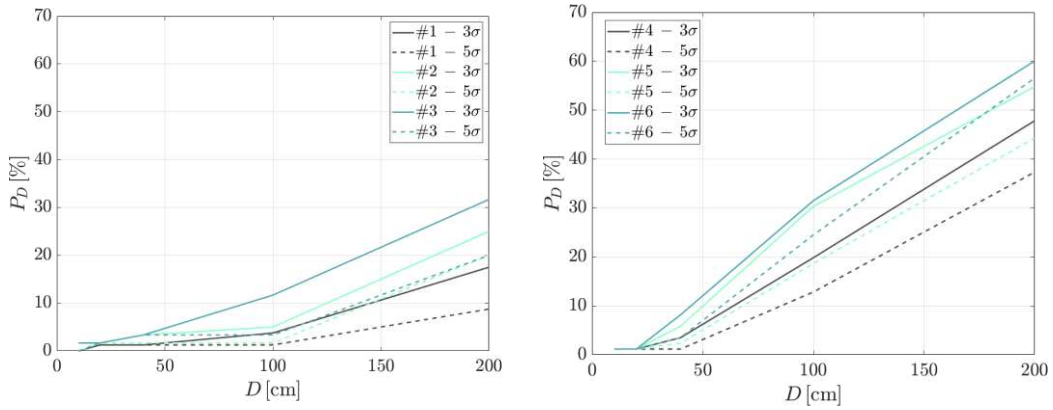

Fig. 4.10 P_D for sensors from #1 to #6 (2-cm aperture sensors) and μ=0.175. Each legend entry reports the sensor number and detection threshold used

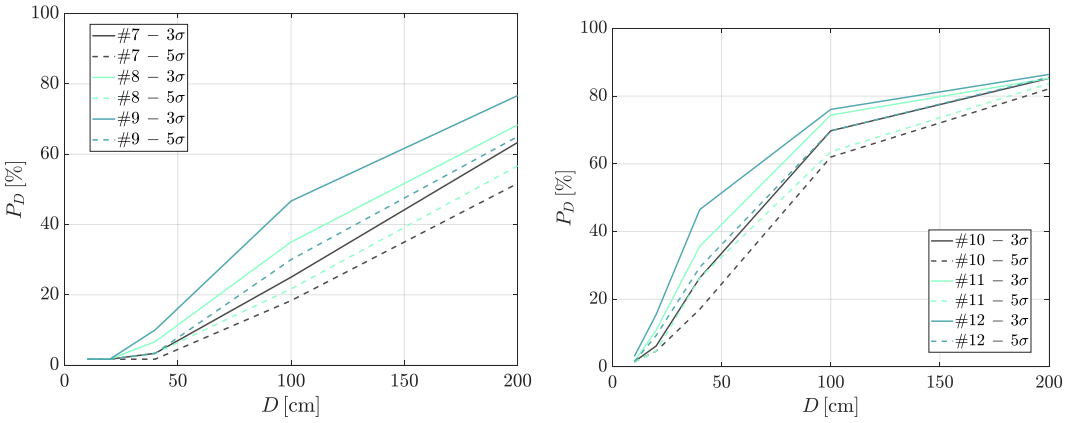

Fig. 4.11 P_D for the 5-cm aperture sensors and μ=0.175

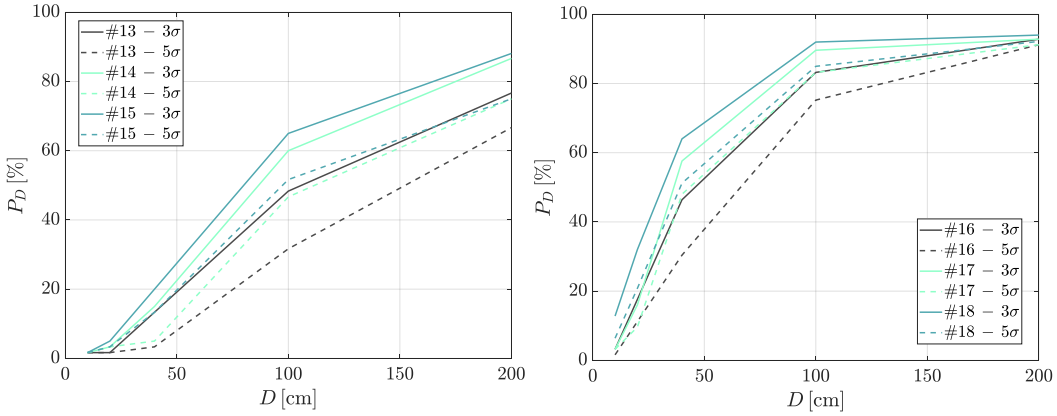

Fig. 4.12 P_D for the 7.5-cm aperture sensors and μ=0.175

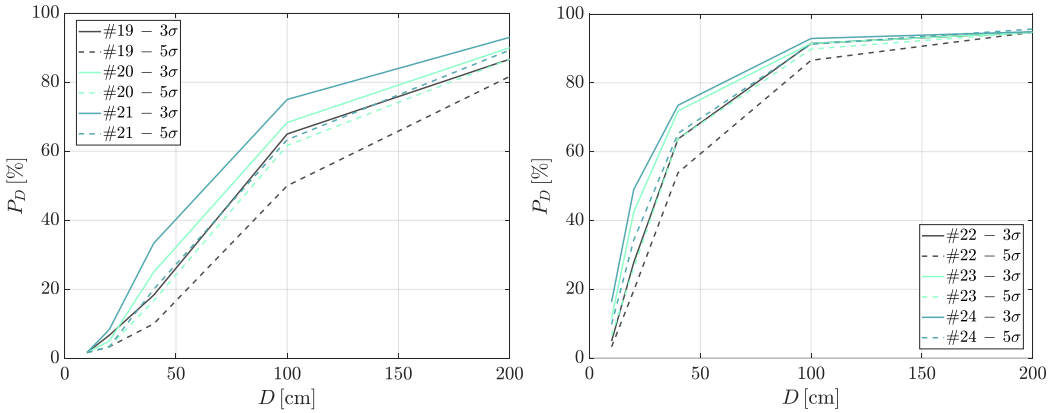

Fig. 4.13. P_D for the 10-cm aperture sensors and μ=0.175

To better grasp the sensitivity of P_D with respect to σ_m, additional simulations have been carried out by modeling a sensor with the same specifications of #11 but varying σ_m across three values: [5, 18, 32] e^-. The outcomes, illustrated in Fig. 4.14, evidence the nonlinear P_D sensitivity to reductions in readout noise, with more significant gains in detection probability observed at lower noise levels. This trend reflects the SNR equation's structure, where σ_m under the square root at the denominator means that each reduction is amplified in their effect on the SNR, thereby enhancing the P_D. In light of these considerations, sensors such as Rocket's Lab "ST-16RTZ" star tracker [51], with its 1.6-cm aperture and system noise as low as $3e^-$, could prove reliable detecting larger objects, despite featuring SWaP characteristics typical of Cubesat platforms.

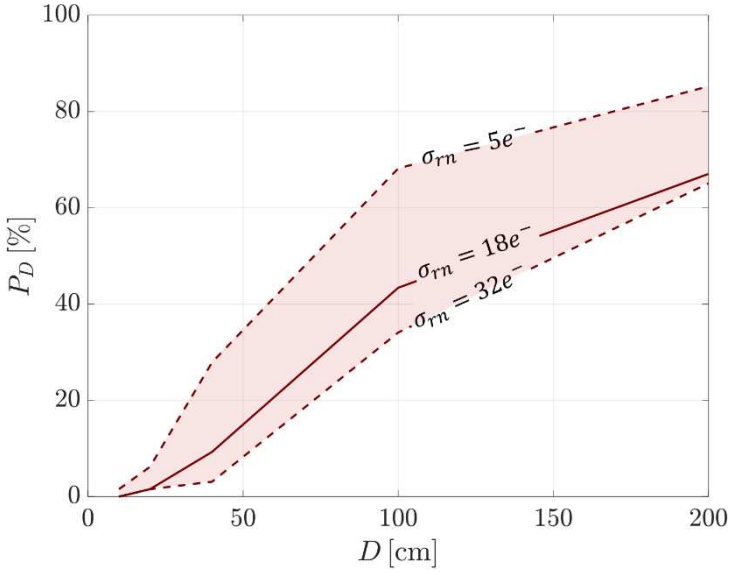

Fig. 4.14 Impact of the readout noise on the P_D. Simulation parameters: sensor #11, detection threshold $4\sigma_n$, values of σ_m = [5, 18, 32] e^-

Despite the low P_D offered by the 2-cm aperture sensors, their ability to occasionally detect large-class objects (>1 meter) might prove useful in several vital scenarios. A hypothetical scenario could be the 2009 collision that occurred between Iridium 33, an operational telecommunication satellite, and Cosmos 2251, a defunct Russian military satellite. Given that Cosmos had a 6.3 m² average cross-section [52], a 2-cm

aperture star tracker onboard Iridium might have been able to provide valuable measurements in the lead-time to TCA, potentially leading to a different outcome.

As shown in Fig. 4.11, 5-cm aperture sensors feature better performance. Those backed by good electronics ensure frequent detection of large objects, suggesting that they could find valuable application for satellites orbiting – or transiting by – densely populated regions, such as the altitudes occupied by mega-constellations. This is the case, for example, for payloads passing close to Starlink satellites, whose flat solar panel extends beyond the meter in the longitudinal direction. Sensor #12 demonstrates a reasonable capability to detect objects around 50 cm, but smaller sizes mostly remain undetected.

Higher P_D can be observed for the larger sensors, as illustrated in Figs. 4.12 and 4.13. However, increasing the aperture from 7.5 cm to 10 cm do not seem to yield significant improvements. This is because the P_D metric simply checks whether the SNR excdeeds a set threshold—a condition often met by both sensor sizes. To better understand the performance differences between sensors, it is useful to examine the distribution of SNR values they achieve. Fig. 4.15 addresses this by presenting a box-and-whisker plot that compares the SNR distributions for sensors #18 (D_A=7.5 cm) and #24 (D_A=10 cm) obtained for detected secondaries with a size of 100 cm. Both sensors demonstrate to be capable of regularly providing good quality images for target in these sizes.

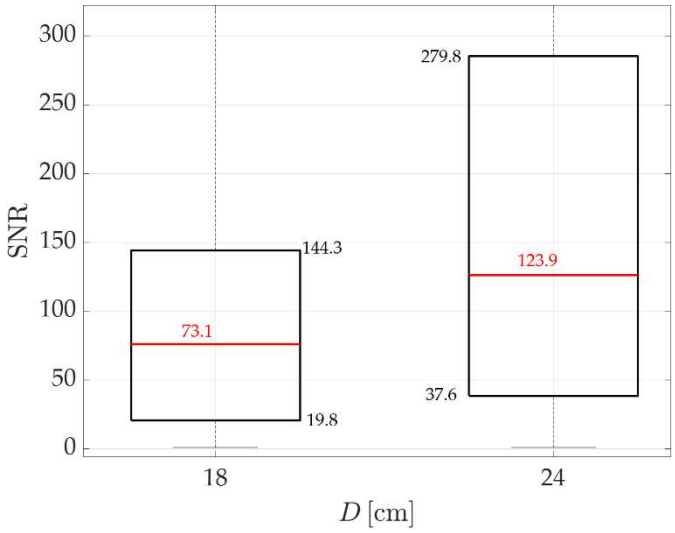

Fig. 4.15 Box-and-whisker plots for sensors #18 and #24 and considering targets sized 100 cm. The red lines correspond to the medians, while the lower and upper edges of the boxes indicate the 25% and 75% quartiles, respectively

The impact of different material surfaces that can characterize secondary objects is shown in Fig. 4.16, which displays the P_D considering sensor #6 and the three μ values of Table 4.5. As previously discussed, most objects in LEO feature reflectivities between the lower and upper bounds of μ used here, so the light blue colored area in Fig. 4.16 can be seen as a region of uncertainty. P_D variations within this range appear to be limited to roughly 10%.

The outcomes for sensor #25 are analyzed in Fig. 4.17. As expected, this sensor delivers superior performance by consistently detecting objects with diameters

above 40 cm. Many of the 20 cm objects are detected as well and, in about one-third of the cases, sensor #25 can detect 1U Cubesat-like objects, which currently are among the smallest objects detectable by ground-based systems.

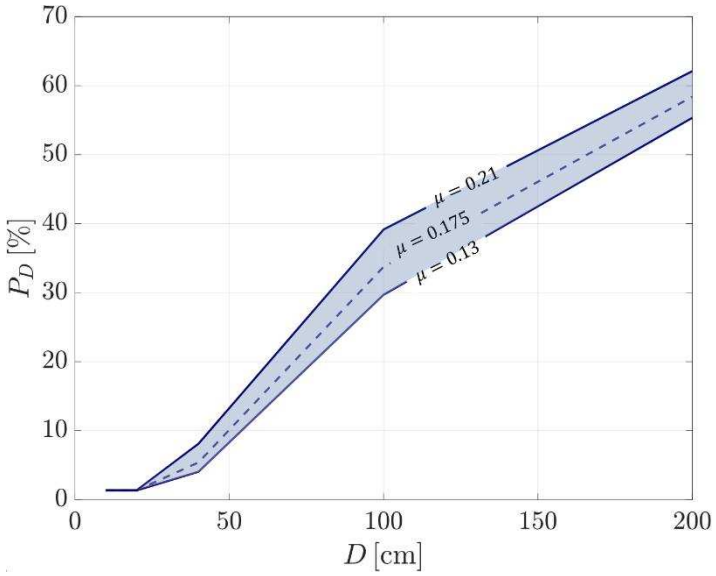

Fig. 4.16 P_D for sensor #6 and three values of μ

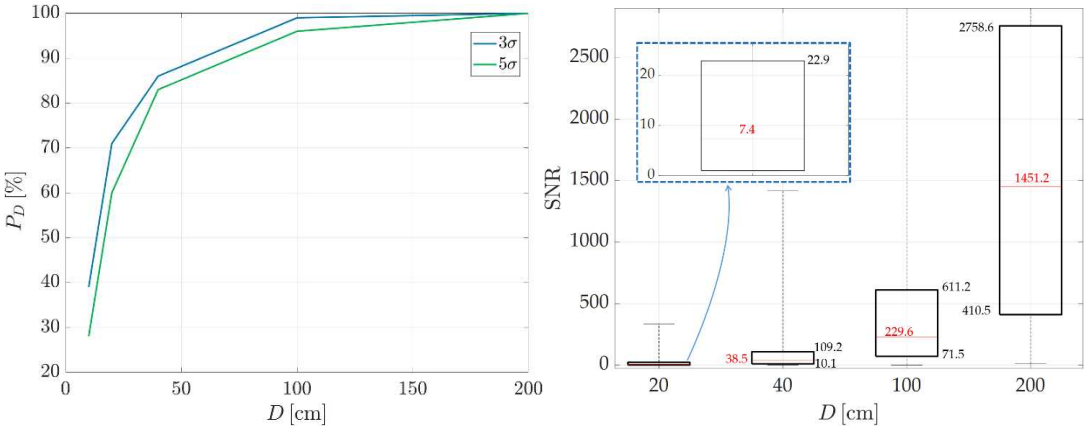

Fig. 4.17 Performance of sensor #25 (telescope). On the left, the P_D is plotted for against D assuming two different detection thresholds. On the right, SNR distributions are presented for targets larger than 20 cm

Some of the simulated conjunction events present particularly favourable visibility conditions, leading to generally higher SNR and succesfull observations even with the least capable sensors. One example is the conjunction between GHGSat C3, an active Canadian satellite at the time, and the inoperative German Cubesat SPiN-1. As shown in Fig. 4.18, the objects followed very similar, almost parallel orbital paths, resulting in very small relative velocities, as low as 0.02 km/s at the TCA. This configuration provides GHGSat C3 with multiple observation opportunities along its orbit, where SPiN-1 remains within the same pixel for longer-than-usual durations, resulting in higher SNR values.

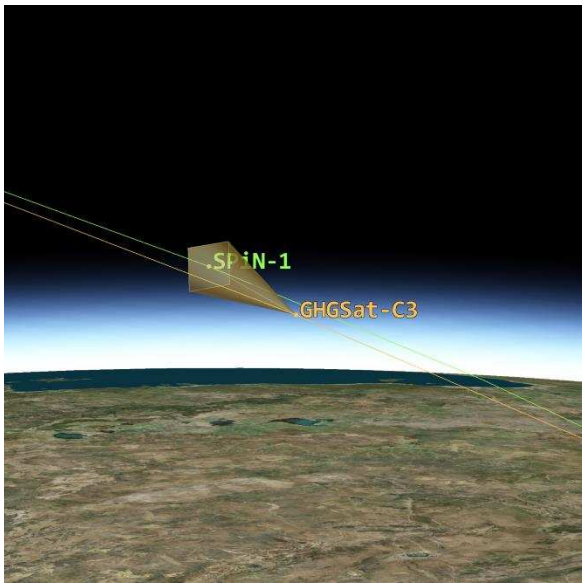

Fig. 4.18 Conjunction between GHGSat C3 and SPiN-1

Conversely, some conjunctions featured particularly unfavourable observation conditions, such as the one between Starlink-2444 and a Russian rocket's fragment, as shown in Fig. 4.19. Their significantly different orbital eccentricities and semi-major axes result in non-synchronized orbital motions, leading to large separations before TCA. Additionally, their orbits only come into close proximity within the Earth's shadow, precluding any possible observations. However, scenarios like the ones depicted in Figs. 4.18 and 4.19 only occur about 1% of the time.

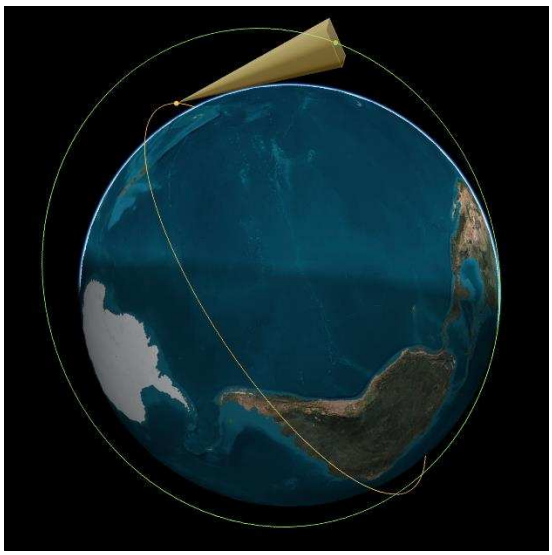

Fig. 4.19 Conjunction between the Starlink-2444 satellite and a Russian rocket's fragment

4.4 Summary of key findings and insights

Small star trackers, fitting the typical SWaP characteristics of Cubesat platforms, have not proven reliable for object detection. The best simulated 2-cm aperture sensor, with $S = 0.6$ and $\sigma_m = 8$ e^-, detects only 25-30% of secondaries sized 1-m and

about 60% for those sized 2-m. These detection rates are insufficient for implementing a reliable self-defense strategy, forcing hosting satellites to primarily rely on ground-based data. However, with a fair likelihood of detecting secondaries larger than 2m, 2-cm aperture sensors could still prove useful in critical situations. An example is the Iridium-Cosmos collision scenario, where the large cross-section of the Russian satellite (~6m²) suggest potentially good visibility by a small star tracker onboard Iridium. Moreover, small sensors could find application in complementing ground-maintained object catalogs by providing extra observations of large objects of interest as they pass close to the hosting platform, provided that the sensor is not engaged in other primary activities.

Sensors with a 5-cm aperture and high-quality electronics ($S = 0.6$, $\sigma_{rn} = 8$ e$^-$, $\sigma_{dc} = 30$e$^-$/s) and those with a 7.5-cm aperture can reliably detect most objects larger than 1-m. Given that large objects are more prone to trigger conjunction warnings than smaller debris, these devices could prove useful in numerous situations. This is particularly true for spacecraft orbiting in densely populated satellite regions, such as Sun-synchronous orbits or areas dominated by the new mega-constellations of micro and mini-satellites (e.g., Starlink).

Increasing the aperture to 10 cm leads to successful detection of objects as small as 20-40 cm and yields high-SNR images of larger objects, while larger telescopes can be effectively used in almost all conjunction scenarios. However, such sensors are not very common and typically only found on very large spacecraft or those primarily designed for optical observations. Increasing sensors' FoV improves detection rates but at the cost of resolution; however, given that positional accuracy is a priority for collision avoidance, smaller FoVs might be preferred.

Finally, the quality of sensor electronics significantly affects detection performance, as evidenced by lower-quality 2-cm aperture sensors ($S = 0.5$, $\sigma_{rn} = 30$ e$^-$, $\sigma_{dc} = 80$e$^-$/s) being nearly ineffective in all scenarios. Among the modeled electronic noise sources, σ_{rn} stands as the primary limitation on detection capability.

Looking ahead in star tracker development, although both larger optical apertures and improved detector electronics considerably enhance performance, the latter should be prioritized given the ongoing trend towards miniaturization in space technology.

References

[1] Planet Labs, "Planet Labs Constellations," 2024, Accessed: Apr. 19. [Online]. Available: https://www.newspace.im/constellations/planet-labs

[2] V. Franzese, F. Topputo, "Celestial bodies far-range detection with deep-space cubesats," *Sensors*, vol. 23, 2023, 4544, doi: https://doi.org/10.3390/s23094544

[3] D. Spiller, E. Magionami, V. Schiattarella, F. Curti, C. Facchinetti, L. Ansalone, and A. Tuozzi, "On-orbit recognition of resident space objects by using star trackers," *Acta Astronautica*, vol. 177, 2020, pp. 478–496, doi: https://doi.org/10.1016/j.actaastro.2020.08.009

[4] Japan Aerospace Exploration Agency (JAXA), "Close-up images of asteroid Ryugu," JAXA Hayabusa2 Project, 2018, Accessed: Apr. 19, 2024. [Online]. Available: https://www.hayabusa2.jaxa.jp/en/topics/20180828e/index.html

[5] 18th and 19th Space Defense Squadrons, "Spaceflight safety handbook for satellite operators," United States Space Force, Vandenberg, CA, USA, Tech. Rep., vers. 1.7, 2023

[6] S. Clemens, R. Lee, P. Harrison, W. Soh, "Feasibility of using commercial star trackers for on-orbit resident space object detection," in *AMOS Conference*, Maui, HI, USA, 2018

[7] M. Hejduk, J. Lambert, C. Williams, R. Lambour, "Satellite detectability modeling for optical sensors," in *AMOS Conference*, Maui, HI, USA, 2004

[8] V. Franzese, F. Topputo, "Celestial bodies far-range detection with deep-space cubesats," *Sensors*, vol. 23, n. 9 2023, doi: https://doi.org/10.3390/s23094544

[9] J. M. Nichols, C. Miller, "Analytical expression for the average ensquared energy," *Journal of the Optical Society of America A*, vol. 32, no. 4, 2015, pp. 654-659, doi: https://doi.org/10.1364/JOSAA.32.000654

[10] Terma, "T1 star tracker," March 06, 2024. Accessed May 09, 2024. [Online]. Available: https://www.terma.com/media/d1ifyxd3/terma_t1_str_data_sheet.pdf

[11] P. Davidsen, P. Hoffmeyer, "Terma next generation star tracker using APS," in *11th ESA ADCSS Workshop*, Noordwijk, Netherlands, October 17-19, 2017. Accessed May 09, 2024. [Online]. Available: https://indico.esa.int/event/182/contributions/1505/attachments/1468/1694/1645_-_Hoffmeyer.pdf

[12] Space Inventor, "STAR-T3 datasheet – v1.0 – May 2020," May 2020, Accessed May 5, 2024. [Online]. Available: https://satcatalog.s3.amazonaws.com/components/300/SatCatalog_-_Space_Inventor_-_STAR-T3_-_Datasheet.pdf?lastmod=20210723043101

[13] P. Davidsen, "Final presentation of "assessment star tracker for asteroid search," Feb 01, 2016, Accessed May 09, 2024. [Online]. Available: https://indico.esa.int/event/124/attachments/711/767/03_Assessment_of_Star_Tracker_Use_for_Asteroid_Search.pdf

[14] Sodern, "Auriga CP," Jul 2022. Accessed May 9, 2024. [Online]. Available: https://sodern.com/wp-content/uploads/2023/12/2022-02-OnePager-Auriga-CP-v2.pdf

[15] Sodern, "Hydra baseline," Oct. 2023. Accessed May 9, 2024. [Online]. Available: https://sodern.com/wp-content/uploads/2023/12/2023-12-Hydra-family.pdf

[16] Sodern, "Horus," Dec. 2022. Accessed May 9, 2024. [Online]. Available: https://sodern.com/wp-content/uploads/2023/12/2023-01-OnePager-Horus.pdf

[17] Leonardo, "A-STR and AA-STR," 2017, Accessed May 10, 2024. [Online]. Available: https://space.leonardo.com/documents/16277711/19573187/Copia_di_A_STR_Auto

nomous_Star_Trackers_LQ_mm07786_.pdf?t=1538987562062

[18] Jena Optronik, "Autonomous star sensor ASTRO APS," Jan. 2015, Accessed May 10, 2024. [Online]. Available: https://www.jena-optronik.de/products/star-sensors/astro-aps.html?file=tl_files/pdf/Data%20Sheet%20ASTRO%20APS.pdf

[19] Jena Optronik, "ASTRO APS3," Sep. 2022, Accessed: May 10, 2024. [Online]. Available: https://www.jena-optronik.de/products/star-sensors/astro-aps3.html?file=tl_files/pdf/Data%20Sheet%20ASTRO%20APS3.pdf

[20] Jena Optronik, "ASTRO CL star tracker," Jul. 2022, Accessed: May 10, 2024. [Online]. Available: https://www.jena-optronik.de/products/star-sensors/astro-cl.html?file=tl_files/pdf/Data%20Sheet%20ASTRO%20CL.pdf

[21] Jena Optronik, "High accuracy star sensor ASTRO XP," Apr. 2023, Accessed: May 10, 2024. [Online]. Available: https://www.jena-optronik.de/products/star-sensors/astro-xp.html?file=tl_files/pdf/Data%20Sheet%20ASTRO%20XP.pdf

[22] L.A.M. Christensen, "Multi-sensor data fusion for spacecraft navigation," Ph.D. dissertation, Dept. of Measurement and Instrumentation, Technical University of Denmark (DTU), Kongens Lyngby, Denmark, 2020

[23] D.A.K. Pedersen, "High accuracy tracking of space-borne non-cooperative targets," Ph.D. dissertation, Dept. of Measurement and Instrumentation, Technical University of Denmark (DTU), Kongens Lyngby, Denmark, 2015

[24] A.H. Jørgensen, D.A.K. Pedersen, "Assessment study of autonomous optical navigation for an asteroid impact mission," Technical University of Denmark (DTU), Kongens Lyngby, Denmark, Tech. Rep. ASC-DTU-AIM, Oct. 2016

[25] Rocket Lab., "Star tracker ST-16RT2," Jul. 2021, Accessed: May 10, 2024. [Online]. Available: https://www.rocketlabusa.com/assets/Uploads/RL-ST16RT2-Data-Sheet.pdf

[26] D. Michaels, and J. Speed, "Ball Aerospace star tracker achieves high tracking accuracy for a moving star field," in *2005 IEEE Aerospace Conference*, Big Sky, MT, USA, 2005

[27] Ball Aerospace, "High accuracy star tracker (HAST)," Jan. 2018, Accessed: May 10, 2024. [Online]. Available: https://www.ball.com/getattachment/adf4295c-2d64-49f9-a1cb-a2eb0f97217e/D1503_HAST_0118.pdf

[28] Blue Canyon Technologies, "Nano star trackers," Jan 2024, Accessed: May 10, 2024. [Online]. Available: https://storage.googleapis.com/blue-canyon-tech-news/1/2024/03/NST-2024.pdf

[29] Redwire, "Star tracker", Jun. 2021, Accessed: May 10, 2024. [Online]. Available: https://redwirespace.com/wp-content/uploads/2023/06/redwire-star-tracker-flysheet.pdf

[30] Arcsec, "SAGITTA star tracker", Aug 2021, Accessed: Dec 31, 2024. [Online]. Available: https://www.arcsec.space/pdf/Sagitta%20Star%20tracker%20datasheet%20V2.1.pdf

[31] J.E. Van Cleve, A. Lawitzke, E. MacAnlis, J.D. Griesbach, M. Sampson, D.P.

Osterman, E.D. Silva, C.J. Grant, and A. Bloom, "Hiding in plain sight: observing objects in low lunar orbit and the L2 dark cone from a lunar surface observatory," in *2021 AMOS Conference*, Maui, HI, USA, 2021

[32] W. Ogiers, S. Kowaltschek, J. Hoet, J. Vermeiren, "FAINTSTAR: A smart single-chip image sensor for next generation star trackers," in *The 4S Symposium 2022*, Vilamoura, Portugal, 2022

[33] ams OSRAM, "CMV4000 Global Shutter CMOS Image Sensor for Machine Vision," Aug. 2023, Accessed: May 10, 2024. [Online]. Available: https://look.ams-osram.com/m/5ddf0ec561bcbdcc/original/CMV4000-Global-Shutter-CMOS-Image-Sensor-for-Machine-Vision.pdf

[34] ON Semiconductor, "NOIH2SM1000A HAS2 image sensor," May 2013, Accessed: May 10, 2024. [Online]. Available: https://upverter.com/datasheet/1dbf6474f4834c5ac73294b488ac44ae8ac1f8ca.pdf

[35] S. Lutgring, E. Tchilian, "Performance testing a new medium accuracy star tracker," in *2022 IEEE Aerospace Conference*, Big Sky, MT, USA, 2022

[36] E. Plotke, P.C. Lai, Y.A. Chan, R.M. Ewart, K.Miller, J.Griesbach "Dual use star tracker and space domain awareness sensor in-space test," in *2021 AMOS*, Maui, HI, USA, 2021

[37] J. Feiteirinha, V. Kairiss, V. Reggestad, T. Flohrer, L. Maleville, J. Siminski, E. Maestroni, "STR4SD - Exploring the concept of opportunistically using star-trackers for space debris observations," in *1st NEO and Debris Detection Conference*, Darmstadt, Germany, 2019

[38] EO Portal, "NEOSSat – satellite missions," Accessed: Oct 17, 2024. [Online]. Available: https://www.eoportal.org/satellite-missions/neossat#nessi-near-earth-space-surveillance-imager

[39] Teledyne e2v, "4720 AIMO Imaging Sensors Datasheet," Tech. Datasheet, Teledyne e2v, 2024. Accessed: Oct 17, 2024. [Online]. Available: https://www.teledyne-e2v.com/en-us/Solutions_/Documents/datasheets/4720+aimo+A1A-100041_9_v1.pdf

[40] R. Anderson, G. Cantwell, "STK EOIR model description and validation," Space Dynamics Laboratory, North Logan, UT, USA, Tech. Rep. SDL/10-393, 2010

[41] C. J. Dennehy, A. A. Wolf, D. K. Swanson, F. Curti, C. Facchinetti, L. Ansalone, A. Tuozzi, "Spacecraft line-of-sight jitter management and mitigation lessons learned and engineering best practices," NASA, Hampton, VA, USA, Tech. Report NASA/TM−20210017871, 2021

[42] S. Lemmens, F. Letizia, "ESA's annual space environment report," ESA Space Debris Office, Darmstadt, Germany, Tech. Rep. GENDB-LOG-00288-OPS-SD, 2022

[43] M. Mulrooney, M. Matney, E. Barker, "A new bond albedo for performing orbital debris brightness to size transformations," in *2008 International Astronautical Congress*, Glasgow, Scottland, 2008

[44] M. Mulrooney, M. Matney, "Derivation and application of a global albedo

yielding an optical brightness to physical size transformation free of systematic errors," in *2007 AMOS Conference*, Kihei, HI, USA, pp. 719-728, 2007

[45] M. Mulrooney, M. Matney, M. Hejduk, E. Barker "An investigation of global albedo values," in *2008 AMOS Conference*, Maui, HI, USA, 2008

[46] J. Shell, "Optimizing orbital debris monitoring with optical telescopes," in *2010 AMOS Conference*, Maui, HI, USA, 2010

[47] J. Reyes, D. Cone, "Characterization of spacecraft materials using reflectance spectroscopy," in *2018 AMOS Conference*, Maui, HI, 2018

[48] A. Rose, "The Visual Process," in *Vision: Human and Electronic*, 1st ed. New York, NY, USA: Springer, 1973, ch. 1, sec. 1.2.3, p. 10

[49] J. Siminski, "Online space debris training course 2022, lecture 9: space surveillance," Lecture, ESA Space Debris Office, Darmstadt, Germany, 2022

[50] T. Flohrer, T. Schildknecht, R. Jehn, M. Oswald, "Performance of a proposed instrument for space-based optical observations of space debris," AIAA 2006-B6.1.01, in *57th International Astronautical Congress (IAC)*, 2006, doi: https://doi.org/10.2514/6.IAC-06-B6.1.01

[51] Rocket Lab, "Second generation star tracker (ST-16RT2)," Accessed: Oct 17, 2024. [Online]. Available: https://www.rocketlabusa.com/assets/Uploads/Star-trackers-product-sheet.pdf

[52] ESA's DISCOSweb, "Cosmos-2251 - Properties," Accessed: Oct 17, 2024. [Online]. Available: https://discosweb.esoc.esa.int/objects/22672

Chapter 5

Evaluation of orbit determination improvements

Once the detection limits of onboard optical sensors have been understood, it is now important to determine whether the information within the images can effectively contribute to improving trajectory data. Achieving this essentialy requires performing three tasks: target detection, astrometric reduction, and orbit determination (OD). The former involves identifying the intended target within the image, while astrometric reduction extracts useful data on the target, such as its position and uncertainty, and OD finally integrates these measurements with pre-existing trajectory data to refine the overall solution, enabling the evaluation of accuracy improvements.

In this chapter, a few case studies are set up starting from the conjunction events modeled in Section 4.1. For these events, images have already been produced and targets identified, providing a foundation for the other two steps, which are discussed in the following sections.

5.1 Astrometric reduction

Astrometry, one of the oldest branches of astronomy, focuses on the precise measurement of the positions and movements of stars and other celestial objects. To extract positional data from a raw astronomical image, the initial step involves matching the image with known star patterns to determine its exact orientation in the sky, as well as its field of view and scale. This technique is often referred to as *plate solving*—a term originating from early astronomical practices when observations were recorded on photographic plates, still used today to refer to digital images captured by telescopes.

5.1.1 Pixel-to-sky coordinates

The process begins by detecting stars within the image through the identification of bright pixels. Using a reference star catalog, such as those provided by Gaia or Tycho, these detected star patterns are then matched to known star positions. Adjustments for scale, rotation, and orientation bring the observed star patterns into

alignment with the catalog data. Once a match is found, the center of the image is identified in terms of celestial coordinates (Right Ascension and Declination, or RA/DEC), essentially "pinning down" where in the sky the image is centered. Plate solving then establishes a precise mathematical transformation—or mapping—between the pixel coordinates in the image (x, y) and celestial coordinates (RA/DEC), accounting for factors such as the pixel scale[7], rotations, and the presence of distortions in the image. This enables the precise location of any object in the image.

It must be noted that, for images captured by orbiting platforms, an alternative indirect method exists to map pixels to celestial coordinates (RA/DEC). This method leverages the satellite's known attitude, provided by onboard navigation instruments, to estimate the image's orientation in space. The attitude information is used along with the known camera's orientation within the spacecraft to perform a sequence of transformations that link pixel coordinates with celestial coordinates through intermediate frames, including the camera frame and the satellite's body frame. However, each transformation step introduces small but cumulative errors, as they depend on precise knowledge of the satellite's attitude and the alignment of the camera relative to the satellite body. These minor inaccuracies introduce biases, making this approach inherently less precise than plate solving. Therefore, this method is typically used only when plate solving is not feasible, such as when images contain too few visible stars for reliable matching. This generally occurs when very close or bright objects dominate the image, such as during close-proximity or rendezvous operations [1]. Therefore, for the purposes here, it is assumed that plate solving is always possible and thus is the primary method used to derive the mapping rule.

Several advanced plate-solving tools are freely available online, among which the one provided by Astrometry.net—referred to here as *AstrNet*—is selected for its widespread adoption. Unlike other tools, AstrNet can perform blind plate solving, meaning it can generate a solution without prior information about the image's orientation or scale [2]. It works by detecting stars in the input image, grouping them into unique sets of four stars called "quads" based on their relative positions, and converting these quads into hash values. These are then compared against a database of cataloged quads, with the solution found when a match is identified and verified across multiple quads.

Figure 5.1 shows the solution of AstrNet for a synthetic image generated through EOIR. Where red and green circles overlap, a matched star is identified and used to calculate the solution.

As is typical for plate-solving tools, the output mapping solution is saved in a Flexible Image Transport System (FITS) file, following World Coordinate System (WCS) conventions. Several scripts were developed in MATLAB to extract key information from the FITS files and create a direct function to transform pixel coordinates into sky coordinates. The detailed steps followed for this process are

[7] The *pixel scale* is the angular distance on the sky corresponding to a single pixel in the image. It is a direct measure of an optical system's resolution, depending on both the focal length and sensor size, and is typically expressed in arcseconds or arcminutes per pixel.

described in Appendix B. In brief, FITS files contain a "data" section, typically storing the raw astronomical image, and a "header" section, which includes essential image data such as pixel scale and transformation parameters, which are required to construct the mathematical mapping. These parameters, defined according to WCS conventions, support both a linear transformation that accounts for rotation and shear, and a nonlinear transformation in Simple Imaging Polynomial (SIP) form to address image distortions.

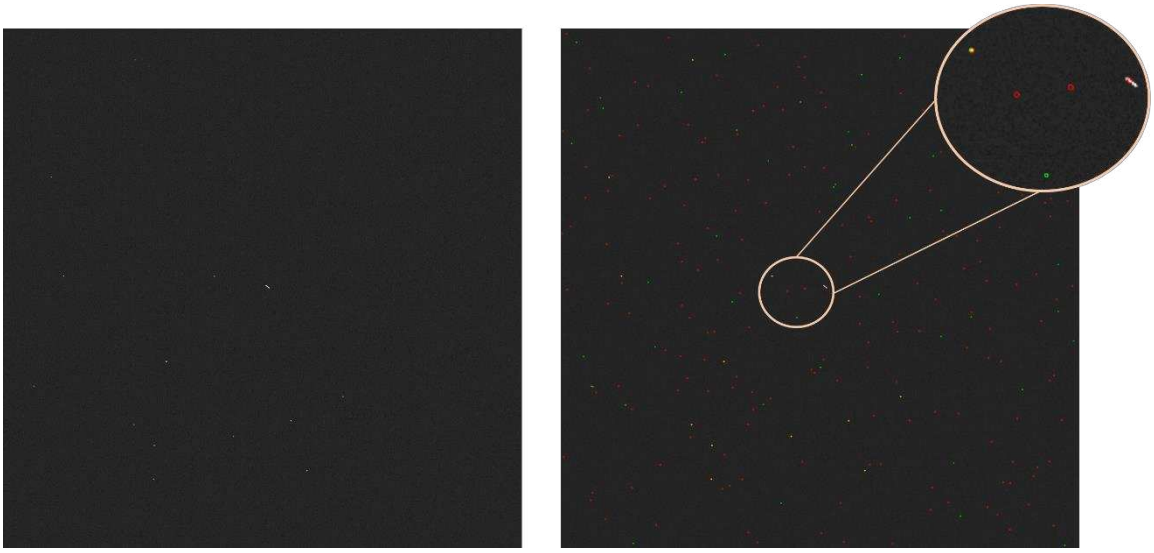

Fig. 5.1 *Left:* Synthetic image generated using EOIR, showing a streak left by a simulated object moving through the center of the FoV. *Right*: AstrNet's solution for the same image, with red circles indicating bright pixels detected by the algorithm and green circles marking the cataloged star positions used by AstrNet

A quick test has been conducted to validate the above procedure for obtaining mapping functions. Conveniently, along with the main FITS file containing WCS parameters, AstrNet also provides additional files, such as a table listing the detected bright sources (red circles in Fig. 5.1) that match reference catalog stars (green circles). The table reports both pixel coordinates and RA/DEC values, which are calculated through WCS transformation. By converting the pixel coordinates to RA/DEC values using the derived mapping function and comparing the outcomes with the known RA/DEC values from the table, the mapping function can be validated.

The test was conducted across thousands of stars, yielding an average error of approximately 0.12 arcseconds in both RA and DEC values. This error can be attributed to the fact that the RA/DEC values listed in the table are rounded to four decimal places, which is less precise than the calculated values through Matlab, which provides around 15-16 decimal digits of precision. Consequently, the maximum possible precision in their difference is 0.00005 degrees (equivalent to 0.18 arcseconds), a negligible error for the subsequent analyses.

Concerning the reference frame in which RA/DEC values are returned by the WCS transformation, AstrNet relies on the USNO-B star catalog for its calculations [2], which is referenced to the Mean Equator and Mean Equinox (MEME) J2000 reference

frame[8] [3], so the resulting RA/DEC coordinates will be in that frame. However, objects trajectories in STK have been modeled in the International Celestial Reference Frame (ICRF)[9]. As the two reference frames nearly coincide, with only a small rotational difference of about 0.1 arcseconds [4], the resulting error is disregarded in this work.

Since the mapping parameters are derived by plate-solving images taken from simulated spaceborne sensors, the resulting RA/DEC values will be expressed in a spacecraft-centered frame (where the spacecraft is the one hosting the simulated sensor). While the RA/DEC of distant stars does not change whether measured in a spacecraft- or Earth-centered reference frame, for nearby objects, such as other satellites or space debris, this difference is important and must be considered when performing OD.

5.1.2 Centroid computation

The derived mappings are used to produce RA/DEC measurements corresponding to the target's location within the images. As mentioned earlier, this chapter assumes that targets have already been identified using the simplified method described in Section 4.1.4.1, which provides a Region of Interest (ROI) around the pixels of the target streak. Future work aims to establish a robust strategy for identifying low-SNR targets through stacked image-processing techniques.

Starting from a ROI, a few options are available to produce target measurements. When objects of interest in astronomical images appear as single points or blurred spots — as is the case for distant stars, galaxies, and small moons — measurements can be obtained by fitting the characteristic Point Spread Function (PSF) of the instrument used to the detected object. A simpler approach, if most of the light from an object falls within a single pixel, is to take the center of that pixel as the position of the object. This achieves a resolution limited to one pixel, which could be improved by slightly defocusing the camera to spread the light over multiple pixels and thus expanding the PSF; this enables a more precise localization of the object's center, albeit with a minor trade-off in clarity.

For streaks, especially long ones, one approach is to identify the endpoints of the streak and produce two RA/DEC measurements representing the object's position at the beginning and end of the sensor's exposure time τ, as was done for the MOST satellite's observations [5]. However, as the streaks in this work are relatively short (2–3 pixels), a single measurement is taken at the "centroid" of the streak and associated with the time corresponding to half the exposure time ($\tau/2$), as done in [6]. The centroid refers to a coordinate position calculated as the weighted average of pixel coordinates, where each coordinate is weighted according to its pixel's

[8] The MEME J2000 frame is based on the Earth's equator and equinox positions as of January 1, 2000, at 12:00 TT (Terrestrial Time). The x-axis points toward the mean vernal equinox (the intersection of the celestial equator and ecliptic planes), the z-axis is normal to the mean equator of that date, and the y-axis completes the right-handed coordinate system [4].

[9] The ICRF is the best realization of an inertial reference frame. It was designed to coincide as closely as possible with MEME J2000, but unlike this latter, whose axes depend on Earth's equatorial and ecliptic planes, the ICRF axes are fixed with respect to extragalactic objects.

brightness [7].

Using the pixels inside a ROI, the streak centroid is calculated using the two-steps method described in [8]:

1) The image momenta I_{00}, I_{01} and I_{10} are calculated as:

$$I_{00} = \sum_{i,j \in ROI} I_{i,j} w_{i,j} \qquad I_{10} = \sum_{i,j \in ROI} X_{i,j} I_{i,j} w_{i,j} \qquad I_{01} = \sum_{i,j \in ROI} Y_{i,j} I_{i,j} w_{i,j} \tag{5.1}$$

where $X_{i,j}$ and $Y_{i,j}$ represent the pixel coordinates, $I_{i,j}$ is the intensity at pixel (i, j), and $w_{i,j}$ is a weighting factor applied to each pixel, which is calculated as $w_{i,j} = I_{i,j}/I_{i,j}^{max}$, giving more weight to brighter pixels.

2) The centroid coordinates are obtained as:

$$X_c = \frac{I_{10}}{I_{00}}, \qquad Y_c = \frac{I_{01}}{I_{00}} \tag{5.2}$$

Figure 5.2 shows an example of the discrepancy between the calculated centroid of a streaked object's and its true position at $\tau/2$. Running the algorithm across multiple tests showed a typical positional accuracy between 0.6 and 1.1 pixels.

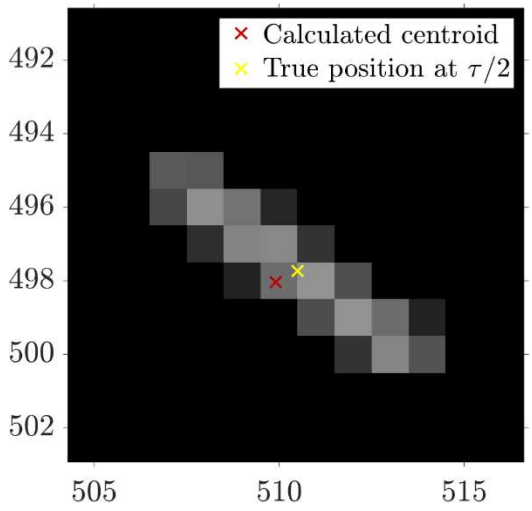

Fig. 5.2 Example of calculated streak centroid and true target's position at half the exposure time ($\tau/2$)

5.1.3 Annual aberrations correction

Once the centroid is calculated in pixel coordinates, the pixel-to-sky mapping can be used to determine a pair of RA/DEC coordinates. However, a small correction is needed to account for orbital aberrations—an error in the measured position of an object in an astronomical image due to the observer's movement around the Sun. This movement causes the observed direction of a star to differ slightly from its true direction. When the observer is on Earth, this effect is called "annual aberration."

In this context, RA/DEC coordinates measured directly from an astronomical image are referred to as "apparent" RA/DEC. Instead, "corrected" RA/DEC are the

coordinates obtained after accounting for these aberrations, representing the "true" positions of celestial objects in a more inertial frame. The correction adjusts the apparent positions to what they would be if viewed from a stationary point at the Solar System's barycenter.

When AstrNet processes an image, it assumes that annual aberrations must be corrected, so the resulting map provides already adjusted coordinates. However, in the present application, this correction is wrong for two reasons. First, EOIR image generation does not account for these aberrations, so all objects are already displayed in their true positions (aside from simulated optical aberrations). Second, aberrations only impact distant objects moving at different velocities relative to Earth in an inertial frame, such as stars. For closer objects, like satellites and space debris, this effect does not need to be considered. Therefore, the RA/DEC values produced through AstrNet mapping must be 'un-corrected' for annual aberrations, which is done here following the procedure outlined in Appendix C.

5.2 Measurement uncertainties

As previously mentioned, calculating the collision probability P_C between space objects requires an estimate of both their state and their uncertainty, which is typically represented by a square 'covariance' matrix including position and velocity uncertainties across three coordinates. The first three diagonal elements indicate the variance in each position coordinate, while the last three represent variance in each velocity component. Off-diagonal elements capture covariances, reflecting dependencies between different position and velocity coordinates.

To obtain a reliable P_C, a robust estimate of the covariance matrix is essential, which requires that the RA/DEC pairs are accompanied by associated uncertainties. These enable OD algorithms to properly weight each measurement, assigning greater weight to measurements with lower uncertainties, resulting in more accurate covariance matrix.

For space-based measurements, uncertainties can arise from various sources, such as instrumental noise and the limited knowledge of the tracking platform's position. In this work, the following relationship is used to estimate the total observation measurement error:

$$\sigma_{tot}^2 = \sigma_{\text{starfit}}^2 + \sigma_{\text{centr}}^2 + \sigma_{\text{par}}^2 + \sigma_{\text{timing}}^2 + \sigma_{\text{unknown}}^2 \tag{5.3}$$

Equation (5.3) combines different sources of error using a root-sum-square, implying that the errors are assumed to be uncorrelated. The sources include:

- $\sigma_{\text{starfit}}^2$: errors arising from fitting the observed star positions to the image coordinates
- σ_{centr}^2: errors in determining the streak centroid
- σ_{par}^2: parallax error due to the limited precision available for the tracking platform's position

- σ^2_{timing}: timing error due to uncertainties in the exact time at which the observation was recorded
- $\sigma^2_{\text{unknown}}$: a general term for unquantified error sources, which will be disregarded in the subsequent analysis

Equation (5.3) can be expressed either in terms of pixels or, by multiplying all components by the sensor's pixel scale, in terms of arcseconds. Originally introduced by [9] for quantifying the data quality of the SBV sensor onboard the MSX satellite, it was later used for MOST satellite's observations [5] as well, but it remains valid for ground-based observations as well.

While σ_{tot} represents the *total* angular error, it will be decomposed into RA and DEC components to directly correspond with the obtained centroid coordinates, which are expressed in RA/DEC components. First, however, each error source is quantified based on the sensor's characteristics and other contributing factors.

5.2.1 Coordinate fit error (σ_{starfit})

This source serves as an indicator of the quality of the mapping solution. Its magnitude largely depends on the accuracy of the algorithm used for plate solving, but the maximum precision achievable is limited by the sensor's pixel scale and the density of stars visible in the image.

Notably, the "cross-boresight" accuracy parameter usually reported in star tracker's datasheets is indicative of their σ_{starfit} error. These devices operate by comparing captured star field images with an onboard catalog to determine the satellite's orientation. The cross-boresight accuracy indicates the accuracy achieved along the directions perpendicular to the sensor's boresight (i.e., yaw and pitch). As σ_{starfit} reflects angular deviations in the two-dimensional sensor plane, it directly corresponds to cross-boresight accuracy. It is worth noting that, for attitude determination purposes, the other error sources in Eq. (5.3) are negligible in star trackers, making σ_{starfit} a direct indicator of the device's performance. Those error sources only become relevant for detection tasks involving nearby, moving objects.

To evaluate σ_{starfit} in the present application, the supplementary files provided by Astrnet alongside the main solution are exploited. As previously mentioned, these include a table listing the matched stars in the image. This table contains the pixel coordinates of each star, both as measured from the image and as calculated based on their expected positions according to the reference star catalog. Comparing these measured and expected positions across all stars provides a quantitative measure of the uncertainty in the plate solution. Specifically, the root-mean-square (RMS) error across all stars is first computed in pixels, then multiplied by the sensor's pixel scale (in arcseconds per pixel) to convert it to an angular error, yielding σ_{starfit}.

This procedure was tested on numerous images generated through EOIR, with sensor parameters varied as in Table 4.3. As expected, the sensor's pixel scale proved to be the primary factor influencing σ_{starfit}, with smaller pixel scales allowing for greater accuracy, while star density in the images played a minor role. However, although the results were consistent, they were slightly below expectations. In particular, when comparing simulated sensors to similar commercially available

hardware, the achieved accuracy was around 2–4 times worse. In particular, regardless of the simulated sensor type, calculated RMS errors generally range between 0.4 and 1.1 pixels.

While achieving sub-pixel accuracy in most cases is favorable, literature on plate-solving algorithms implemented in spacecraft onboard devices (including star trackers) reports better results. For instance, the star tracker described in [10] achieves an RMS error of 0.2 pixels, which the authors describe as "modest." The algorithm used by [11] achieves an average error of approximately 0.011 pixels, aligning with studies by [12] (~0.04 pixels) and [13] (between 0.005 and 0.013 pixels).

A few tests have been done by feeding AstrNet with real star tracker images, to determine if the issue was related to EOIR-generated images, but the results remained roughly the same. After careful consideration, it was concluded that the discrepancy is likely due to the general-purpose nature of the AstrNet solver, which makes it less precise than specialized software. AstrNet is a blind, versatile solver designed to handle a wide variety of cases—from narrow to wide FoV images and both ground- and space-based observations, which feature very different background noise levels. Therefore, AstrNet is not specifically calibrated to the unique characteristics of any particular optical system. By contrast, onboard camera and star tracker algorithms are generally fine-tuned to their expected environments, compensating for known background noise levels and lens system specifics, including camera defocus and the PSF.

As a result of this discussion, it was decided to adopt a σ_{starfit} value corresponding to a random number between 0.2 to 0.5 pixels, which is considered a more realistic estimate of the achievable performance in orbit. Assuming that σ_{starfit} is equally contributed to by error in RA and DEC, it can be decomposed as

$$\sigma_{\text{starfit}}^2 = \sigma_{\text{starfit,RA}}^2 + \sigma_{\text{starfit,DEC}}^2 \tag{5.4}$$

5.2.2 Centroiding error (σ_{centr})

The centroiding error is generally treated independent of the coordinate fit error, though this is not always the case if, for instance, distortions in the image that are not properly captured with the coordinate fit.

This error is calculated here as follows:

$$\sigma_{\text{centr}} = \frac{FWHM}{2 \cdot SNR} \tag{5.5}$$

where $FWHM$ is the full width at half maximum of the source. As noted in [14], the above relationship—which has been extensively validated by both ground- and space-based observations—is an approximate estimate that aligns with other theoretical models (e.g., [15] and [16]), despite slight variations in the scaling factor used at the denominator.

For point-like sources with well-sampled PSFs, the FWHM can be readily calculated using analytical formulas. However, for elongated streaks, the calculation is a little

trickier, as the PSF stretches along the object's direction of motion projected onto the Focal Plane Array (FPA), resulting in a larger FWHM in that direction. Additionally, covariance develops between the x and y axes of the FPA, and consequently in the RA and DEC directions.

Referring to the example in Fig. 5.3, the method used here to calculate the FWHM of an oblique streak begins by identifying the orientation of the streak within the ROI, as shown in the top-left panel of the figure. Using Principal Component Analysis (PCA) on the coordinates of the streak pixels, the primary direction of the streak is determined. This angle is used to rotate the ROI so that the streak becomes horizontally aligned, as illustrated in the top-right panel. With the streak aligned, intensity profiles are extracted in two directions: along the streak (horizontal) and perpendicular to it (vertical), as shown in the bottom-left and bottom-right panels of the Fig. 5.3, respectively. Finally, the FWHM in each direction is computed by locating the points where the intensity crosses half of the maximum value in each profile.

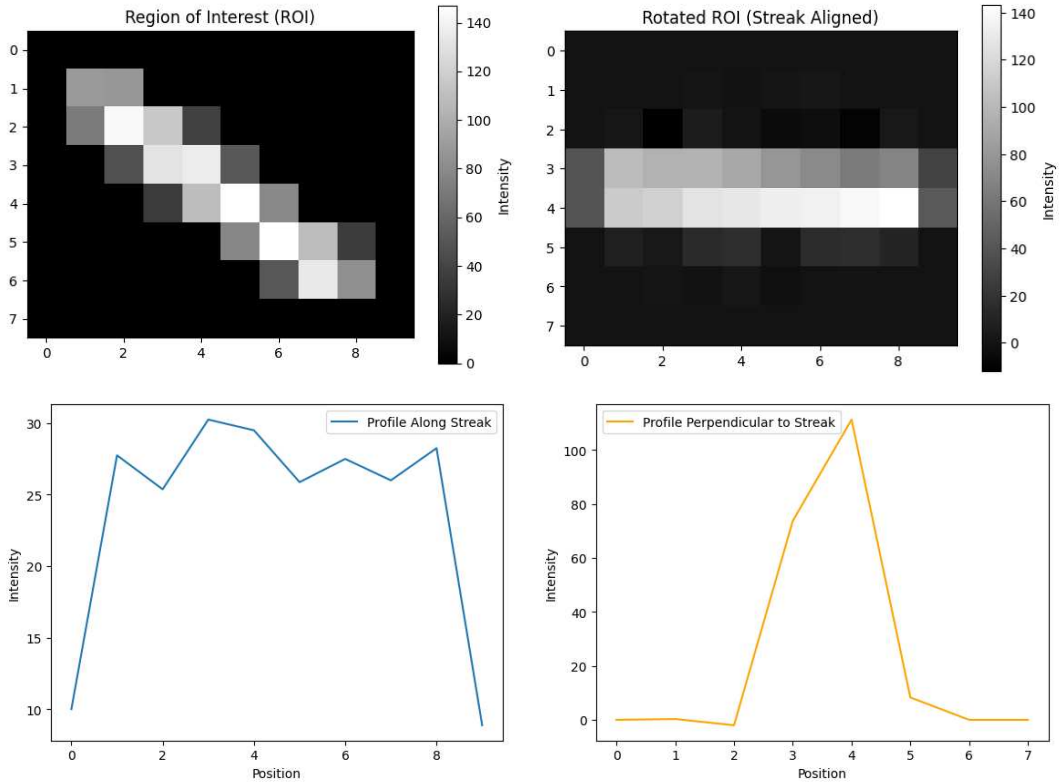

Fig. 5.3 Steps for calculating the FWHM along and across the principal direction of an oblique streak

Denoting $FWHM_{\parallel}$ and $FWHM_{\perp}$ as the FWHM values in the along-streak and across-streak directions, respectively, the example shown in Fig. 5.3 has these values at 7 pixels and 1 pixel. However, this example features a relatively long streak for illustration, while the observation strategy employed here typically produces streaks around 2–3 pixels in length. For a FWHM of 2 and a SNR of 4, the resulting error is of 0.25 pixels—a scale comparable to the coordinate fit error.

In theory the uncertainties obtained in the two directions should be projected onto a

spacecraft-centered ICRF frame to be able to convert them into RA/DEC components. However, in a conservative manner, the error in the along streak direction is assumed to uniformly represent the centroid error in each direction. Therefore, σ_{centroid} can be evenly split into $\sigma_{\text{centr,RA}} = \sigma_{\text{centr,DEC}} = \frac{FWHM_{\parallel}}{2\sqrt{2} \cdot SNR}$.

5.2.3 Parallax error (σ_{par})

When a satellite's position is not perfectly known, this uncertainty in its location results in a slight inaccuracy in determining the exact position of target objects. Let σ_{eph} denote the 1-sigma uncertainty in the location of the tracking platform and let R denote the slant range with respect to the observed target. Provided that $R \gg \sigma_{\text{eph}}$, the parallax error can be calculated as:

$$\sigma_{\text{par}} \approx \frac{\sigma_{\text{eph}}}{R} \tag{5.6}$$

where σ_{eph} and R should be expressed in either meters or kilometers. Equation (5.6) provides the error in radians, which can be converted to arcseconds by multiplying by 206,265 (the number of arcseconds in a radian).

The parallax error can be quite significant relative to other contributions if the tracking platform is not accurately tracked. For instance, a target at distance of 500 km leads to a parallax error of 41.3 arcseconds if σ_{eph} is 100 m. However, primary satellites considered here are assumed to carry GNSS devices, limiting positional uncertainties to about 15 meters. Since the adopted observation strategy results in secondary objects typically observed at distances above 300 km, the maximum parallax error is $\sigma_{\text{par}} = 10.3$ arcseconds. On the other hand, the maximum detection distances are around 800 km, resulting in an error of less than 4 arcseconds. Assuming there is no preference direction for σ_{par}, it can be evenly split between RA/DEC components, thus $\sigma_{\text{par,RA}} = \sigma_{\text{par,DEC}} = \frac{\sigma_{\text{par}}}{\sqrt{2}}$.

5.2.4 Timing error (σ_{timing})

When a satellite records the position of an object, even a small error in the time-tagging of that observation can translate into a positional error because the object continues to move during the time discrepancy. The error is generally due to unmodeled systematic inaccuracies in the on-board clock, which serves as the timing reference, and can be calculated as:

$$\sigma_{\text{timing}} \approx \omega * \sigma_t \tag{5.7}$$

where ω is the relative angular rate of the target (in arcseconds per second), and σ_t is the timing uncertainty (in seconds).

Alternatively, σ_{timing} can be obtained using the relative velocity of the target projected onto the FPA, denoted as v_{FPA}, and the range to the target:

$$\sigma_{\text{timing}} \approx \frac{v_{FPA}}{R} * \sigma_t \tag{5.8}$$

This error has been a dominant contribution for observation satellites lacking a

proper timing reference [5]. However, many modern satellites in LEO use timing signals from GNSS devices to synchronize their onboard clocks to a high accuracy. For instance, GPS-based time synchronization achieves a documented timing offset within 30 nanoseconds 95% of the time (15 nanoseconds 1-sigma) [17]. Considering a worst-case scenario in which a secondary object is traveling at 1 km from the primary and with a velocity $v_{FPA} = 8$ km/s, the resulting timing error (considering $\sigma_t = 30$ ns) is less than 0.002 arcseconds. For this reason, σ_{timing} is disregarded here.

Putting together the above discussions, the total angular error can be written in terms of RA/DEC components as:

$$\sigma_{tot}^2 = \sigma_{\text{starfit}}^2 + \sigma_{\text{centr}}^2 + \sigma_{\text{par}}^2 =$$

$$= (\sigma_{\text{starfit,RA}}^2 + \sigma_{\text{starfit,DEC}}^2) + (\sigma_{\text{centr,RA}}^2 + \sigma_{\text{centr,DEC}}^2) + (\sigma_{\text{par,RA}}^2 + \sigma_{\text{par,DEC}}^2) = \quad (5.9)$$

$$= \sigma_{RA}^2 + \sigma_{\text{DEC}}^2 = 2\sigma_{RA}^2 = 2\sigma_{DEC}^2$$

where the final expression reflects the fact that RA and DEC contributions are assumed equal for all error sources, as discussed earlier.

By substituting explicit expressions for each term in Eq. (5.9) and incorporating all assumptions discussed above, σ_{RA} and σ_{DEC} can be expressed in arcseconds as follows:

$$\sigma_{\text{RA}} = \sigma_{\text{DEC}} =$$

$$= \frac{\sqrt{2}}{2}\sqrt{(\text{rand}(0.2, 0.5) \cdot p_{scale})^2 + \left(\frac{FWHM_{\parallel} \cdot p_{scale}}{2 \cdot SNR}\right)^2 + \left(\frac{15}{R} \cdot 206{,}265\right)^2} \quad (5.10)$$

where 'px' stands for pixels, $\text{rand}(0.2, 0.5)$ is a random value uniformly chosen between 0.3 and 0.5, and p_{scale} (expressed in arcsec/px) denotes the sensor's pixel scale.

Given the specific parameters of the modeled sensors outlined in Table 4.1, the total calculated angular error ranges between 8.32 to 50.78 arcsec, resulting in σ_{RA} and σ_{DEC} varying between 5.88 and 35.90 arcsec. This calculation assumes that objects are detected at distances between 300 and 800 km with an SNR between 3 and 8, which is often the case. Approximately 20% of the total error can be attributed to parallax error, while the remaining part is roughly split between the other two sources.

5.3 Orbit determination

The steps described in Sections 5.1 and 5.2 allow each image that includes an identified secondary object to be associated with a couple of time-tagged RA/DEC centroid coordinates and corresponding uncertainties. Once these values are collected for each simulated observation within a conjunction scenario, OD processing can be performed to evaluate potential improvements.

OD is the process of estimating the trajectory of celestial objects, including satellites, by fitting observational data to a model. OD methods can be distinguished into three

primary classes: Initial Orbit Determination (IOD), Least Squares (LS), and Sequential Estimation (SE), also known as filtering. Each method differs in its requirements, output, and applicability to various scenarios.

IOD methods are designed to produce an initial orbit estimate without needing any prior data. This is especially useful at the beginning of orbit tracking, where no existing estimates are available. The resulting estimates from IOD can feature significant errors, but the method operates very quickly, allowing rapid initial estimates to be established. Because it lacks prior information, IOD does not support measurement editing, which is a challenge in dealing with data outliers.

Unlike IOD, LS and SE methods require a prior orbit estimate (i.e., position and velocity) as input, with SE additionally needing an initial estimate of the covariance. LS is an iterative approach that minimizes the sum of the squared residuals (differences) between observed and predicted orbital states. This batch processing method takes a set of observational data points all at once to determine the best-fit orbit parameters. It is most effective when a large dataset is available and an optimal solution is desired for a single epoch, but it requires recalculating the whole solution if new data points are added. LS also generates error covariance matrices that, although helpful, are often overly optimistic compared to actual conditions [18].

SE methods process observational data sequentially, updating the estimated orbit with each new observation. They work by predicting the spacecraft's position and velocity at the next observation point and then adjusting this estimate based on the actual observed data. More specifically, the following two steps are performed at each new input observation:

1) Prediction: the filter first predicts the spacecraft's state (position and velocity) at a future time, using the current state and a model of the spacecraft's dynamics, which incorporates any known forces acting on the spacecraft (e.g., aerodynamic drag and known maneuvers),
2) Update: the observation is used by the filter to compare the observed value with the predicted value. The difference, called "residual," between these values is then used to correct the state estimate.

The update step also refines the uncertainty of the state by updating the covariance matrix with each new measurement, starting from the initial input covariance. This covariance adjustment is based on two main sources of uncertainty: process noise and measurement error. The former accounts for the fact that the state could not be propagated exactly during the prediction, as the dynamic model has inherent limitations due to unmodeled or simplified forces. Incorporating process noise allows the filter to adjust and correct the estimated orbit more flexibly as new measurements are integrated. Instead, the measurement uncertainty is the uncertainty in the actual observations, accounting for the limited accuracy of the utilized sensors. These uncertainties must be fed to the filter at each new observation, which is the reason why σ_{RA} and σ_{DEC} are calculated in this work along with the RA/DEC measurements.

It should be noted that the uncertainty derived from the filter provides a realistic estimate only if it the filter is properly tuned and all uncertainties sources in the

dynamic model are accounted for. Overlooking errors or misestimating process noise can result in inaccuracies in the estimated state.

5.3.1 Case studies

Several of the simulated conjunction events discussed in the previous chapters have been further examined by performing OD analyses using the obtained observations. OD processing is conducted here using Ansys' Orbit Determination Tool Kit (ODTK), a comprehensive OD software that conveniently supports integration with STK. Before processing observations for a scenario, all calculated RA/DEC values and associated uncertainties must be formatted into a *.geosc* file, one of ODTK's supported formats for external space-based measurements. The complete description of the format is available at [19].

To process the measurements, SE methods, which continuously update an estimated trajectory with each new observation, are selected for their sequential nature, making them ideal for real-time applications such as the one under consideration. Unlike LS methods, which require reprocessing the entire batch of observations whenever a new one arrives, filters are initialized only once, allowing subsequent runs to start from the state and covariance obtained at the last run.

Particularly, the Extended Kalman Filter (EKF) is considered here, one of the most widely used SE techniques. The original Kalman Filter, as initially formulated, is not suitable for OD because it is only applicable to linear systems [20]. The EKF extends the Kalman Filter to handle nonlinear dynamics by linearizing the dynamical model.

After importing measurements on ODTK, an initial state and covariance matrix are given as input to initialize the EKF. The initial state is derived from the secondary's TLEs at an epoch assumed to represent the last contact with ground, denoted as t_{LGC}. This moment marks the last opportunity for a state update to be sent to the primary, after which it is effectively left on its own to refine the secondary's orbit solution. While the final Go/No-Go decision is generally made around 24 hours—or slightly less—before TCA (see Section 2.1.3), the last ground contact often occurs closer to the event. Here, t_{LCG} is varied between 1 and 10 hours before TCA. Instead, the imported measurements usually fall within 40 to 120 minutes prior to TCA, although earlier observation opportunities may also be available. This is because optimal observation conditions generally lie within that window, as established in Section 4.3.

The initial covariance should represent the uncertainties available at t_{LGC} from the ground and communicated to the primary at that time. Unfortunately, while position and velocity data are readily accessible to operators (e.g., via publicly available TLEs or SP ephemeris through an SSA Data Sharing agreement), uncertainty information is typically not disclosed to the public. Therefore, if operators wish to assess conjunction risk themselves, they must use internal resources if available or, alternatively, adopt realistic values, as is done here for the simulated objects.

The uncertainties screened in Section 3.1—derived from the Kelvins dataset—are not usable for this purpose because their values are already propagated at TCA. The

uncertainties available at t_{LGC} are more likely closer to those available *at epoch*, which refers to the time OD for a space object is done on ground based on fresh observational data. Luckily, a large dataset of Vector Covariance Messages (VCMs) was recently released [21], including position, velocity, and covariance matrix at epoch for space objects as determined by the 18th SDS, based on SSN data. An analysis of those data has been done to derive realistic covariance matrices for initializing the EKF at t_{LGC}. The analysis has focused particularly on fragmentation debris objects, which are tracked less accurately than intact satellites or large rocket bodies. VCMs do not directly provide information on object types, only a universal space object identifier; thus, ESA's DISCOS database, which includes such details, was used to retrieve a list of identifiers for 300 fragmentation debris objects, later used to locate the corresponding VCMs.

For more than 60% of the objects, position and velocity uncertainties are consistently observed to be below 100 m and 0.1 m/s, respectively, for each of the three components. Accordingly, for the simulated objects, the main-diagonal elements of the initial covariance matrix are varied between 0 and 200 m for the position and between 0 and 0.2 m/s for the velocity, with a tendency toward the lower values in each range. Components are specified in the in-track (IT), across-track (CT), and radial (R) directions. Off-diagonal elements are set to zero, having a minor impact on the calculations.

Although the primary's trajectory does not need to be estimated, its ephemeris are still given as input to ODTK, as it is necessary for processing the measurements. In fact, since the measurements were derived relative to a spacecraft-centered ICRF, the primary's position serves as the origin of the coordinate system for correctly using the RA/DEC values.

To propagate orbits in ODTK, which is done by the EKF during the prediction step to estimate the secondary's state at each observation time, the "High Precision Orbital Propagator (HPOP)" is the only available option. HPOP integrates the equations of motion using numerical methods based on a user-configurable list of forces acting on the spacecraft. Adjustable settings include the choice of atmospheric drag models (e.g., CIRA 1972, Jacchia-Bowman 2008, etc.), the number of harmonics in the Earth's gravitational model, and more. HPOP was also the propagator used by STK to generate the "true" secondary trajectory from its SP ephemeris, on which observations were generated. To reflect the primary's imperfect knowledge of the secondary's dynamics, slight deviations are introduced to the HPOP settings in ODTK relative to those in STK. Specifically, parameters such as the drag coefficient, cross-sectional area, and ballistic coefficient are varied within a 1% range. The degree and order of the gravity field model are set to 9×9 in ODTK, while STK used 21×21 degree. Instead, numerical integration is done using the Runge-Kutta-Fehlberg (RKF) 7(8) method both in ODTK and in STK.

The main performance metric investigated is the reduction in position uncertainty achieved after processing observations, although additional insights are presented.

5.3.2 Results

Since the outcomes largely vary based on a few important variables, such as the

initial velocity uncertainties, a representative conjunction event is considered where these variables are tweaked to show their impact on positional uncertainties.

The conjunction occurred between Starlink 1350 and a fragmentation debris from Iridium 33—assumed as the secondary, with an estimated TCA of 01 Jul 2023 20:39:48.805.

A first test is done using sensor #11 from Table 4.3 (aperture: 5-cm, FoV: 15 deg, sensitivity: 0.6) and assuming the secondary's diameter and reflectivity to be 50 cm and 0.175, respectively. With these parameters, one favorable observation window is present half an orbit before TCA, during which 13 observations are collected, with an average estimated SNR of 5.7. Processing the observations yields RA/DEC values with total uncertainties ($\sigma_{tot} = \sqrt{\sigma_{RA}^2 + \sigma_{DEC}^2}$) around 35.4 arcsec. For reference, the sensor's pixel scale is 52.7 arcsec/pixel, calculated by dividing the FoV by the number of pixels in either the vertical or the horizontal direction. OD analysis is then performed using a t_{LGC} value and initial position/velocity uncertainties specified in Table 5.1.

Table 5.1 Fixed parameters of the OD run with outcomes shown in Figure 5.4. Velocity uncertainties are identified by a 'v' subscript

Parameter	Value
Time of last ground contact: t_{LGC}	4 hours before the TCA
Position uncertainties at t_{LGC}: $[\sigma_{IT}, \sigma_{CT}, \sigma_R]$	[100, 20, 40] m
Velocity uncertainties at t_{LGC}: $[\sigma_{v,IT}, \sigma_{v,CT}, \sigma_{v,R}]$	[0.06, 0.02, 0.03] m/s

The results are presented in Fig. 5.4, which compares the evolution of position uncertainty with and without the contribution of space-based observations. As expected, the in-track uncertainty component is the dominant source. After data processing, the in-track and radial components experience a sharp drop, followed by a slower increase. Fig. 5.5 offers further insights into their evolution at the processing times, revealing the so-called 'saw-tooth' pattern. The cross-track component is only slightly improved, almost negligible. At TCA, the total position uncertainty reaches approximately 400 m, compared to about 1.8 km when no observations are used. Notably, the in-track uncertainty drops to around 390 m after the first observation, and improves further to ~150 m thanks to the next 12 observations. As a secondary note, data processing here is simulated at the exact observation times, whereas in real-life scenarios, processing would occur a few moments later. It is assumed that the whole processing workflow can be done within a few minutes at most, though this assumption requires further detailed investigation to confirm its feasibility.

A second test is conducted to assess the impact of varying the time of last ground contact (t_{LGC}), which depends on ground-station access availability for the primary. This test uses the same parameters of the previous one, except for t_{LGC}, which is varied among the following values: 8, 6, 4, 2, and 1 hour(s) before the TCA. The outcomes are illustrated in Fig. 5.6, showing the evolution of total position uncertainty for each case.

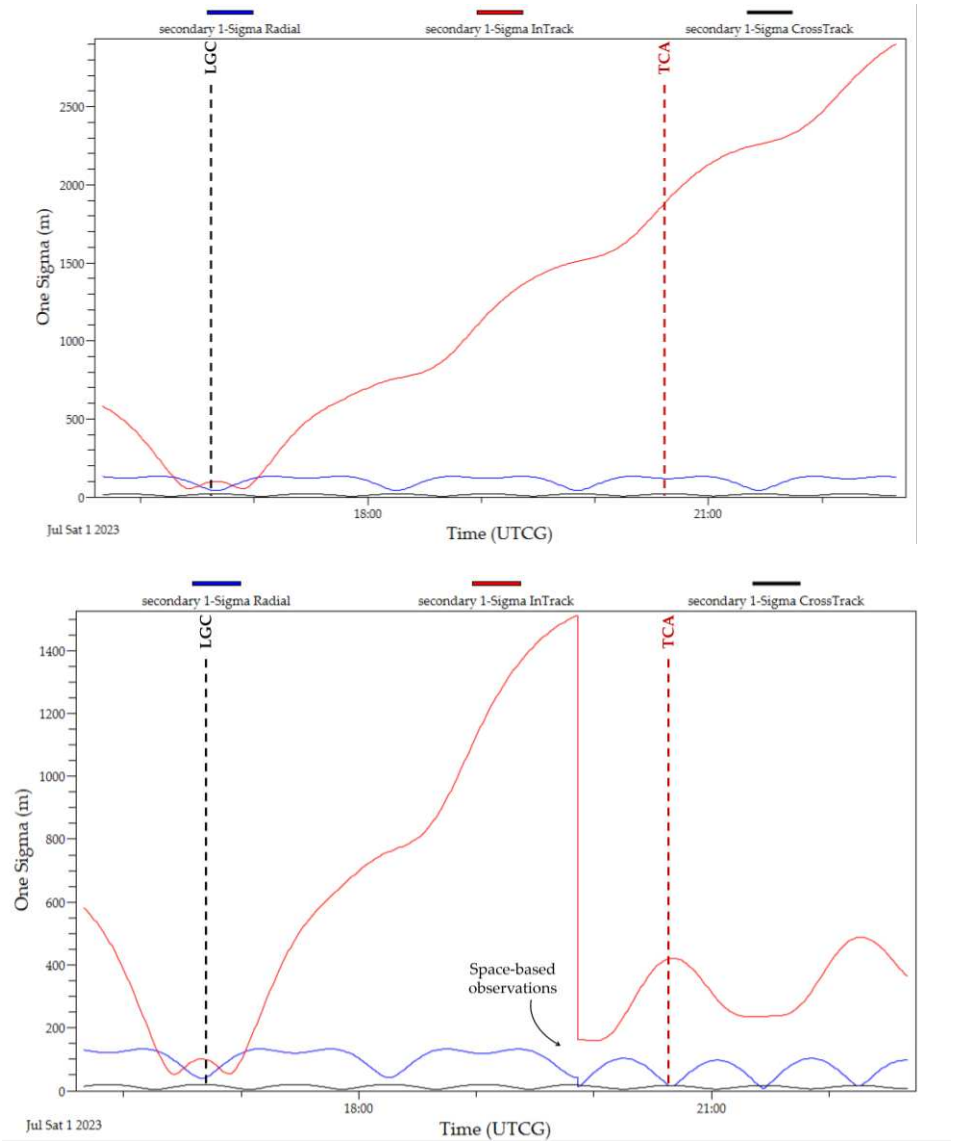

Fig. 5.4 *Top:* natural uncertainty evolution; *bottom*: uncertainty evolution resulting from collecting and processing space-based observations half an orbit before TCA. The time of last ground contact and the TCA are indicated by dashed vertical lines.

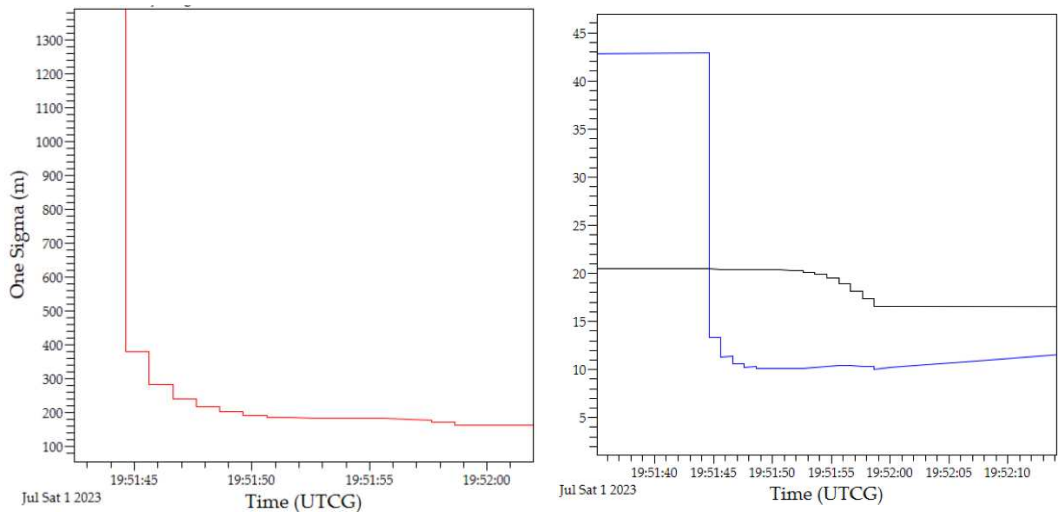

Fig. 5.5 Uncertainty components right after processing the observations

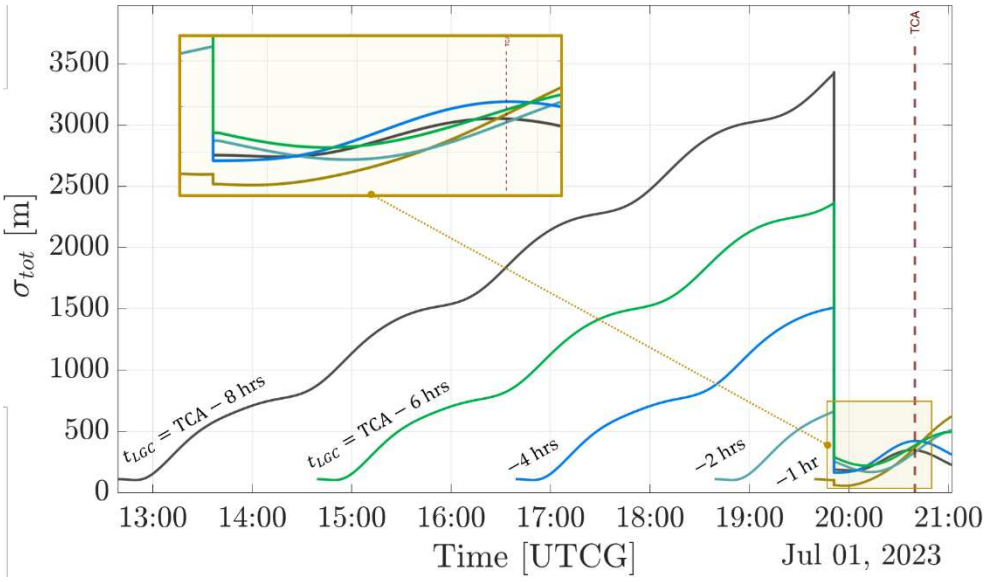

Fig. 5.6 Evolution of the total uncertainty by assuming different possible values of t_{LGC}: [8, 6, 4, 2, 1] hours before the TCA

No evident correlation is observed between t_{LGC} and the achieved accuracy. Although the state initialized 1 hour before TCA results in lower uncertainty right after the observation processing compared to the other cases, the uncertainty values at TCA are similar across all scenarios. In any case, it can be observed that if a good initial state can be uplinked close to the TCA (as in the gold line scenario), the benefits of space-based observations may be almost negligible.

Further tests were conducted by pushing t_{LGC} back even more. In a few cases where t_{LGC} was set to more than one day before TCA, no improvement in uncertainty was recorded after OD processing. This occurred because the filter 'rejected' the input measurements based on its outlier detection mechanism. When measurements exhibit significant deviation from the predicted state, meaning they have large residuals, they are considered as outliers by the filter and excluded to avoid distorting the state estimate. Therefore, sending the last state too early to the primary carries the risk of the state becoming outdated and deviating significantly from the true trajectory of the secondary. This complicates both OD processing and the recognition of the secondary in images, as the bright pixels may appear too far from their expected position, reducing confidence in the association process.

The impact of the sensor's accuracy —represented by its pixel scale —is evaluated next. The considered conjunction is simulated three times on STK by using sensors #10, #11, and #12. The sensors are all identical except for their FoV, which is 10, 15, and 20 degrees, respectively, resulting in different pixel scales. On average, measurement uncertainties obtained for the observations resulting from three sensors are around 5, 25, and 48 arcsec, respectively. Figure 5.7 presents the results after OD processing.

Interestingly, although sensor #11 has a worse resolution than sensor #10, it achieves a better uncertainty immediately following observation processing. However, this improvement is only temporary, as the three uncertainty curves later evolve to reflect their respective sensor accuracies. At TCA, the positional uncertainty

obtained with sensor #10 is more than 200 meters better than that achieved with sensor #12, underscoring the importance of high-accuracy detectors.

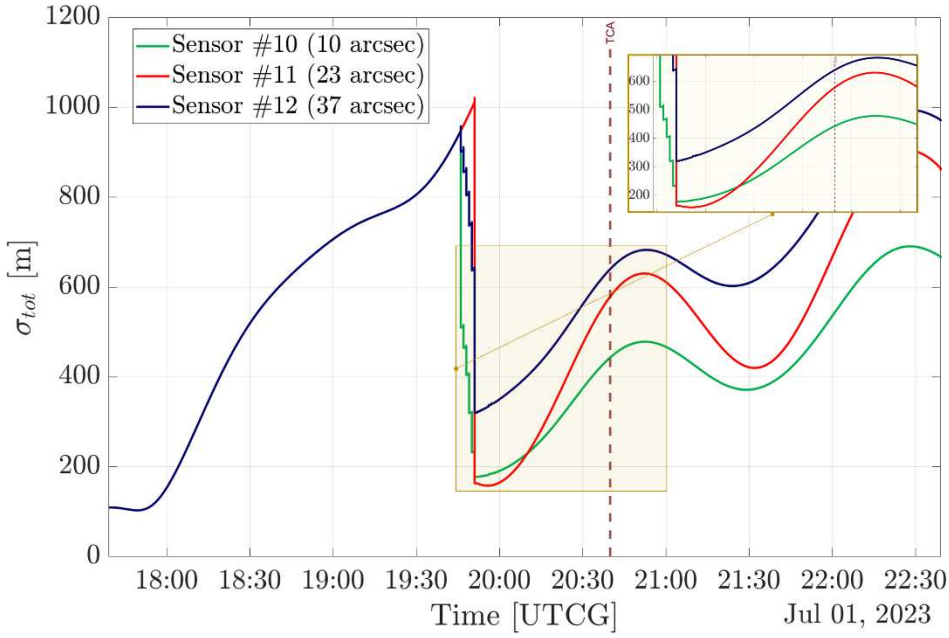

Fig. 5.7 Evolution of σ_{tot} by processing observations from differently accurate sensors. The legend reports the average uncertainty in the obtained observations

However, achieving high sensor's accuracy often comes at the expenses of sensitivity. In this context, it is interesting to examine the OD performance of sensors #16 and #18 for the same conjunction, which is shown in Fig. 5.8. These sensors have the same parameters as sensors #10 and #12, respectively, but with a larger aperture. Although sensor #18 is less accurate than sensor #16, it has a larger FoV, making it inherently more sensitive to dimmer objects. In this case, this property enables sensor #18 to detect the secondary object also 1.5 orbits before TCA, allowing the primary to collect and process additional observations.

While the single tracklet[10] from sensor #16 still provides more accurate estimates at TCA than the two tracklets from sensor #18, it is noteworthy that the two solutions are much closer than those obtained with sensors #10 and #12 (see Fig 5.7), highlighting the benefit of the second observation window.

Further insights into the impact of the number of observations can be gained by evaluating the performance of sensor #24, which is identical to sensor #18 but has a larger aperture. Due to the increased aperture, a third observation opportunity becomes available between the two previously used by sensor #18, occurring one orbit before TCA, as shown in Fig. 5.8. OD processing of this additional data results in the lowest uncertainty at TCA.

On one hand, the availability of three tracklets instead of two seems enough to justify

[10] In SSA terminology, a *measurement* is a single data point (e.g., RA, DEC, Azimuth) from a sensor, an *observation* is a set of measurements from the same sensor at one time (e.g., a RA/DEC couple from a telescope), whereas a *tracklet* (or *track*) is a sequence of closely spaced observations

the increased filter's confidence in the state estimate. However, further analysis suggests that the reason may be more closely related to the timing of the observations rather than their quantity.

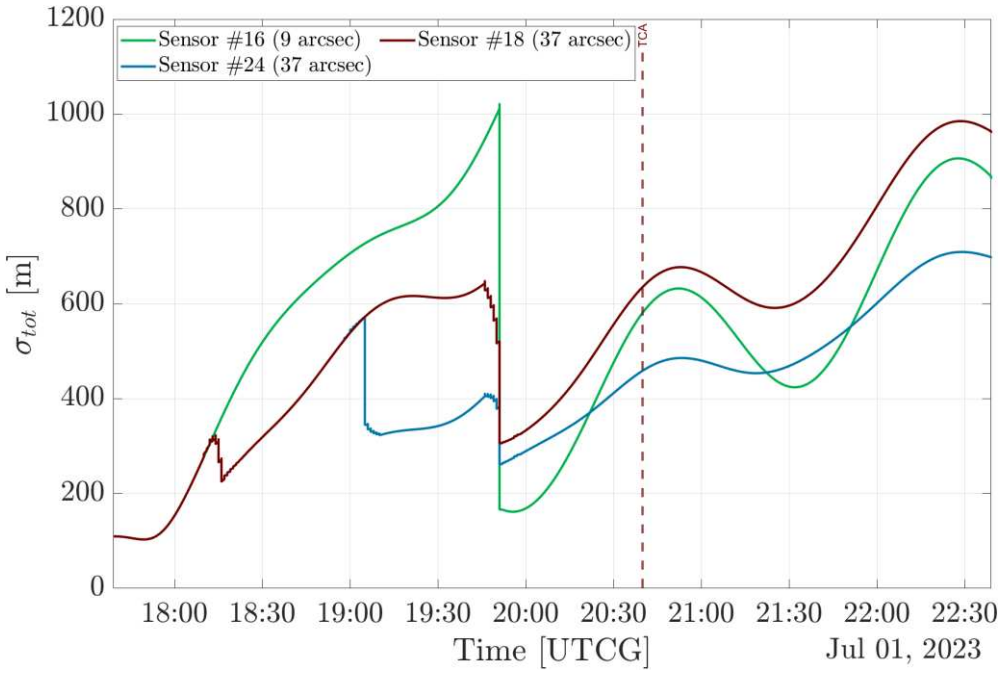

Fig. 5.8 Positional uncertainties for sensors #16, #18, #24. The legend reports the average uncertainty in the obtained observations

To verify this hypothesis, the reflectivity of the secondary is temporarily raised to 0.5, allowing the object to be visible many times before the TCA. Using sensor #18 again, observations are collected during all available opportunities during the three orbits leading up to the TCA. Then, tests are conducted by processing only a few of these tracklets to assess their individual contributions to the overall solution.

Figure 5.9 shows the differences in positional uncertainty when processing three tracklets collected at 0.5, 1.5, and 2.5 orbits prior to TCA, compared to processing two tracklets at 0.5 and 1 orbit(s) before TCA. As evident from the figure, the solution obtained from two tracklets is more accurate than the one obtained from three. This improvement is likely because the two-tracklet solution includes observations at different orbital points, whereas the three-tracklet solution uses data from nearly the same orbital node. As explained in [22], when SSA observations of an object are clustered near the same orbital point, they provide limited information to constrain the orbit's tangential uncertainty, as there will be multiple orbits with different eccentricities that can fit those observations well. Conversely, observations taken from different orbital points better constrain the orbit solution space, thereby enhancing the accuracy of the OD solution. As established in Section 4.3, around 49% of the events conveniently feature favorable visibility conditions at two opposite orbital points.

Using once again the same conjunction event and sensor #11, the impact of different initial positional and velocity uncertainties is evaluated. Figure 5.10 illustrates the evolution of σ_{tot} for three values of the initial velocity uncertainty, which are

specified in Tab. 5.2.

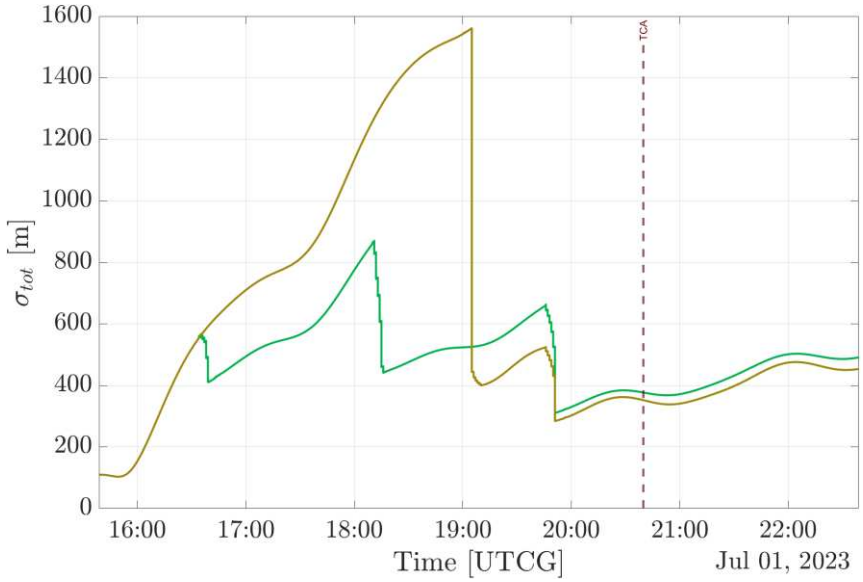

Fig. 5.9 Difference between the positional uncertainty achieved by processing three tracks collected at the same orbital point (*green line*) or two tracks at different nodes (*gold line*)

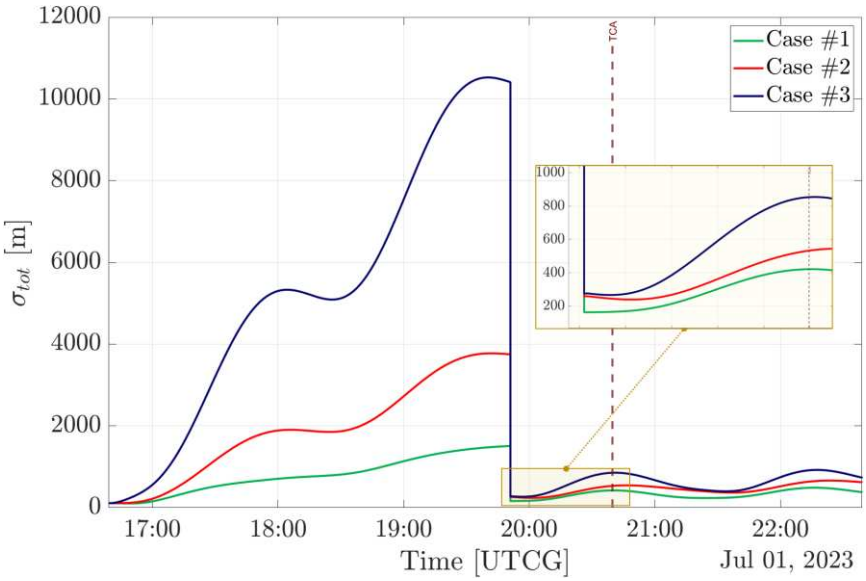

Fig. 5.10 Impact of different initial velocity uncertainties

Table 5.2 Values of velocity uncertainty components across three cases, with outcomes shown in Fig. 5.10

Parameter	Case #1	Case #2	Case #3
$\sigma_{v,IT}$ [m/s]	0.06	0.1	0.3
$\sigma_{v,CT}$ [m/s]	0.02	0.02	0.1
$\sigma_{v,R}$ [m/s]	0.03	0.04	0.2

As it can be seen, initial velocity uncertainties have a significant impact on σ_{tot}, with this effect intensifying as the propagation time increases. Nevertheless, processing

space-based observations always improves positional uncertainties at TCA, with improvement factors ranging from 5 to 13 compared to the cases with no observations.

Figure 5.11 illustrates the impact of initial positional uncertainties, showing results for the same conjunction but assuming three different sets of initial uncertainties.

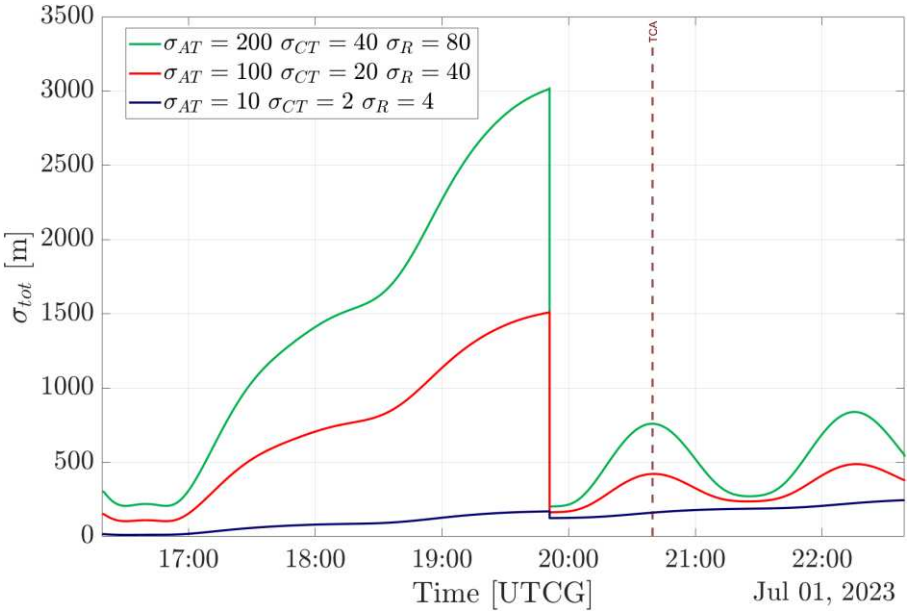

Fig. 5.11 Impact of different initial positional uncertainties, with specific values reported in the legend

In this case as well, improvements are observed across all scenarios, although they are quite limited for the one with best positional uncertainties. This latter case represents the uncertainties that may be available for a secondary object that is an active satellite, suggesting that sensor #11—along with all simulated sensors with the same pixel scale (52.7 arcsec/pixel)—may be ineffective for such objects. Considering the recent rise of mega-constellations, active-active conjunctions will become more frequent, so the system must be designed to deliver improvements for well-tracked objects as well. To this end, it is believed that a pixel scale finer than 40 arcsec/pixel is necessary for the onboard sensor to ensure meaningful improvements across different objects. However, it should be noted that this recommendation derives from assuming a coordinate fit uncertainty ($\sigma_{starfit}$) ranging between 0.2 and 0.5. A more robust system guideline, avoiding reliance on such assumptions, would specify that the system—regardless of pixel scale—should achieve a total measurement error σ_{tot} of better than 15 arcsec in all cases, whereas sensor #11 achieved ~30-40 arcsec. This level of resolution can be achieved either by using sensors with FoVs no larger than 10×10 degrees on 1024×1024 detectors —though this comes at the expense of SNR—or by improving the precision of coordinate fit solutions and centroiding algorithms. Prioritizing the latter approach is advisable, given the significant advantages in detection rates offered by a relatively wide FoV, as highlighted in Figs. 4.10–4.13.

References

[1] S. D'Amico, J.-S. Ardaens, G. Gaias, H. Benninghoff, B. Schlepp, "Noncooperative rendezvous using angles-only optical navigation: system design and flight results," *Journal of Guidance, Control, and Dynamics*, vol. 36, no. 6, 2013, pp. 1576-1595, doi: https://doi.org/10.2514/1.59236

[2] D. Lang, D. W. Hogg, K. Mierle, M. Blanton, S. Roweis, "Astrometry.net: blind astrometric calibration of arbitrary astronomical images," *The Astronomical Journal*, vol. 139, 2010, pp. 1782–1800, doi: https://doi.org/10.1088/0004-6256/139/5/1782

[3] D. Monet, S. Levine, B. Canzian, H. Ables, A. Bird, C. Dahn, H. Guetter, H. Harris, A. Henden, S. Leggett, H. Levison, C. Luginbuhl, J. Martini, A. Monet, J. Munn, J. Pier, A. Rhodes, B. Riepe, S. Sell, R. Stone, F. Vrba, R. Walker, G. Westerhout, R. Brucato, N. Reid, W. Schoening, M. Hartley, M. Read, S. Tritton, "The USNO-B catalog," *The Astronomical Journal*, vol. 125, no. 2, 2003, pp. 984–993, doi: https://doi.org/10.1086/345888

[4] NASA's Navigation and Ancillary Information Facility (NAIF), "An overview of reference frames and coordinate systems in the SPICE context," Accessed Nov 3, 2024. [Online]. Available: https://naif.jpl.nasa.gov/pub/naif/toolkit_docs/Tutorials/pdf/individual_docs/17_frames_and_coordinate_systems.pdf

[5] R. L. Scott, B. Wallace, D. Bedard, "Space-based observations of satellites from the MOST microsatellite," Defence R&D Canada, Ottawa, Canada, Tech. Rep. TM 2006-199, 2006

[6] X. Wei, W. Tan, J. Li, G. Zhang, "Exposure time optimization for highly dynamic star trackers," *Sensors*, vol. 14, no. 3, 2014, pp. 4914-4931, doi: https://doi.org/10.3390/s140304914

[7] J. E. Postma, D. Leahy, "An algorithm for coordinate matching in world coordinate solutions," Publications of the Astronomical Society of the Pacific, vol. 132, no. 1011, 2020, 054503, doi: https://doi.org/10.1088/1538-3873/ab7ee8

[8] E. Andreis, P. Panicucci, F. Topputo, "An image processing pipeline for autonomous deep-space optical navigation," *arXiv online repository*, 2023, doi: https://doi.org/10.48550/arXiv.2302.06918

[9] C. von Braun, J. Sharma, E.M. Gaposchkin, "Space-Based Visible metric accuracy," *Journal of Guidance, Control and Dynamics*, vol. 23, no. 1, 2000, pp. 175-181, doi: https://doi.org/10.1016/10.2514/2.4508

[10] J. Enright, D. Sinclair, T. Dzamba "The things you can't ignore: evolving a sub-arcsecond star tracker," in *26th AIAA/USU Conference on Small Satellites*, Logan, UT, USA, 2012

[11] G. Rufino, D. Accardo, "Enhancement of the centroiding algorithm for star tracker measure refinement," *Acta Astronautica*, vol. 53, no. 2, 2002, pp. 135-147, doi: https://doi.org/10.1016/S0094-5765(02)00199-6

[12] G. A. Finney, S. Fox, B. Nemati, P. J. Reardon, "extremely accurate star

tracker for celestial navigation," in *Advanced Maui Optical and Space Surveillance Technologies Conference (AMOS)*, 2023

[13] G. Borghi, D. Procopio, M. Magnani, S. Pieri, S. Becucci "Stellar reference unit for CASSINI mission," in *Proc. SPIE 2210, Space Optics 1994: Space Instrumentation and Spacecraft Optics*, 1994, doi: https://doi.org/10.1117/12.188076

[14] D. G. Monet, J. M. Jenkins, E. W. Dunham, S. T. Bryson, R. L. Gilliland, D. W. Latham, W. J. Borucki, D. G. Koch, "Preliminary astrometric results from Kepler," in *arXiv online repository*, 2010, doi: https://doi.org/10.48550/arXiv.1001.0305

[15] N. Kaiser, J. L. Tonry, G. A. Luppino, "A new strategy for deep wide-field high-resolution optical imaging," *Publications of the Astronomical Society of the Pacific*, vol. 112, no. 772, 2000, pp. 768-800, doi: https://dx.doi.org/10.1086/316578

[16] I. R. King, "Accuracy of measurement of star images on a pixel array," *Publications of the Astronomical Society of the Pacific*, vol. 95, no. 564, 1983, pp. 163-168, doi: https://dx.doi.org/10.1086/131139

[17] US Department of Defense (DoD), "Global Positioning System standard positioning service performance standard," US DoD, Washington, DC, USA, Tech. Rep. GPS SPS PS, 5th ed., 2020. Accessed Nov 5, 2024. [Online]. Available: https://www.gps.gov/technical/ps/2020-SPS-performance-standard.pdf

[18] J. R. Wright "Orbit Determination Tool Kit: theory & algorithms," Analytical Graphics, Inc. (AGI), Exton, Pennsylvania, USA, Tech. Rep., 2020

[19] ODTK Help, "GEOSC format," Accessed Nov 7, 2024. [Online]. Available: https://help.agi.com/odtk/index.htm#od/ODObjectsGEOSCFormatType.htm?Highlight=SBV

[20] E. Gamper, C. Kebschull, E. Stoll "Statistical orbit determination using the ensemble Kalman filter," in *1st NEO and Debris Detection Conference*, Darmstadt, Germany, Jan 2019

[21] G. Lavezzi, P. M. Siew, D. Wu, Z. Folcik, V. Rodriguez-Fernandez, J. Price, R. Linares, "Early classification of space objects based on astrometric time series data," in *25th Advanced Maui Optical and Space Surveillance Technologies Conference (AMOS)*, Maui, Hawaii, USA, Sep 2024

[22] J. Siminski, T. Flohrer, T. Schildknecht, "Assessment of post-maneuver observation correlation using short-arc tracklets," in *7th European Conference on Space Debris*, Darmstadt, Germany, 2017

Chapter 6

Towards ground testing and on-orbit demonstration

6.1 Planning software development and on-ground testing

Following feasibility studies, the next step is to design and develop the software infrastructure required to functionalize on-board hardware for the desired avoidance purposes. Several processing modules — such as orbital propagation and astrometric reduction — have already been covered partially during feasibility studies; however, further work is necessary to optimize their implementation in support of real-time decisions and to integrate them within a unified software architecture. All system functionalities must then be tested on the ground under realistic environmental conditions to identify potential issues before in-orbit deployment and to better characterize expected system performance.

The initial planning of these two activities—software development and on-ground testing—along with the preliminary setup design, is outlined in this thesis, laying the foundation for future work. The two activities are planned to run concurrently, creating a feedback loop whereby design refinements are informed by on ground test outcomes, and vice versa.

Concerning the software, a modular structure will be adopted to optimize onboard computational resources. A preliminary definition of each module, including its inputs and outputs, is provided in Table 6.1.

The activities are organized into five approximately sequential phases:

1. development of the OBSWIN and IMPRO software modules,
2. open-loop testing with the sensor,
3. development of the remaining software modules,
4. definition of the hardware architecture for on-board processing,
5. closed-loop testing with the sensor and System-on-Chip (SoC).

OBSWIN and IMPRO modules are developed first because of the higher research effort they require. IMPRO includes image-processing algorithms to convert raw sensor data into usable measurements for OD, while OBSWIN handles planning in-orbit observation campaigns, including timings and pointing angles. IMPRO's development requires extensive algorithm tuning, while OBSWIN demands a more detailed investigation into the observation strategy beyond what has been covered in this thesis. Algorithms will first be developed in MATLAB/Simulink, which provide the flexibility needed in this phase for algorithm optimization.

Table 6.1 Onboard software modules

Acronym	Inputs	Outputs
PROP	_ Orbital state of an object at time t_0 or ephemeris _ Desired epoch t_1 _ Force model parameters	_ State of the object at time t_1
OBSWIN	_ Propagated states or ephemerides (output from PROP)	_ Observation plan (time-tagged pointing angles and exposure time)
ATCOM	_ Observation plan	_ Attitude maneuver command
IMPRO	_ Raw sensor images	_ Bright pixels of non-stellar objects _ Outcome of the observation association process _ Time-tagged RA/DEC, σ_{RA}, σ_{DEC} for the secondary (if associated)
OD	_ Secondary's state and covariance _ Time-tagged RA/DEC, σ_{RA}, σ_{DEC} _ Primary's state and covariance _ GNSS data for the primary	_ Refined orbital state (or ephemeris) for the primary _ Refined orbital state (or ephemeris) for the secondary
COLA	_ Primary's state _ Secondary's state	_ Collision assessment report _ Go/No-Go maneuver decision
CAMDES	_ Collision assessment report _ Go/No-Go decision	_ Planned maneuver
CAMCOM	_ Planned maneuver	_ Maneuver command

An open-loop test, whose setup is shown in Fig. 6.1, will validate IMPRO using a real star tracker in a darkroom. The setup includes a star tracker with a 2 cm aperture and 15×15° circular field of view. The sensor will capture simulated celestial scenes including transient debris projected onto a high-resolution screen. which offers high contrast suitable for celestial scenes. Following [1], an OLED screen is selected because does not suffer from the bleeding issues typical of LCDs and offers high contrast, ideal for rendering deep black celestial backgrounds.

To isolate the setup from vibrations, the experimental assembly will be mounted on an optical bench supporting the monitor and a horizontally mobile mount. An optical collimator placed in front of the star tracker will simulate starlight from

virtually infinite distances. Images displayed on the screen will be generated by a computer running STK, which simulates orbital dynamics and generates synthetic images via EOIR. Unlike the images generated in Section 4.1.4, the EOIR output here will be set to "Radiometric Input," simulating photons reaching the sensor before lens and radiometric processing. A second computer connected to the star tracker will store and process images offline via IMPRO.

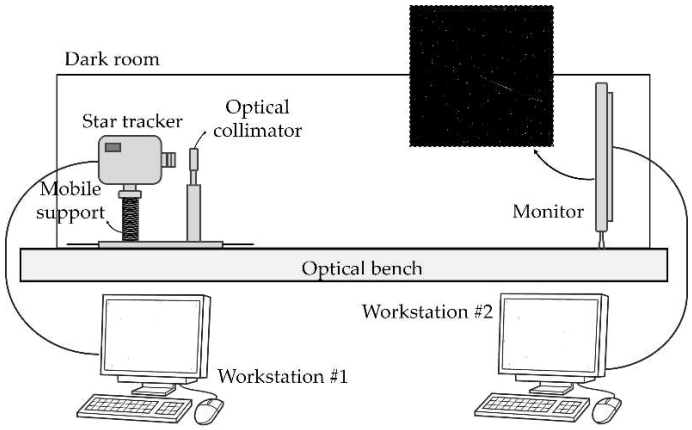

Fig. 6.1 Experimental setup for the open-loop test. The setup is inspired by that described in [2], later used by several authors for similar tests, such as [1].

In the next phase, the remaining software modules—PROP, ATCOM, OD, COLA, CAMDES, and CAMCOM—will be developed. Unlike IMPRO and OBSWIN, these modules require less research as they are based on well-established methods like OD techniques and conjunction assessments.

Simultaneously, a SoC will be selected to implement both the whole software of Table 6.1 and an "Integrated Onboard Simulator" (IonS), which emulates the behavior of satellite's onboard systems. Before implementing the software, all codes will be converted to hardware description languages (HDL) like VHDL or Verilog. For IonS, the aerospace company 'Planetek' will supply "SpaceKit," an onboard data processing framework that allows access to core satellite resources such as GPS, attitude data, onboard time, and more. SpaceKit offers an abstraction layer for platform data and acquisition sensors, as well as higher-level library functions for data processing and operations.

A final closed-loop test will fully validate the integrated software on the SoC. The setup mirrors the open-loop test, but Workstation #1 is replaced by the SoC, now connected to the star tracker and Workstation #2, which generates synthetic scenes, thus closing the loop. All satellite operations will be managed at the SoC level, including issuing image acquisition commands to the star tracker and sending attitude adjustment commands to Workstation #2, which will update the dynamics accordingly. This configuration allows the end-to-end system to simulate operations across various collision scenarios.

6.2 In-orbit demonstration mission

A small budget In-Orbit Demonstration (IOD) mission is hypothesized to partially validate the autonomous system's capabilities. A 3U CubeSat in LEO equipped with

an electro-optical payload is proposed, with the goal of demonstrating the extent to which a satellite can autonomously acquire optical tracking data on hazardous objects during the lead-up to the TCA. Findings from this IOD would be essential for refining and optimizing the system's design and operation.

This section provides a description of the conceived mission and a preliminary selection of the Cubesat's orbit.

6.2.1 Mission description

The Cubesat shall be equipped with either a star tracker or a small camera to attempt observations of objects predicted for oncoming close approaches. The Concept of Operations (ConOps) envisions the satellite receiving daily updates of TLEs for all objects predicted to approach within a 10 km radius of its position over the following 24 hours. Such orbital information must be propagated onboard to identify favorable visibility opportunities and schedule observation plans. A subset of images would be compressed, while others would undergo minimal onboard and downlinked at the earliest available ground-station access. Ground-based processing of these data would assess the OD improvements resulting from the acquired images. Additionally, compressed images would be further analyzed to explore potential enhancements in IP onboard processing to extract Regions of Interest (ROIs)—defined as small rectangular sections of pixel values around bright sources. ROIs and compressed images must be stored detection algorithms and observation strategies.

As part of its high-level requirements, the mission shall comply with ESA's Space Debris Mitigation Requirements "ECSS-U-AS-10C Rev.1" [3].

The following points outline the primary functions that the satellite is expected to perform and provides a preliminary draft for deriving the mission's operational and functional requirements:

- Image acquisition: The spacecraft shall capture images of at least 1,000 objects predicted to come within 10 km in less than 24 hours. For each target, it shall attempt at least two observations, provided that favorable visibility conditions are available. The two attempts shall be spaced at least 10 minutes apart, with the last attempt occurring no later than 30 minutes prior to the TCA. The spacecraft shall capture a minimum of six images of the target object in rapid succession (exact timing to be defined (TBD)), following the observation strategy outlined in Section 4.1.3. The payload shall generate acquisition timestamps for each image with an accuracy better than 1 μs.
- Data processing: the spacecraft shall be capable of both extracting ROIs and compressing raw images. The spacecraft shall be able to: 1) propagate both its orbital state and that of the target objects, 2) schedule observation plans, including the definition of a timeline and the sensor pointing directions, 3) generate attitude control commands to according to the planned observation schedule. The onboard software shall also feature reconfiguration capabilities, to allow for updates in the observation strategy.

- Data transmission: the spacecraft shall downlink time-tagged ROIs, compressed images, and telemetry data to the ground. The spacecraft shall also be able to receive command data and orbital information (current specification: TLEs) on the target objects.
- Navigation: the spacecraft shall be able to autonomously determine its position in real-time when performing observation scheduling activities.

Additional requirements, not explicitly mentioned, concern usual subsystem functions such as generating and storing electrical energy or ensuring an appropriate thermal environment.

6.2.2 Operational orbit

A preliminary operational orbit is selected by accounting for multiple factors, including subsystem design and constraints. The analysis starts by considering orbital regions that ensure frequent observation opportunities for the satellites, which requires the mission to target populated orbits. Figure 6.2 shows the spatial density of space debris for different altitudes and declinations in LEO, obtained using ESA's MASTER 8.0.3 debris environment model. In the simulation, objects larger than 5 cm are considered, given that the space-based observations targets objects already identified from ground-based sensors, whose current detection capabilities are limited to minimum object sizes of approximately 5-10 cm.

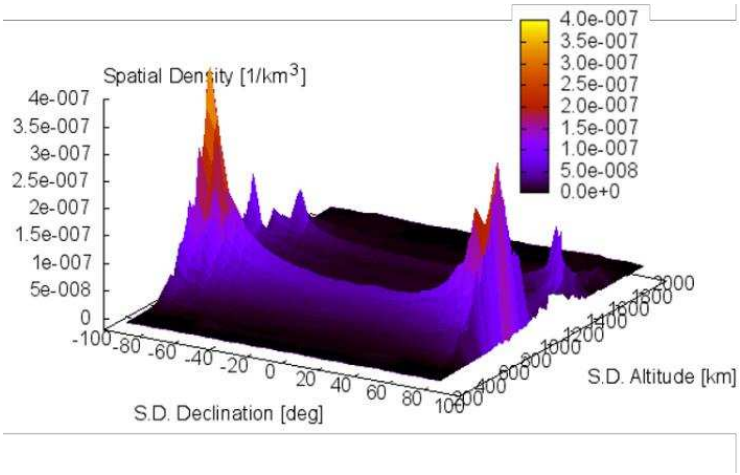

Fig. 6.2 Spatial density of debris objects > 5 cm in LEO [4]

Polar orbits at altitudes of around 800 km appear to be the most congested with debris. However, the debris mitigation requirements force the satellite to de-orbit within 25 years after the end of its lifetime, imposing an upper limit to the feasible altitudes. Figure 6.3 shows an estimation of the natural decay times for a 3U Cubesat at different altitudes. The analysis has been made by using the model of altitude reduction due to drag reported in [5] and by considering a drag coefficient c_D of 2.2, average solar activity, and a cross-sectional area of 0.01 m² exposed to the air flux (worst-case for a 3U CubeSat).

Given the multiple sources of uncertainty affecting decay times estimations, altitudes approximately lower than 550 km should be targeted to comply with the 25-year policy. Employing a propulsion engine for actively de-orbiting the CubeSat has been considered, but ultimately deemed not convenient due to SWaP

limitations. Although the debris requirement prevents targeting the most debris-populated regions, it should be noted that altitudes around 450 – 550 km are the most crowded with active payloads, as reported in ESA's 2023 Annual Space Environment Report [6]. SpaceX's "Starlink" constellation contributes particularly to the statistics, counting more than 6,400 satellites distributed in different orbital planes at around 540 km as of September 2024 [7]. Since the avoidance system is intended for generic hazardous objects, both payloads and debris objects are potentially good targets for the observations. Moreover, given the rapidly accelerating launch rates in LEO, risky conjunctions between active satellites are becoming always more common.

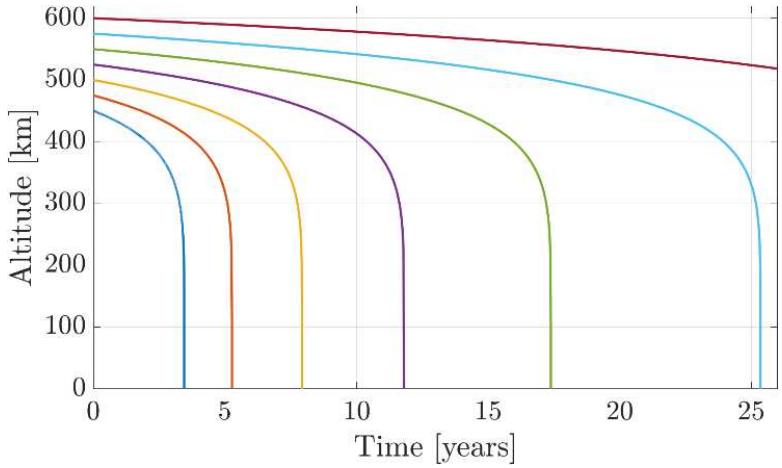

Fig. 6.3 Estimated orbital decay times for a 3U Cubesat [4]

The orbit preliminarily chosen for the mission is a circular one at an altitude of 535 km, which ensures regular observation opportunities with the Starlink satellites while avoiding risky close approaches. The decision to opt for a null eccentricity is based on the analysis of Section 3.2.2, which has evidenced that repeated encounters between potentially colliding objects occur as far as their orbits are nearly circular with similar radii. Additionally, circular orbits are popular targets of piggyback launch opportunities.

The remaining orbital parameters are selected to obtain a dusk-dawn Sun-Synchronous Orbit (SSO), which is shown in Fig. 6.4. This choice follows several considerations regarding the relative positioning of the spacecraft with respect to the sunlight, which affects the illumination conditions during the encounters as well as the onboard solar power generation. Dusk-dawn orbits minimize eclipse time, during which orbiting objects would be generally invisible to onboard optical sensors. Then, the SSO choice ensures that the dusk-dawn condition – alignment of the orbit with the terminator line – is met throughout time. Furthermore, the dusk-dawn SSO allows an easier fulfilment of the type of pointing required for the observations. Specifically, as established in Section 3.2.4.5, elevation angles of hazardous objects with respect to the spacecraft's local horizon plane takes on values of about -10° when the relative distances are still > 1500 km, then it gradually reaches 0° as the objects advance further. Instead, the azimuth angles exhibit a broader range of values, but their distribution is notably skewed towards 0° (or 360°). It is concluded that aligning the CubeSat's sensor axis in the direction of motion and with

a slightly negative elevation (e.g., -5°) would minimize the slew maneuvers required before the observation attempts. Keeping such pointing direction while in a dusk-dawn SSO conveniently allows the Sun to fall always outside the sensor's FoV, fulfilling any requirements on solar exclusion angles.

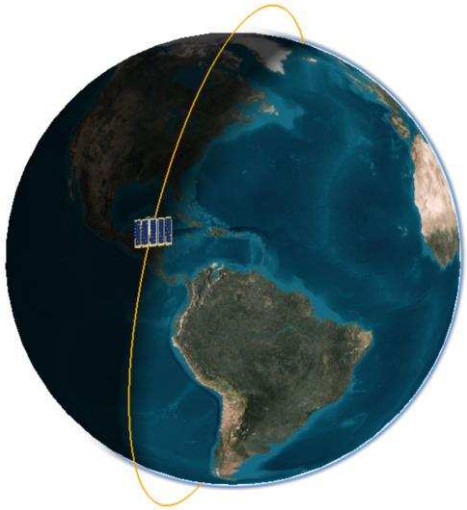

Fig. 6.4 Selected dusk-dawn SSO

References

[1] P. Panicucci, F. Topputo, "The TinyV3RSE hardware-in-the-loop vision-based navigation facility," *Sensors*, vol. 22, 2023, doi: https://doi.org/10.3390/s22239333

[2] G. Rufino, D. Accardo, M. Grassi, G. Fasano, A. Renga, U. Tancredi, "Real-time hardware-in-the-loop tests of star tracker algorithms," *International Journal of Aerospace Engineering*, 2013, 505720, doi: https://doi.org/10.1155/2013/505720

[3] European Cooperation for Space Standardization (ECSS), "Adoption notice of ISO 24113: space systems – space debris mitigation requirements," European Space Research and Technology Centre (ESTEC/ESA), Noordwijk, Netherlands, Tech. Rep. ECSS-U-AS-10C Rev.1, 2019. Accessed: Oct 26, 2024. [Online]. Available: https://ecss.nl/standard/ecss-u-as-10c-adoption-notice-of-iso-24113-space-systems-space-debris-mitigation-requirements-2/

[4] G. Campiti, G. Brunetti, C. Ciminelli, "A 3U Cubesat mission to image potentially colliding objects," in *Small Satellite Systems and Services (4S) Symposium*, Palma de Mallorca, Spain, May 27-31, 2024

[5] J.R. Wertz, W.J. Larson, *Space mission analysis and design*, Space technology library. Microcosm, 1999. ISBN: 9781881883104

[6] European Space Agency, "ESA's Annual Space Environment Report", ESA Space Debris Office, Darmstadt, Germany, Tech. Rep. GEN-DB-LOG-00288-OPS-SD, 2023

[7] Space.com, "Starlink satellites: facts, tracking and impact on astronomy," Accessed Oct 26, 2024. [Online]. Available: https://www.space.com/spacex-starlink-satellites.html

Chapter 7

Conclusions

The thesis presented a feasibility analysis of an oboard payload designed for the self-protection of satellites operating in LEO. The system exploits onboard sensors to make observations of hazardous objects during orbits prior to the TCA, refining their trajectory estimates up until shortly before the TCA.

Following a system engineering approach, system requirements were derived first. Given the innovative nature of this concept, deriving requirements, such as the sensor's detection range and the duration of available observation windows, required an in-depth study of the orbital dynamics of conjuncting objects in LEO. Findings indicated that conjuncting objects in LEO frequently perform several close passes before a potential collision, providing multiple short arcs for potential observation. The repeated proximity is a result of similar orbital periods and nearly circular orbits, where objects typically meet twice per orbit at opposite nodal intersections. For a small subset of conjunctions (< 1%), objects exhibit considerably different orbital eccentricities, resulting in no observation opportunities.

The study also reveals that 70% of conjuncting objects pass within 100 km and 90% within 300 km of each other in orbits leading to the TCA. However, high angular rates at such proximities limit continuous observation within the sensor's FoV. By setting a limit angular rate of 1°/s, it is shown that an onboard sensor a having detection range of 500–600 km see around 90% of secondary objects with at least one 10-second observation opportunity before TCA.

Following this characterization, a review of existing technologies—including radar, LiDAR, and optical cameras—guided the establishment of specific sensor requirements. Electro-optical sensors emerged as the most feasible option, prompting a detailed parametric study to optimize sensor performance. Using a Matlab–STK modeling environment, various conjunction scenarios were reconstructed by modeling space-based observations between the objects. Synthetic images of approaching objects were analyzed to evaluate SNR and detection probabilities across different sensor types and sizes. A detailed observation strategy was outlined, which uses an analytical model of the expected SNR to find a favorable time for making observations.

Regarding visibility conditions—such as proper Sun illumination, a solar exclusion angle, and elevation above the Earth's limb—simulations showed that in nearly 50% of cases, conjuncting objects have one good observation opportunity per orbit at the

same orbital node. Of the remaining 50%, around 49% exhibit two observation opportunities per orbit at roughly opposite orbital nodes, while approximately 1% of cases have no viable opportunities, corresponding to events involving objects with differing eccentricities, as already identified in the orbital dynamics study.

Sensor-wise, small star trackers, such as those with a 2-cm aperture, are insufficient for reliable detection of 1-meter objects (detecting only 25-30%), although they identify larger secondaries (> 2 meters) in many situations. In contrast, larger sensors (5 cm and above) demonstrated consistent detection of objects over 1 meter, suitable for use in densely populated orbital regions.

While increasing aperture sizes above 10 cm enables detection of smaller objects (down to 20-40 cm), such sensors are realistically too large for common platforms. In the future, prioritizing high-quality electronics in smaller sensors—focusing on minimizing noise factors like σ_{rn}—is essential to achieve effective autonomous collision avoidance on small satellites.

The thesis also evaluated potential OD improvements resulting from processing space-based observations. Key steps in this analysis included using plate-solving tools for deriving transformations from pixel to celestial coordinates (RA/DEC) and conducting an error budget analysis to generate realistic measurement uncertainties to be associated with target's centroid coordinates. For debris tracked at current accuracy levels, almost all simulated sensors can contribute to OD improvements, provided the target is successfully detected. However, for more accurately tracked objects, such as active satellites, the total uncertainty achieved by the sensing system should be below 15 arcsec. This requirement is estimated to correspond to a sensor pixel scale finer than 40 arcsec/pixel.

Observation timing has a significant impact on accuracy. The availability of tracklets acquired from different orbital points (as opposed to closely clustered observations) yields much better OD results, as it more effectively constrains the orbit solution space. Fortunately, as previously noted, approximately half of conjunction events in LEO offer two visibility windows at opposite orbital intersections.

Finally, some considerations were offered on non-technical aspects of the proposed system, including potential conflicts during high-risk events involving active satellites. This discussion supports the view that, despite the autonomous nature of the system, maneuver decision authority (i.e., whether the satellite can make the Go/No-Go decision) should be communicated from the ground after coordination with other involved operators.

The findings in this thesis lay essential groundwork for advancing the proposed autonomous collision avoidance system. Although significant progress has been made, challenges remain. Future work should prioritize improving the target detection and orbit association processes, which are crucial for the primary satellite to reliably identify the secondary within an image. This task becomes particularly challenging if the secondary maneuvers, as the target may appear far from its expected position, complicating reliable detection. Additionally, an estimate of the magnitude of attitude maneuvers required to point at targets should be made to ensure that their costs are offset by the benefits of reducing CAMs.

Appendix A

EOIR processing

EOIR is an STK plug-in tool that provides different key capabilities for the end-to-end simulation of electro-optical and infrared sensor operations. These include advanced sensor modeling capabilities, modeling of optical and thermal target properties, and generation of synthetic imagery. These functionalities are integrated within STK's dynamic simulation scenarios, ensuring that sensor operations are simulated by incorporating aspects such as orbital dynamics and atmospheric conditions.

To simulate what the onboard sensor sees at each instant and provide resulting image outputs, EOIR uses two main components, which are the scene generator and the sensor model. The scene generator computes the amount and direction of radiant energy arriving at the sensor aperture, where several factors are accounted for such as objects position, illuminating sources, and surface material properties [A.1]. The sensor model then processes this information by simulating the sensor's optic and radiometric response, ultimately generating digitized images.

A.1 Objects model

To enable the calculations behind scene generation, every object in the scenario must first be properly modeled, accounting for aspects such as its dimensions and thermal properties. Central bodies in the solar system, such as the Sun or the planets, are represented as spheres with defined radii. Thermal models and, occasionally atmospheric models are available based on validated models that incorporate empirical research findings. For example, the Earth's thermal model is based on [A.2] while its atmosphere is simulated using MODTRAN®. Stars are pure point sources with blackbody spectral irradiance given by the star's effective temperature and visual magnitude. Stars data, including celestial coordinates, is derived from either the Hipparcos or Tyco catalogs, depending on the user's selection. In this work, Hipparcos is chosen, and including all stars with a lower apparent magnitude than 15.

Other objects within the scenario, such as satellites and debris, are incorporated into the scene generation by designating them as "target" and defining their shape, size, surface material, and temperature. Since primary objects serve as observers and do not influence scene generation, they are not designated as targets. As for secondary objects, given their real-world diversity in shapes and sizes that range from tiny irregular debris fragmens to large defunct spacecraft, in this work they are modeled

as spheres with uniform surface material and varying dimensions, as detailed in Section 4.1.2. Concerning the material's optical properties, EOIR provides 27 selectable options, including "Aluminum MLI (multi-layer insulation)" and "White Thermal Control Paint". EOIR maintains a unique spectral reflectance profile for each material option, detailing the wavelength-dependent reflectance characteristics of each material, derived based on data from NASA Reference Publication 1121 [A.3]. The "Gray body" option allows a user-selectable reflectance value that is assumed constant across the spectrum, ranging from 0% (black body) to 100% (white body). Given the wide range of materials characterizing the population in LEO, the gray body option is chosen to model secondary objects, employing statistically representative reflectance values, as specified in Section 4.2.2. In terms of thermal material properties, determining how much thermal energy an object emits, EOIR assigns a fixed temperature for the entire body. For objects in LEO, surface temperatures typically span -150°C to +150°C. Within this range, visible light emission is negligible compared to reflected light contributions. Therefore, a standard value of 50°C is selected for all secondaries, with a negligible influence on the simulation outcomes.

A.2 Scene generation

As a first step, the scene generator performs geometric calculations to determine the relative position of all objects falling within the sensor's FoV, including stars. The sensor's frustum is sampled at a finer angular resolution than each pixel's instantaneous FoV, creating a granular representation of the scene. For each angular sample, the radiant energy arriving from the detected objects is computed as the sum of three contributions. The first one is representative of the diffuse night sky brightness and includes airglow, zodiacal light, and integrated starlight. The second contribution is self-radiance, calculated through the Planck function based on the objects' surface temperature and emissivity. The last contribution is the reflected radiance, which is the light originating from sources such as the Sun or Earth and bouncing off the detected objects. To model the reflection process, a bi-directional reflectance distribution function based on a modified Phong Reflection model is utilized [A.1]. In all these calculations, radiometric coupling between surfaces is accounted for, defined as the throughput of radiant energy exchanged between two surface areas. The scene generator's output to the sensor model is a two-dimensional array of spectral radiance vectors, each associated with an angular sample within the FoV.

A.3 Sensor model

At a high level, the EOIR model of electro-optical sensors consists of a single equivalent thick lens followed by a focal plane array made of a grid of pixels. Then, several user-defined parameters characterize the specific sensor response, namely its ability to convert incident radiance into an electrical signal. These parameters are organized into four categories: spatial, spectral, optical, and radiometric.

Spatial parameters include the FoV, number of pixels, and detector pitch. Together with the focal length, they are utilized by the scene generator to map angular samples with respect to the focal plane array. The spectral response of the sensor is

characterized by an idealized bandpass defined between two user-defined wavelengths, which represent the lower and upper bounds of the sensor's sensitivity, with a response of one within this range and zero outside of it. The scene spectral radiances arriving at sensor aperture are integrated over this wavelength range. Optical parameters encompass the entrance pupil diameter Φ, the effective focal length f, and the transmission coefficient T. The optical response of the system further accounts for degradation effects due to diffractions, aberrations, blurring caused by the longitudinal defocus of the optical system, and line-of-sight jitters, which are undesired fluctuations in the sensor's pointing direction caused by high-frequency vibrations arising onboard the satellite. All these effects, requiring specific user inputs like the root-mean-square wavefront error for aberrations, are modeled through different Optical Transfer Functions (OTFs), which collectively define the overall system OTF. The system's Point Spread Function (PSF), describing how the imaging system responds to a point source, is then obtained as the two-dimensional Fourier transform of the system OTF. The PSF is also used to determine the fractional ensquared energy, which is the portion of total energy from a point source that is captured by a single pixel centered on that source. Concerning radiometric parameters, they include quantum efficiency QE, fill factor FF, variance of the read noise σ_{rn}, variance of the dark current rate σ_{dc}, and integration time τ. Standard radiometric equations incorporating these parameters and the system OTF are utilized to convert radiances into an electronic signal expressed in electrons.

In addition to the signal electrons, other electrons are added to each pixel to account for explicit noise sources such as dark current, read noise, and Poisson-distributed shot noise. Other modeled contributions that could be considered noise, but are implicitly accounted for within the computed scene radiances, are path radiance (namely scattered sunlight or moonlight and thermally generated path radiance), background noise sources, and optical distorsion. The total number of electrons in each pixel is limited by the detector's Full Well Capacity (FWC), provided as input, thereby emulating pixel saturation. As a last step, EOIR simulates the analog-to-digital conversion by performing a quantization step, in which the signal is discretized by assigning one digital count for every specified number of electrons, which depends on a user-defined sensor's bit depth. During this step, quantization noise is inherently introduced in the measurements.

References

[A.1] R. Anderson, G. Cantwell, "STK EOIR model description and validation," Space Dynamics Laboratory, North Logan, UT, USA, Tech. Rep. SDL/10-393, 2010.

[A.2] A. Ignatov, G. Gutman, "Monthly mean diurnal cycles in surface temperature over land for global climate studies," *Journal of Climate*, vol. 12, no. 7, 1999, pp. 1900-1910, doi: https://doi.org/10.1175/1520-0442(1999)012<1900:MMDCIS>2.0.CO;2

[A.3] J. H. Henninger, "Solar absorptance and thermal emittance of some common spacecraft thermal-control coatings," NASA, Washington, DC, USA, Tech. Rep. NASA-RP-1121, 1984

Appendix B

Mapping pixel-to-sky coordinates using FITS and WCS standards

The Flexible Image Transport System (FITS) and World Coordinate System (WCS) are fundamental standards in astronomy, working together to store and interpret data from telescopes and other imaging instruments. FITS is a file format designed for storing astronomical data, including not only images but also tables and multidimensional arrays. Each FITS file has a data section where the actual image or observational data is stored, and a descriptive header section. This header contains standard keyword-value couples including data such as the date of observation, the telescope used, and WCS transformation parameters.

WCS conventions provide a formalized method of encoding how positions in an image (pixel coordinates) map to real-world celestial coordinates – typically RA/DEC – in the header of a FITS file. In other words, FITS provides the format and structure, while WCS provides the mathematical conventions for representing spatial information, so they are highly complementary.

The following provides the fundamentals for utilizing key FITS data to develop a direct function for transforming pixel coordinates to RA/DEC. The full FITS format, which is standardized by the International Astronomical Union (IAU), is available in a single reference [B.1]. WCS conventions are defined across three formal papers ([B.2], [B.3], [B.4]); however, most of their content is also included in the official FITS standard document.

Among the 53 keywords defined in the FITS standard, the main ones necessary for establishing the transformation typically include:

- `CRPIXn`: reference pixel coordinates (in pixels), where `n` can be 1 or 2, representing x or y axis coordinates, respectively,
- `CRVALn`: celestial coordinates of the reference pixel (RA/DEC),
- `CTYPE`: specifies the coordinate system and projection type (e.g., gnomonic projection),
- `CDn_m` (where `n` and `m` can be 1 or 2) linear transformation matrix elements for rotation, scaling, and shear,

- `A_ORDER` and `B_ORDER`: define the order of the polynomial terms used for distortion corrections,
- `A_n_m` and `B_n_m` (with `n` and `m` varying up to the values defined by `A_ORDER` and `B_ORDER`): coefficients for the Simple Imaging Polynomial (SIP) distortions, enabling a nonlinear transformation to handle optical distortions.

The following steps outline the procedure to transform a generic pixel (p_x, p_y) into RA/DEC values using the above WCS parameters. This procedure assumes that the `CTYPE` keyword specifies a TAN (gnomonic) projection, as is consistently the case for the plate-solved images used in this thesis.

The transformation begins by using the reference pixel coordinates and their associated RA and DEC values to define the origin. Each pixel coordinate (p_x, p_y) is first offset relative to the reference pixel:

$$p_x{}' = p_x - CRPIX1$$
$$p_y{}' = p_y - CRPIX2$$

If Simple Imaging Polynomial (SIP) distortions are included, they are applied to the pixel coordinates using polynomial terms. These terms correct the pixel coordinates for distortions, resulting in the updated coordinates ($p_x{}''$, $p_y{}''$):

$$x_{corr} = \sum_{i,j=0}^{(i+j)\leq A_{ORDER}} A_{ij}(p'_x)^i(p'_y)^j$$
$$y_{corr} = \sum_{i,j=0}^{(i+j)\leq B_{ORDER}} B_{ij}(p'_x)^i(p'_y)^j$$
$$p_x{}'' = p_x{}' + x_{corr}$$
$$p_y{}'' = p_y{}' + y_{corr}$$

After the distortion correction, the linear transformation matrix CD is applied to account for rotation, scaling, and shear. This transformation produces the intermediate coordinates ξ and η in the projection plane:

$$\begin{bmatrix}\xi\\ \eta\end{bmatrix} = \begin{bmatrix}CD_{11} & CD_{12}\\ CD_{21} & CD_{22}\end{bmatrix} \cdot \begin{bmatrix}p_x{}''\\ p_y{}''\end{bmatrix}$$

In the final step, the intermediate plane coordinates (ξ, η) are converted to celestial coordinates (RA, DEC) using the TAN (gnomonic) projection:

$$RA = CRVAL1 + \tan^{-1}\left(\frac{\xi}{\cos(CRVAL2) - \eta\sin(CRVAL2)}\right)$$
$$DEC = \tan^{-1}\left(\frac{\eta\cos(CRVAL2) + \sin(CRVAL2)\cdot\sin(RA - CRVAL1)}{\xi}\right)$$

References

[B.1] FITS Working Group, "Definition of the Flexible Image Transport System (FITS)," International Astronomical Union (IAU), Tech. Rep., v. 4.0. Accessed Nov 2, 2024. [Online]. Available: https://fits.gsfc.nasa.gov/standard40/fits_standard40aa-le.pdf

[B.2] E. W. Greisen, M. R. Calabretta, "Representations of World Coordinates in FITS (Paper I)," *Astronomy & Astrophysics*, vol. 395, no. 3, 2002, pp. 1061-1075, doi: https://doi.org/10.1051/0004-6361:20021326

[B.3] M. R. Calabretta, E. W. Greisen, "Representations of Celestial Coordinates in FITS (Paper II)," *Astronomy & Astrophysics*, vol. 395, no. 3, 2002, pp. 1077-1122, doi: https://doi.org/10.1051/0004-6361:20021327

[B.4] E. W. Greisen, M. R. Calabretta, F. G. Valdes, S. L. Allen, "Representations of Spectral Coordinates in FITS (Paper III)," *Astronomy & Astrophysics*, vol. 446, no. 2, 2006, pp. 747-771, doi: https://doi.org/10.1051/0004-6361:20053818

Appendix C

Un-correct for annual aberrations

Consider first the procedure to correct for annual aberrations, which transforms apparent RA/DEC (α, δ) into corrected RA/DEC (α', δ').

The first step involve converting spherical to Cartesian coordinates:

$$\boldsymbol{r}' = \begin{pmatrix} x \\ y \\ z \end{pmatrix} = \begin{pmatrix} \cos(\delta)\cos(\alpha) \\ \cos(\delta)\sin(\alpha) \\ \sin(\delta) \end{pmatrix}$$

Next, calculate the observer's velocity:

$$\boldsymbol{v}' = \begin{pmatrix} v_x \\ v_y \\ v_z \end{pmatrix} = \frac{\boldsymbol{v}'_E + \boldsymbol{v}'_{obs}}{c}$$

Where c is the speed of light, while $\boldsymbol{v}'_E$ and $\boldsymbol{v}'_{obs}$ are the velocity of Earth and the observer, respectively, relative to a J2000 frame centered at the barycenter of the Solar System.

Compute Lorentz scaling parameters χ and β:

$$\beta = \sqrt{1 - \|r' \cdot v'\|^2}\ \chi = \frac{r' \cdot v'}{1 + \beta}$$

Transform $\boldsymbol{r}'$ into corrected position $\boldsymbol{r}'_{\boldsymbol{corr}}$:

$$\boldsymbol{r}'_{\boldsymbol{corr}} = \begin{pmatrix} x' \\ y' \\ z' \end{pmatrix} = \begin{pmatrix} \beta x + v_x + \chi v_x \\ \beta y + v_y + \chi v_y \\ \beta z + v_z + \chi v_z \end{pmatrix}$$

Finally, compute the corrected RA/DEC:

$$\alpha' = \arctan\left(\frac{y'}{x'}\right)\ \delta' = \arctan\left(\frac{z'}{\sqrt{x'^2 + y'^2}}\right)$$

Identifying with $\boldsymbol{f}(\alpha, \delta, v'_{\mathrm{E}}, v'_{\mathrm{obs}})$: $\mathbb{R}^2 \to \mathbb{R}^2$ the overall function returning α', δ' for an input pair of (α, δ), the inverse transformation is simply obtained by solving the following minimization problem:

$$\begin{bmatrix} \alpha \\ \delta \end{bmatrix} = \min_{\alpha,\delta} \left\| \boldsymbol{f}(\alpha, \delta, v'_{\mathrm{E}}, v'_{\mathrm{obs}}) - \begin{bmatrix} \alpha' \\ \delta' \end{bmatrix} \right\|^2$$